January 2013

Spin Dependent Transport in Novel Magnetic Heterostructures

Priyanga Buddhika Jayathilaka
University of South Florida, jayathilaka_kgpb@yahoo.com

Spin Dependent Transport in Novel Magnetic Heterostructures

by

Priyanga Buddhika Jayathilaka

A dissertation submitted in partial fulfillment
of the requirements for the degree of
Doctor of Philosophy
Department of Physics
College of Art and Sciences
University of South Florida

Major Professor: Casey W. Miller, Ph.D.
Sarath Witanachchi, Ph.D.
Hariharan Srikanth, Ph.D.
Denis Karaiskaj, Ph.D.
Sanjukta Bhanja, Ph.D.

Date of Approval:
April 26, 2013

keywords:
Spintronics, Magnetite, Magneto Resistance, Spin valve, Spin caloritronics, Spin Seebeck effect, Magnetothermopower

Dedication

To my Parents, for showing me that any hurdle can be overcome by courage and hard work, for believing in me all the time and for unconditional love and support provided to me.

To my Wife, for being with me all the time and encouraging me continuously to follow my dreams.

To my baby girl Sanuthi, for reminding me that the life is lot more than physics.

Acknowledgments

First, I would especially like to convey my thanks to Dr. Casey W. Miller for his exceptional support and guidance provided to me during the last five years. He was not only my mentor, but also my role model in and out of the lab. I would like to show my appreciation for his mentoring approach, which made research look so simple and fun. I would also like to give thanks for his patience with my annoying Sri Lankan accent. I always enjoyed working in the lab with him, and every time I learned something new. Out of everything, the best things I learned from him were probably bowling and darts.

Secondly, I would like to thank Dr. Dale Johnson for providing me the information and guidance during the first half of my graduate school career. He was calm, quiet and always had answers for our problems. Also the administrative support given by Daisy Matos, Candice Pietry and Mary Ann Prowant was greatly appreciated.

I would also like to thank Dr. Brian Kirby for allowing me to go to NIST to complete my industrial practicum. It was a great experience and a privilege to work with him in a world class research facility.

Also, I would like to give special thanks to Dr. Sarath Witanachchi for helping me to come to the USF and for introducing me to the community.

I must also thank my fellow lab mates and other physics graduate students for their support; without them, most of this work would not have been done. First, I would like to thank Dustin Belyea for being with me the entire time and supporting me in every single experiment. His machine shop and computer programming skills especially have made my life much easier. I would like to also thank my first full time

lab mates, Daryl Williams and Christopher Bauer for their support in developing the lab and doing X-ray and EDX measurements for my experiments. Next, I would like to thank Hillary Kirby for reducing my work load by taking over the responsibilities of the sputtering system and other maintenance in the lab. I would also like to thank Scott Campbell and Tatiana Eggers for helping me out in my experiments in various ways; they truly turned the lab into a fun place to work. I would also like to thank all of the undergraduate students who have worked with me in last five years: Diana Nesbitt, Sarayah Caray, Matthew Carver, Jonathan Willman and Courtney Halpin, as well as high school students Simeng Zhu and Kristina Hendrix. They not only contributed to my experiments in various ways, but also gave me my own mentoring experience, and I greatly appreciate that. I must also thank Dr. Robert Hyde for training me on XRD and SEM tools.

Last, but not least, I would like to thank all my family and friends for their love and support. Without them I would have gone mad during last five years.

Contents

List of Figures

List of Tables

Abstract

Magnetic oxides have become of interest source for spin transport devices due to their high spin polarization. But the real applications of these oxides remains unsatisfactory up to date, mostly due to the change of properties as a result of nano structuring. Magnetite (Fe_3O_4) is one such a material. High Curie temperature and the half metallicity of Fe_3O_4 make it a good potential candidate for spin transport devices. Studies have shown that the nano structuring Fe_3O_4 changes most of it's important properties. This includes high saturation magnetization and drop of conductivity by a few orders of magnitude in Fe_3O_4 thin films.

In this study, we have successfully grown Fe_3O_4 by reactive sputtering and studied the effect of transition metal buffer layers on structural, transport, and magnetic properties of Fe_3O_4. It is shown that the lattice strain created by different buffer layers has major impacts on the properties of Fe_3O_4 thin films. Also for the first time, the magnetic force microscopic measurements were carried out in Fe_3O_4 thin films through Verway transition. MFM data with the magnetization data have confirmed that the magnetization of Fe_3O_4 thin films rotate slightly out of the plane below the Verway transition.

Fe_3O_4 thin films were also successfully used in fabricating spin valve structures with Chromium and Permalloy. Here, the Fe_3O_4 was used to generated the spin polarized electrons through reflection instead of direct spin injection. This is a novel method that can be used to inject spins into materials with different conductivities, where the traditional direct spin injection fails. Also the effect of growth field on Fe_3O_4 and Fe_3O_4/Cr/Py spin valves were investigated. In Fe_3O_4 the growth field

induced an uni-axial anisotropy while it creates a well define parallel and anti-parallel states in spin valves.

Magneto thermal phenomenon including spin dependent Seebeck effect, Planar Nernst effect and Anomalous Nernst effect were measured in ferromagnetic thin films and spin valves. Spin dependent Seebeck effect and planar Nernst effect were directly compared with the charge counterpart anisotropic magneto resistance. All the effects exhibited similar behavior indicating the same origin, namely spin dependent scattering.

1 Introduction

1.1 Spintronics

Spintronics stands for Spin transport electronics, where the electron spin is used to fabricate a new generation of transport devices [1], [2], [3]. Even though the idea of spintronics was used since 1970's the real applications started only after the invention of the Giant Magneto Resistance (GMR) by Albert Fert and Peter Grunberg in 1988 [4], [5]. This invention revolutionized the magnetic recording industry by producing hard drives with high capacity and won the Nobel price in 2007.

Similar to the electron charge in conventional electronics, in spintronics the information is carried by the electron spin, which can be detected by it's magnetic moment, $-g\mu_B s$.Where"**s**" is the electron spin, "μ_B" is the Bohr magneton and the "**g**" is the gyro-magnetic coefficient. In spintronics, the orientation of magnetic spin (phase of the spin) with respect to an applied magnetic field or to a magnetic orientation of a ferromagnetic film is used to store the information. In device fabrication, orientation of the spin is used to manipulate other properties such as electrical current and voltage in a predictable way. The most impactful applications of the spintronics are in the magnetic recording industry [6]. Magnetic read heads in modern hard drives and Magnetic Random Access Memories (MRAM) are among the main applications. Main advantages of spintronics technology over conventional electronics are the non-volatility, high data storage density, high read/write speeds and low electric consumption.The most important aspects of spintronics are the generation of spin polarized current, optimizing the spin life time, transporting spin polarized current

through materials without loosing the polarization, and the detection of the spins. Most of the present day research on spintronics focuses on the above topics.

1.2 Generating spin polarized current

Spin polarization is defined as P=$\frac{N(\uparrow) - N(\downarrow)}{N(\uparrow) + N(\downarrow)}$, where $N(\uparrow)$ are the number of electrons with spin up orientations and the $N(\downarrow)$ are the number of electron with spin down orientation. Any non magnetic material has equal number of spin up and spin down electrons giving zero spin polarization to the material. Injecting spin polarized current into these non magnetic materials is a fundamental requirement in fabricating spin transport devices. Spin polarized current can be generated by optical [7] and electrical [8] techniques. But for device fabrication, electrical spin polarization techniques are more desirable. In electrical spin injection, a magnetic electrode directly connects to a non magnetic material and applies a current into the structure. This current drives the spin polarized current into the non magnetic material creating a spin accumulation in the non magnetic material. The spin accumulation and the spin penetration depth [9] depend on various factors such as spin relaxation, where polarized spins bounce back to their equilibrium un-polarized state, spin-orbital coupling and the purity (relative residual resistance) of the material.

1.2.1 Direct spin injection from ferromagnetic to a non magnetic metal

Direct spin injection from a ferromagnetic material to a non magnetic (normal) metal is the most commonly used method to produce spin polarized current. In a normal metal, the density of states of spin up and spin down electrons are equal. When a voltage is applied to normal metals both spin up and spin down electrons carry equal amount of current, giving equal conductivities to both spin channels. This gives zero spin polarization to the normal metal. To get a spin polarized current into the normal metal we should be able to contact one spin channel and apply a different voltage to

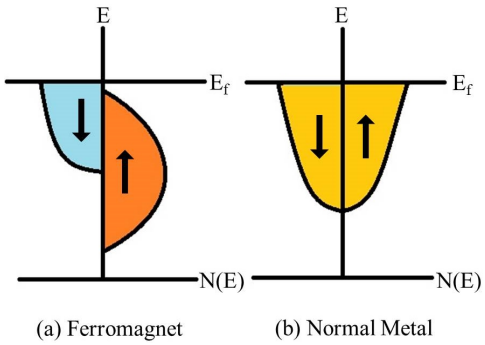

Figure 1.1: Density of States of a Ferromagnetic material and Non magnetic material

it. This is impossible to do just using a normal metal. The simplest way to do this is to apply the current though a ferromagnetic contact, which acts as a spin dependent resistor. Ferromagnets have different density of states for spin up and spin down electrons at Fermi level (fig.1.1) . This provides different conductivities for two spin channels. The Ohm's law can be applied for each spin channel.

spin up electrons $$\vec{\nabla}\ \mu^{\uparrow} = -\frac{e\ j^{\uparrow}}{\sigma^{\uparrow}}$$

spin down electrons $$\vec{\nabla}\ \mu^{\downarrow} = -\frac{e\ j^{\downarrow}}{\sigma^{\downarrow}}$$

Where σ is the conductivity for each spin direction and ej is the current density for respective spin species. The continuity of un-polarized current leads the Ohm's law and the Poisson's equation to

$$\vec{\nabla}\ \vec{j} = 0.$$

For the spin polarized currents, the spin up and spin down components should be taken into account separately. Since the spin up current can be transferred into spin down current through spin flip

$$\vec{\nabla}\ \vec{j}^{\uparrow\downarrow} = -\vec{\nabla}\ \vec{j}^{\downarrow\uparrow}$$

The spin transport across the Ferromagnetic/Non-magnetic (FM/NM) interface can be treated with the diffusion equation,

$$\frac{\mu^{\uparrow} - \mu^{\downarrow}}{\tau_{sf}} = D\nabla^2(\mu^{\uparrow} - \mu^{\downarrow})$$

where $D = \frac{v_f l}{3}$ is the diffusion constant, v_f is the Fermi velocity, l is the electron mean free path and the τ_{sf} is the spin flip time.

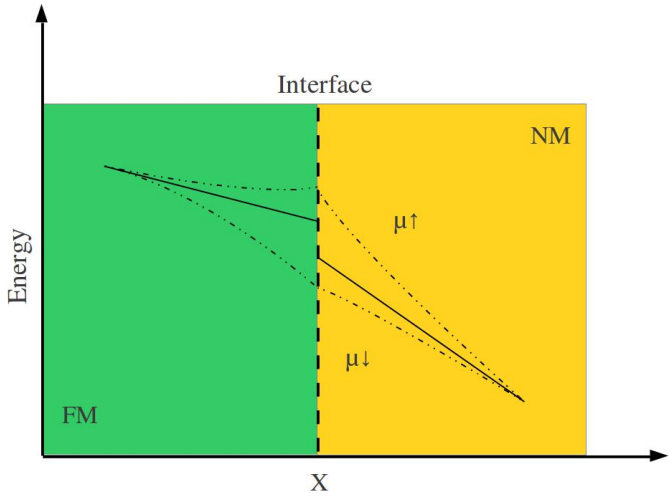

Figure 1.2: Ferromagnetic-Nonmagnetic interface

By solving the differential equation with boundary conditions at x = $\pm(\infty)$

$$\mu \uparrow = \mu \downarrow = \mu_0$$

and let $\mu^{\uparrow} - \mu^{\downarrow} = \mu_s$,

Then the diffusion equation leads to,

$$\mu_s(x) = \mu_s(x = 0).e^{-x/\lambda}$$

According to the above equation, if the μ_s is non zero at the interface (x=0), there should be a non zero spin polarization at the normal metal [10]. Also the μ_s decays exponentially within the spin flip diffusion length, $\lambda = (D\tau_{sf})^2$. Here both $\mu_{\uparrow}$ and $\mu_{\downarrow}$ are continuous through the interface but μ_0 is not. This difference between the chemical potentials drives spin polarized current into the NM with different spin up and spin down current densities. But the total current density j remains constant.

This method has been successfully used in most of the metallic systems. But it is proven to fail when the conductivities of two materials are mismatched. Theoretical models have shown that for this method to be successful, either both normal metal and the ferromagnetic material should have closely matched conductivities or the ferromagnetic material should be 100% spin polarized [11]. However, experiments which have attempted to inject spins from ferromagnet metal to semiconductors have shown less than 1% spin polarization effect [12] [13] in the semiconductor, which is not sufficient for real world applications. Therefore direct spin injection has become unsatisfactory method when it come to materials with different conductivities.

1.2.2 Polarization by reflection

In this method a non zero spin polarization is induced in the normal metal by reflection of conduction electrons off the interface of a ferromagnetic material. Injecting spins into normal metals through reflection is already been proven [14] [15] [16]. The efficiency of the reflected base process is also similar to the efficiency of the direct injection process. Therefore, generating spin polarized current through reflection can be used in device fabrication. From this view, consider fig.1.3 in which, magnetic

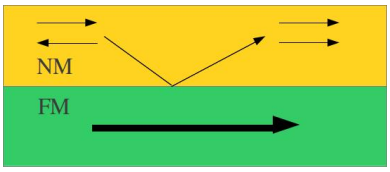

Figure 1.3: Unpolarized electrons get reflected off the FM and gains the spin polarization.

insulators are used with normal metals. When a current is applied to the structure, higher resistivity of the magnetic insulator prevents current flowing into it, keeping the most of the current in normal metal. This can be demonstrated by parallel resistor model. Two layer structure shown in fig.1.3 can be represented by two resistors parallel to each other (fig.1.4).

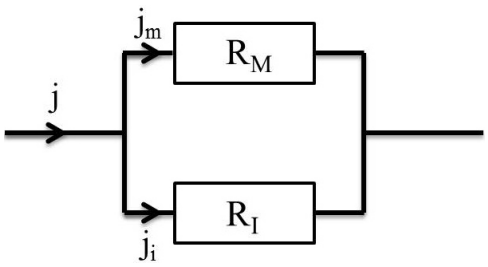

Figure 1.4: Parallel resistor model

$$\text{The current density through insulator,} \quad j_i = \frac{R_M}{R_M + R_I}\, j$$

$$\text{The current density through metal,} \quad j_m = \frac{R_I}{R_M + R_I}\, j$$

$$\text{If } R_M << R_I,$$

$$\text{Then, } R_M + R_I \approx R_I$$

This leads the current density through the metal (j_m) to be equal to the total current density ($j_m \approx J$). This implies that, if the resistance of the magnetic insulator is considerably high relative to the resistance of the metal, the current will mainly flow through the metal.

When the current is applied to the structure, electrons closer to the magnetic layer get reflected off the interface and get spin polarized. Similar to the direct spin injection, the spin polarization decays exponentially with the film thickness. Even though this method has proven to be a success, it hasn't been used that much in fabricating real spintronics devices. In this dissertation I am presenting the use of reflection based method in fabricating spintronics devices.

1.3 Giant Magneto Resistance (GMR)

Giant magneto resistance was first invented in 1988 by Albert Fert and Peter Grunberg in (100) oriented single crystal Fe/Cr/Fe sandwich structure and Fe/Cr super

lattice [5], [4] grown using Molecular Beam Epitaxy (MBE). Since the resulted magneto resistance values were much larger ($\frac{\Delta R}{R} \approx 25\%$) than to the anisotropic magneto resistance (AMR) of a single layer of Fe, the effect was named as "Giant magneto resistance". Later GMR was also measured on polycrystalline Fe/Cr sandwiches and superlattices deposited through magnetron sputtering [17].

To understand the GMR effect consider a simple spin valve structure with two ferromagnetic layers and a normal metal layer in between.

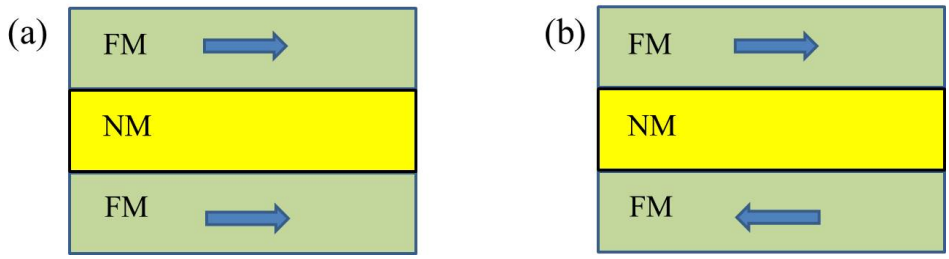

Figure 1.5: Spin valve structure with parallel(a) and anti-parallel (b) configurations

Depending on the thickness of the normal metal layer, two magnetic layers couple either ferromagnetically or anti-ferromagnetically at zero applied field. This coupling can be explained through RKKY (Ruderman,Kittle, Kasuya, Yosida) interactions [18] [19] [20].

The interaction between nuclei spins i and j at a distance R_i and R_j through electron scattering is given by

$$H(R_{ij}) = \frac{I_i.I_j}{4} \frac{|\Delta k_m \; k_m|^2 m^*}{(2\pi)^3 \; {R_{ij}}^4 \; \hbar^2} [2k_m R_{ij} \cos(2k_m R_{ij}) - \sin(2k_m R_{ij})]$$

This model explains the coupling between magnetic moments of two metallic nuclei via conduction electrons. In the spin valve structure, the nuclei of two ferromagnetic layers mutually couple with each other indirectly through conduction electrons. The variation of $H(R_{ij})$ with respect to R_{ij} is oscillatory. Therefore depending on the distance between two nuclei (in spin valves, this is just the normal metal thickness)

two nuclei can couple either ferromagnetically or anti-ferromagnetically at zero field.

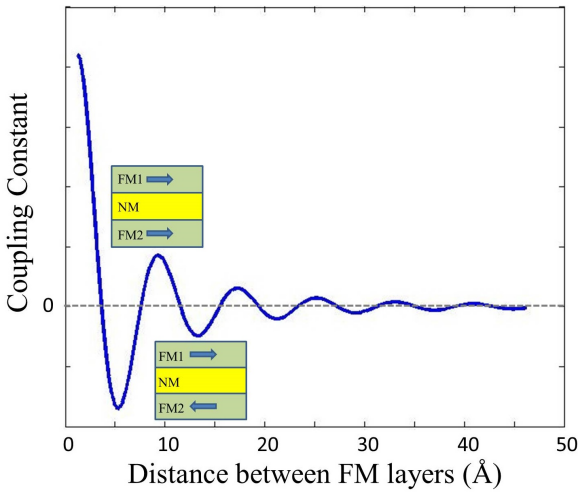

Figure 1.6: RKKY coupling

The resistance of the spin valve changes with the coupling state. Therefore ferromagnetically and anti-ferromagnetically coupled states have different resistances at zero field. Usually the anti-ferromagnetically coupled state has higher resistance than the ferromagnetically coupled state. A higher magnetic field can be used to overcome the anti-ferromagnetic coupling and align all the spins parallel to each other. The resistance of the spin valve becomes lower, similar to the ferromagnetic coupling. If the external magnetic field sweeps to a lower value the anti-ferromagnetic coupling become stronger and two ferromagnetic layers return back to anti-ferromagnetically coupled state.

To understand the spin valve mechanism consider two ferromagnetic layers with different coercivities separated by a non magnetic layer (Fig. 1.7). Here the top two graphs show the magnetic hysteresis loops of the two ferromagnetic layers FM1 and FM2 respectively and the third graph shows the Giant Magnetoresistance effect of the spin valve. By applying a higher external magnetic field both ferromagnetic layers can be aligned along the direction of the magnetic field making them parallel to each other. This gives lower resistance to the spin valve structure (region 6). Then the external field sweeps from positive to negative fields. At position (3) the

magnetization of FM1 layer flips by 180 deg to align with the external field making it anti-parallel to FM2. This gives higher resistance to the structure in the area between (2)and (3). At the position (2) the FM2 also flips magnetization by 180 deg making it parallel with FM1. This gives lower resistance to the structure in area (1). Similar behavior can be seen when the external field sweeps from negative to positive fields. At position (4) FM1 flips magnetization making it antiparallel to FM2. This gives higher resistance to the areas between (4) and (5). At position (5) FM2 also flips its magnetization giving a lower resistance to the area (6).

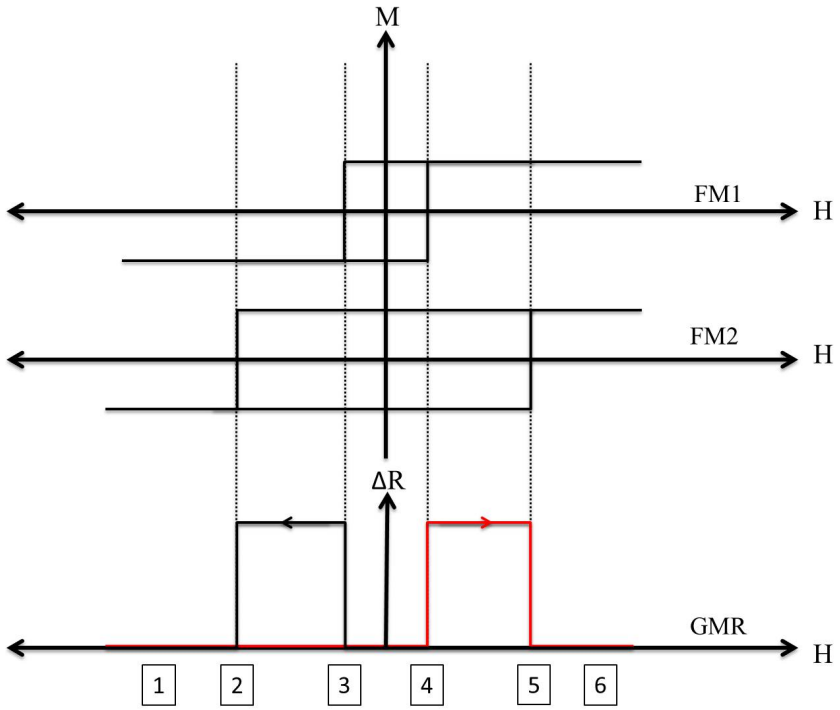

Figure 1.7: GMR mechanism

The origin of GMR in spin valve is mainly due to the spin dependent scattering, with the interface scattering being more significant than bulk scattering [21]. As shown in the fig.1.8, the first FM layer polarizes the incoming electrons and injects it into the normal metal. Then the spin polarized current passes through the NM and reaches the interface of the NM and the second FM layer. If the spin of the incoming

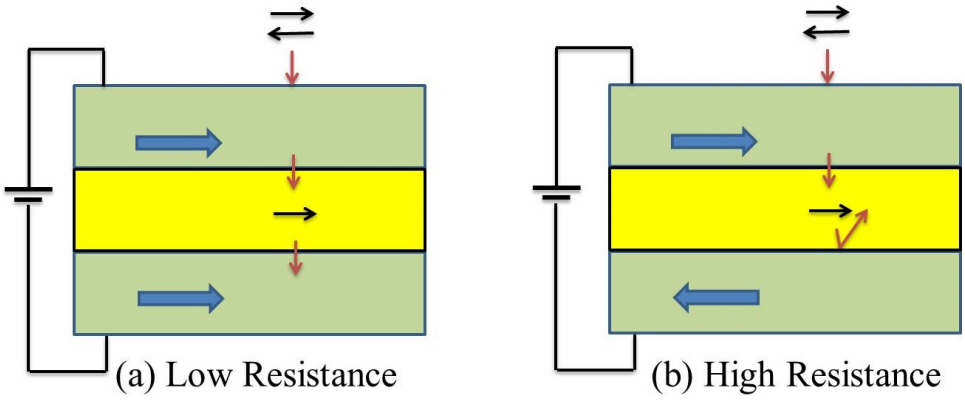

Figure 1.8: Spin dependent scattering

current is aligned with the spin of the second FM layer, then the current passes through the second FM layer without significant additional resistance. If the spin of incoming electrons are not aligned with the second FM layer, then those electrons are strongly scattered at the NM-FM interface, giving additional resistance to the spin valve structure. Fig. 1.8 (a) and (b) show the scattering from the interfaces depending on the polarities of the FM layers along with the schematics of the density of state graphs for each layer.

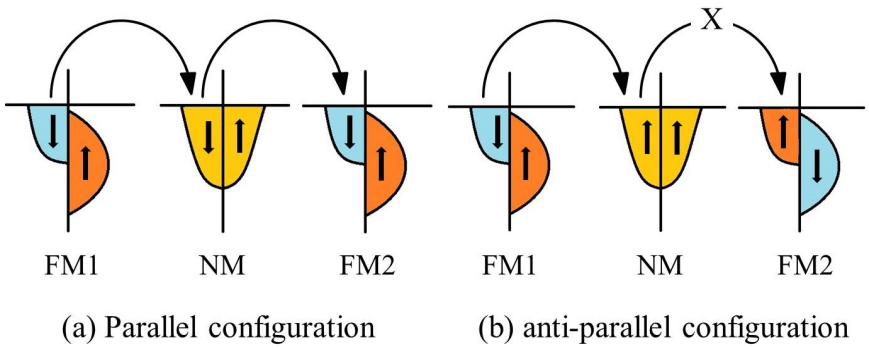

Figure 1.9: GMR behavior using density of states of FM and NM layers

This can be also explained using the density of states of materials. In ferromagnetic materials, due to exchange splitting spin up and spin down bands shift. In a strong ferromagnetic material, Fermi level only has one type of spins. Here we assume that in FM1, the Fermi level only has a band with spin down electrons (fig.1.9). In

both parallel and anti-parallel situations spin down electrons can move from FM1 to the NM without additional resistance. Because in NM, Fermi level has both spin up and spin down bands open. In parallel configuration, since FM2 has spin down band open at the Fermi level, spin down electrons can move without additional resistance. But in anti-parallel configuration, the FM2 does not have a spin down band at the Fermi level. Due to the Pauli exclusion principle spin down electrons cannot go in to the spin up band. This introduces an additional resistance in anti-parallel configuration relative to the parallel configuration.

1.4 Different Geometries

Mainly two different geometries have been used in measuring GMR: Current in Plane (CIP) geometry and Current Perpendicular to the Plane geometry (CPP). The CPP geometry is more popular due to higher GMR values and ability to retain the GMR effect even in thicker layers.

Current Perpendicular to the plane geometry (CPP)

In this geometry current flows perpendicular to the sample plane, as described in Fig. 1.8. When the two FM layers are parallel to each other, incoming electrons weakly scatter at the interfaces and gives low resistance. When the FM layers are anti-parallel to each other,the interface scattering dominates and gives higher resistance to the spin valve. CPP geometry gives higher GMR compared to CIP geometry.But CPP geometry requires complicated fabrication techniques to overcome the lower resistance across the junction. Since the layer thicknesses are in the order of few nano meters the resistance across those layers are significantly lower. Several techniques are used to overcome this problem, such as reducing the area of the layers by making them as nano pillars. The most interesting property of CPP is the GMR can be observed in spin valves with layer thickness as big as microns. Here the spin polarized current

flow perpendicular to the plane give rise to spin accumulation effect and generates long spin diffusion lengths [22].

Current in plane geometry (CIP)

In contrast to the previous geometry, in CIP current flow along the length of the spin valve.

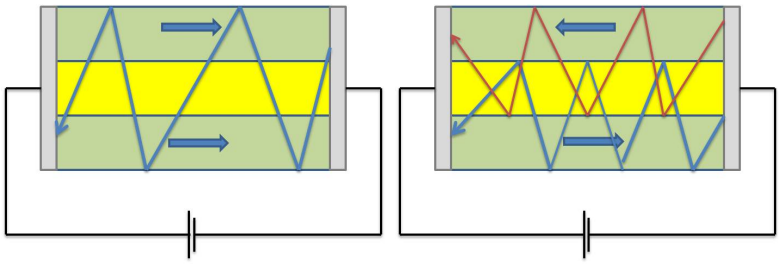

(a) Low Resistance (b) High Resistance

Figure 1.10: Current In plane Geometry

Therefore the lower resistance across the junction is not a problem in this geometry. The actual mechanism, which governs the GM in this method is much more complicated than CPP. As a result of this complication one cannot simply predict CPP GMR valves from CIP GMR measurements. For the understanding we can explained it as shown in fig. 1.10. When the two magnetic layers are parallel to each other electrons undergo less scattering at the interfaces and lead to longer path lengths.This gives lower resistance to the structure. In anti-parallel case the conduction electrons scatters significantly at the interface leading to a higher resistance. In this geometry, the GMR values decrease significantly with the increasing layer thicknesses. However it is possible to see smaller GMR values at higher layer thicknesses due to bulk scattering.

1.5 Magnetite

Magnetite is a material that has been studied extensively in the past due to its unique properties such as Verwey transition, half metallicity and high Curie temperature (853°C). It is also reported to be the oldest known magnet, and was discovered in China. The half metallicity, which results in 100% spin polarization at the Fermi level, make magnetite a promising materials for spintronics applications [23]. Magnetite is a ferrimagnetic material with a spinel structure and has the chemical formula of $Fe_A^{3+}[Fe^{3+}\ Fe^{2+}]_B\ O_4$. Here, big O^{2-} ions form a close packed face-centered cubic lattice with both the Fe^{2+} and Fe^{3+} ions sharing the interstitial sites. There are two types of interstitial sites that can be recognized on Fe_3O_4 structure. The tetrahedral sites (red) are occupied by the Fe^{3+} atoms and the octahedral sites (yellow) are occupied by the randomly distributed Fe^{2+} and Fe^{3+} atoms giving an average valence value of +2.5 per Fe cation in octahedral site [24], [25].

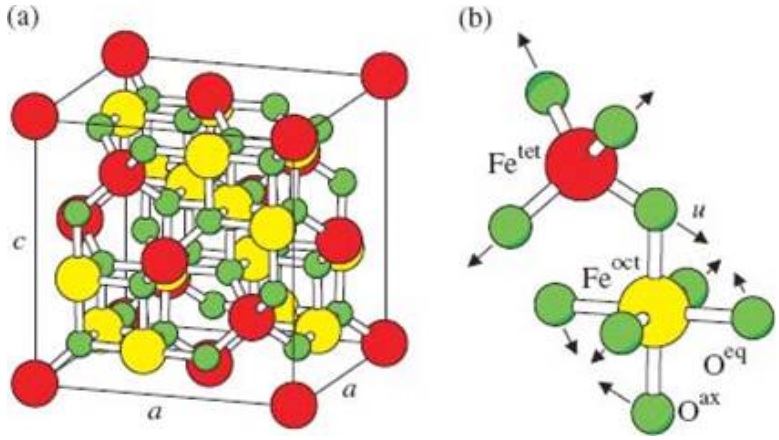

Figure 1.11: Inverse spinel structure of Magnetite. (reproduced with the permission) [26],

The signature property of Magnetite is the Verwey transition which is a metal to insulator transition at 125K [27], [28], [29]. It is believed that this transition is related to localization and delocalization of electrons at B sites. Above the Verwey temperature (T_v) hopping of extra electrons between Fe^{2+} and Fe^{3+} at octahedral

sites give higher conductivity to the magnetite. Below T_v, freezing of these extra electrons make the Fe^{2+} ions ordered at octahedral sites generating a structure where (001) planes are alternatively occupied by Fe^{2+} and Fe^{3+} ions. This ordering of ions decreases the conductivity by several orders of magnitudes resulting the Verwey transition [24]. Although this model is believed to be the most successful so far, the exact mechanism which governs the transport properties of magnetite is still unknown. The most important property of magnetite for the spintronics application is the half metalicity. That means at the Fermi level it only has one type of spins.(In this case it is spin down electrons). Therefore at the interface the material has 100% spin polarization [30]. This property together with the higher resistivity of magnetite make it an ideal candidate for spin injection process through reflection.

2 Experimental Details

This chapter consists of detailed explanations of all the experimental techniques used. Including sample preparation, thin film deposition and characterization techniques such as X-ray reflectivity, X-ray diffraction and Magneto optical Kerr effect (MOKE).

2.1 Making thin films

An AJA Orion Argon ion sputtering system was used to grow the films on selected substrates. Due to the nearly ideal lattice match, usually MgO(100) is the ideal substrate for magnetite film growth (lattice mismatch $< 0.3\%$). Before the deposition process, samples need to be cleaned well to get a good surface.

2.1.1 Sample Cleaning

Sample cleaning processes mainly depends on the substrate type. Our standard cleaning procedure consists with five steps. First, the substrates were sonicated for five minutes in soap water and then rinse with DI water until all the soap water is removed from the substrate container. Then sonicated again with DI water for five minutes to make sure those are free of soap stain. After that, to get rid of all the oily dirt on the substrates, those are immersed in acetone for five minute with the sonication. This followed by another five minutes of sonication with methanol to get rid of acetone and all the remaining dirt. Finally those cleaned substrates are blown off with nitrogen gas until all the methanol is being evaporated. This kind of cleaning is required for substrates like Si,SiO_x and Al_2O_3. But for MgO substrates,(which are

highly sensitive to the water),only the last three steps of the above process were used. That is, sonicate with acetone and methanol for five minutes in each and blow off with nitrogen gas to evaporate the methanol. Also care has to be taken in storing MgO substrates. Since those are highly sensitive to the water,they can react with the moisture in air. Those can be identified by white spots on the substrates. To prevent this issue MgO substrates were stored in a dry vacuum chamber. Previous studies have shown that annealing of MgO substrates at 800°C helps to obtain good MgO surface.

2.1.2 Sputtering

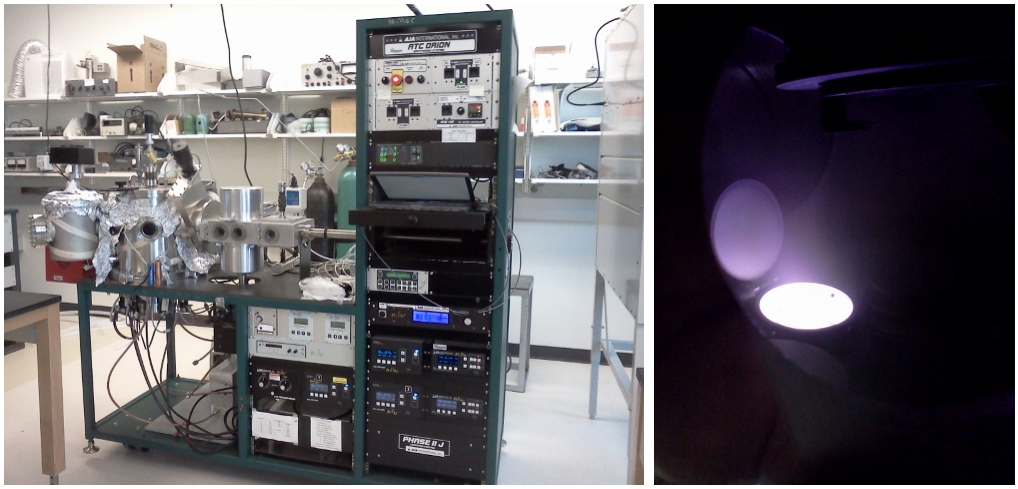

(a) Ar ion SputteringSystem (b) Ar ion Plasma

Figure 2.1: Argon Ion Sputtering System and Argon ion plasma

Sputtering is a method used to deposit thin films of a material on a given substrate. In our studies, we used an Argon ion sputtering system to deposit films. In the process of sputtering, Ar ions are accelerated onto a target material (thin film material) by creating an argon plasma closer to the target. Due to these accelerated ions target material starts to erode and ejects individual atoms through energy transfer into the deposition chamber. These ejected atoms usually travel in a path of a straight line. By placing a substrate at a certain distance,a thin film of the target material

can be obtained on the substrate. The mean free path of those sputtered atoms can be changed by varying the pressure inside the deposition chamber. When the pressure inside the deposition chamber increases, the ejected atoms undergo more and more collisions. This process decreases the deposition rate of the material onto the substrate. Most of our normal depositions were done at 3 mTorr pressure. The deposition rate also depends on the total power apply to the target material.

Pre-Sputtering Pre-sputtering is a process used to clean the target material prior to the deposition. Generally the sputtering chamber keeps under a high vacuum (10^{-8} Torr) to prevent all kinds of contaminations and reactions. But contamination and oxidation can still take place inside the chamber due to sputtering of other materials and use other gases. Therefore, pre-sputtering is a necessary step that should be done prior to all major depositions. It is done by covering the path between the target and the substrate by a metal piece (shutter), so that all the ejected atoms will deposit onto the shutter keeping the substrate clean. When all the unnecessary materials are removed from the target, the shutter can be opened to start the deposition. This can be identified by the input voltage(or the current) supply to the target material: the input voltage and current become constant once all the unnecessary materials are removed from the target.

2.1.3 Reactive Sputtering

In reactive sputtering, in addition to normal sputtering a chemical reaction is taking place inside the deposition chamber. This is done by adding reactive gases like oxygen and nitrogen in to the chamber in a controlled environment. Depending on the final product, the sputtering conditions like pressure, temperature and gas flow rates should be changed. In these studies, magnetite films were grown using reactive sputtering. Fe was sputtered in an oxygen environment. This was little harder due to the presence

of other oxides of iron like hematite(Fe_2O_3). Therefore, the exact reactive conditions had to be identified prior to each deposition. Also, if materials with higher reactivity (such as Gd) deposited prior to the reactive sputtering, those should be cleaned before start the deposition. Usual procedure is to fill up the chamber with O_2 gas and keep there for an hour, so that all the reactive materials will oxidise and will not absorb more O_2 during the deposition.

2.2 Structural Characterization

2.2.1 X-ray diffraction

X-ray diffraction is a non destructive and versatile characterization technique used on solid state materials and thin films. Properties like crystal structure, chemical composition, lattice parameters and other physical properties can be obtained using x ray diffraction technique. As shown in the Fig.2.2, the incoming X-ray beam is incident on to a stack of atomic planes in a thin film with a angle θ and reflected off with the same angle. The difference in path length between two consecutive X-ray beams is equal to $\Delta_1 + \Delta_2$. Therefore the difference in path length between two X-ray beams;

$$\Delta = \Delta_1 + \Delta_2 = 2d\sin(\theta)$$

For constructive interference the difference in path length should be an integer multiple of the X-ray wave length. So the $\Delta = n\ \lambda$ where n is the order of reflection and λ is the wave length of the X-ray radiation. All of the above equations leads to Bragg's equation.

$$n\lambda = 2d\sin(\theta)$$

Here d represents the distance between atomic planes and θ represents the angle between the x-ray beam and the surface of the sample. Different atomic planes have different inter atomic spacings (d values) and this leads constructive interference to occur at different θ values for each plane [31].

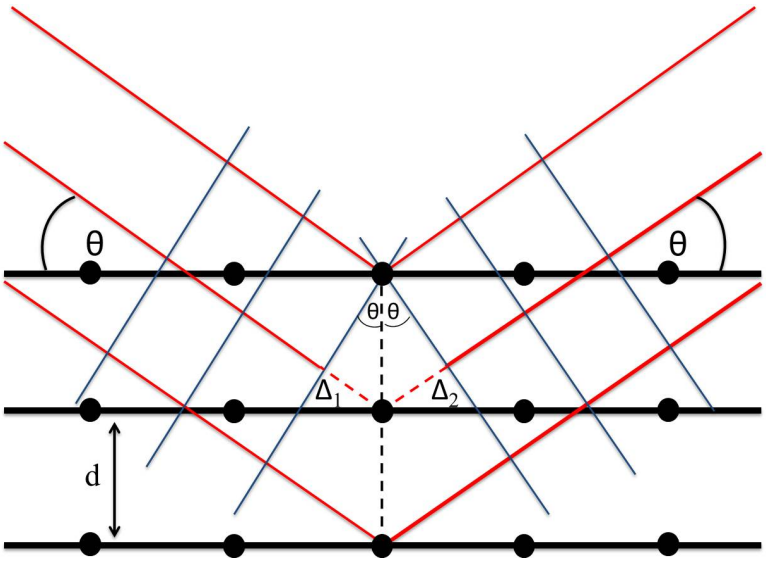

Figure 2.2: X-ray diffraction on a thin film

2.2.2 X-ray reflectivity

In this method the X-ray diffractometer works in a symmetric configuration, where both the X-ray source and the detector move in equal amounts. But it operates on lower angles compared to wide angle X-ray diffraction. This method can be used to determined the thin film thickness and surface and interface roughness [32] .

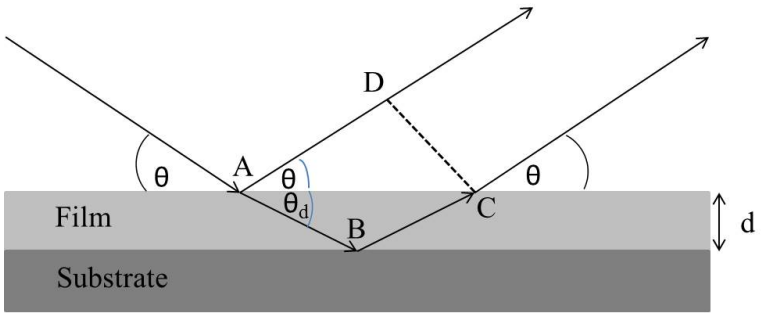

Figure 2.3: Reflected and refracted x ray beams from a thin film

In figure 2.3 the path length difference between AC and AD is equal to

$$\Delta = 2d\sin(\theta_d)$$

$$\Delta = 2d\theta_d = 2d\sqrt{\theta - \theta_c}$$

For constructive interference the phase shift should be equal to an integer multiple of the x-ray wave length (λ). For Cu k_α radiation the wave length is 1.54 Å.

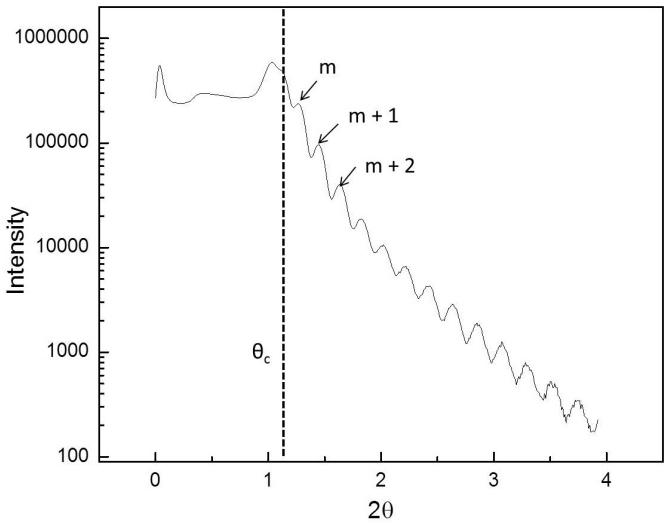

Figure 2.4: XRR scan of the Cr thin film

$$(m\lambda)^2 = (2d)^2(\theta^2 - {\theta_c}^2)$$
$$\theta^2 = (\frac{\lambda}{2d})^2 m^2 + {\theta_c}^2$$

The thickness of the film can be obtained by the slope of the θ^2 vs m^2 plot.

2.2.3 In plane X-ray diffraction (phi-scans)

This method is used to determine the in-plane orientation of the crystallites on thin films [33], [34]. In normal $\theta/2\theta$ scans, angles ϕ and ψ are set to be zero and the θ is changed between the given range. But in phi scans both ψ and θ were set up to constant values and the ϕ changes from 0° to 360 °.

Here the magnetite thin films can be used as a example. Due to the close lattice match and the thicker substrate peaks the Fe_3O_4 (200) peak is unresolvable in normal $\theta/2\theta$ scans. But using phi scans we can distinguish the MgO(220) peak from the substrate peaks. First the θ was set up to 43° where the Fe_3O_4 (002) peak was expected. Then ψ, the angle between the (002) peak and the (220) peak was set up to 25.2°. After that the ϕ was scanned from 0°to 360°.

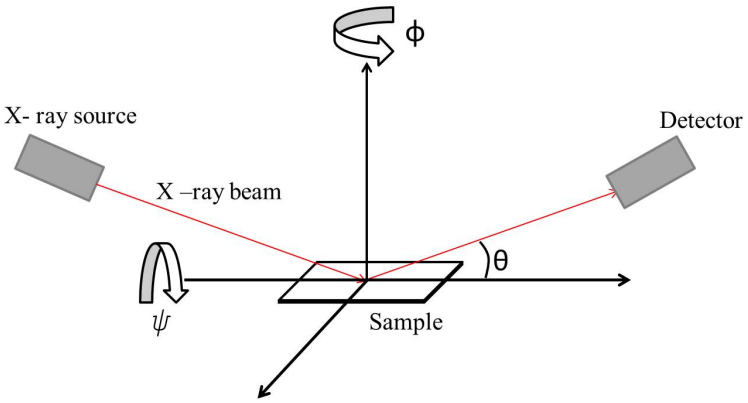

Figure 2.5: X-ray planes

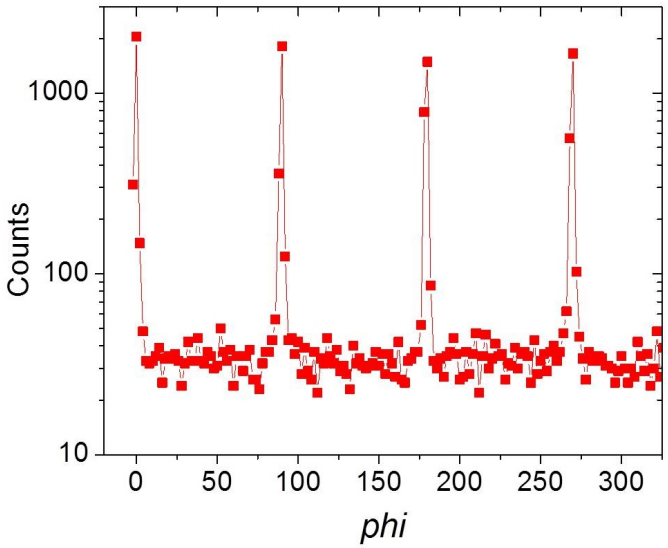

Figure 2.6: Phi scan of Fe_3O_4 (220) peak

2.3 MOKE magnetometry

MOKE (Magneto Optical Kerr Effect) is an optical technique that allows us to study the surface magnetization. It measures the intensity of a polarized light beam reflected off a ferromagnetic surface, which is proportional to the magnetization of the ferromagnet.

Figure 2.7 shows a schematic diagram of a MOKE set up. Here a laser beam was directed on to the sample through a polarizer. The polarization of the incoming beam

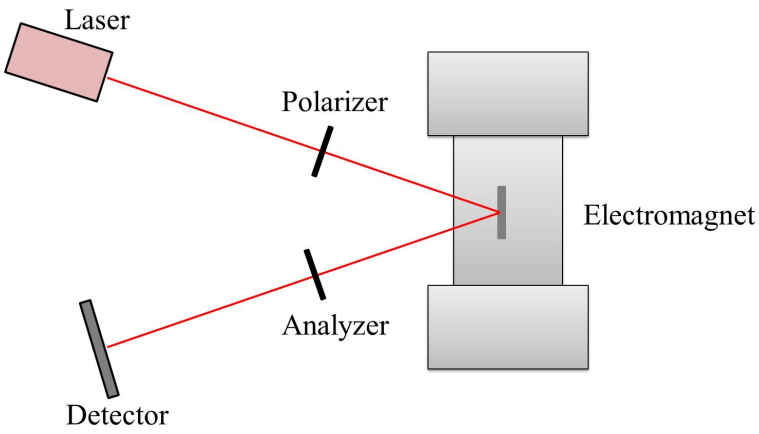

Figure 2.7: Schematic diagram of the MOKE set up

changes by the reflection off the sample. This change in polarization was converted in to a intensity change using an analyzer. Then the reflected beam was detected by a photo detector.In ferromagnetic materials the magnetization flips upon sweeping an external magnetic field. This change in magnetization can be detected as a change in light intensity in MOKE with same coercivities. Therefore MOKE is a simple and an accurate technique that can be used to study the coercivity related properties of ferromagnetic materials.

2.4 Magnetite Growth and Characterization

Magnetite thin films were grown by reactive sputtering. This method is chosen over depositing magnetite directly from a magnetite target due to the quality of the film. The magnetite deposited directly from the target showed Fe_2O_3 (Hematite), FeO and Fe peaks in addition to the Fe_3O_4 peaks in high angle X-ray diffraction.

The figure 2.8 shows the x ray diffraction data of the Fe_3O_4 target. Here, in addition to the Fe_3O_4 peaks Fe, FeO and Fe_2O_3 peaks can be identified. These extra peaks can be observed in the thin films grown from this target. But the magnetite grown through reactive sputtering only showed the magnetite peak Figure (2.10).

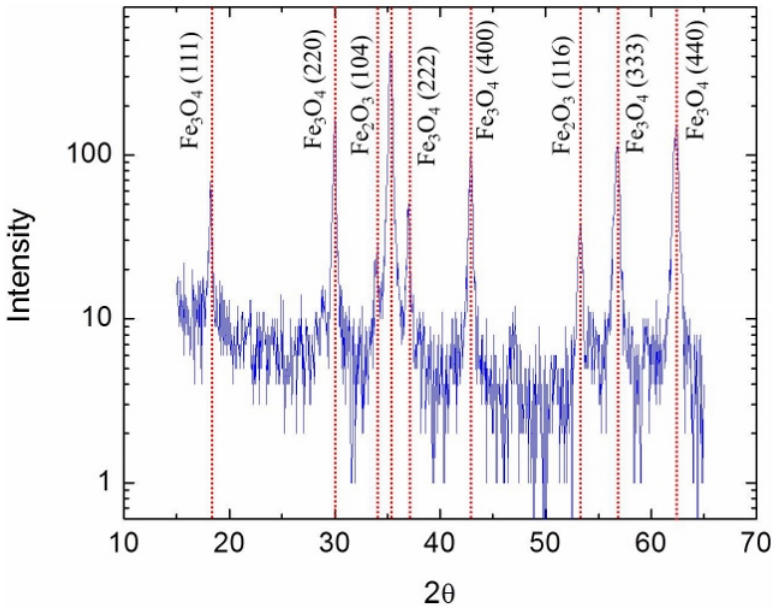

Figure 2.8: X ray diffraction data of a Fe_3O_4 target shows few Hematite (Fe_2O_3) peaks in addition to Fe_3O_4 peaks

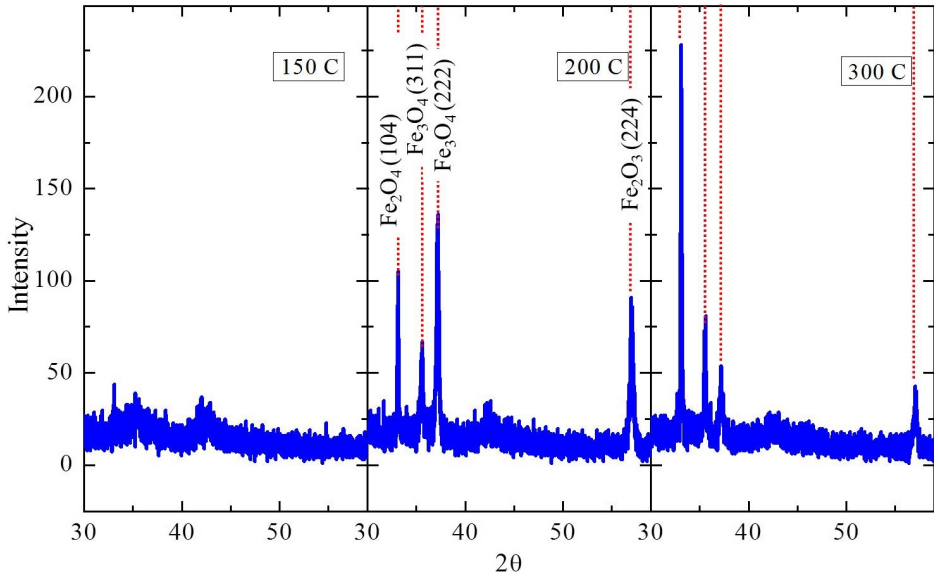

Figure 2.9: X ray diffraction of Fe_3O_4 thin films grown using Fe_3O_4 compound target at different temperatures on glass substrates.

The process of reactive sputtering is highly sensitive to the amount of O_2 in the chamber. Presence of other reactive materials in the deposition chamber walls from

the prior depositions can reduce the amount of usable O_2 and affect stoichiometry of the magnetite (especially materials like Gd and Ta). Therefore, prior to the deposition all the high reactive materials were removed from the deposition chamber.

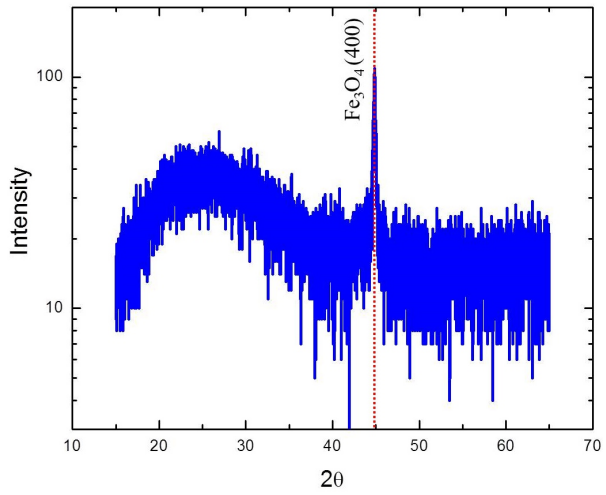

Figure 2.10: X ray diffraction of Fe_3O_4 thin films grown by reactive sputtering at 300°C on glass substrates

The most important and time consuming part of the reactive sputtering was finding the correct deposition parameters. Here the deposition power, pressure, temperature and the Ar flow rate were kept constant and the O_2 flow rate was changed until the correct recipe was found. When growing magnetite the sample holder was heated to 300 °C and left idle for 15 minutes, so that the temperature would be uniformly distributed through the sample holder. Then the Fe plasma was sparked using a radio frequency (RF) power source at 200 W and allowed to pres putter for 15 minutes. The total pressure of the chamber was controlled through the position controller. The position of the gate valve was set up to 380 (VAT position), so that the total pressure of the system would be 10 mTorr with 20 SCCM Ar flow. Then the O_2 flow was switched on with a flow rate of 0.51 SCCM, which we found to be the optimum flow rate. After opening the O_2 flow, it's necessary to wait at least 2 minutes before the real deposition. This gives enough time for the system to equilibrate. The sample

holder was rotated at a speed of 40 rpm to obtain a uniform film thickness. Finding the correct recipe can take from couple of days to couple of weeks.

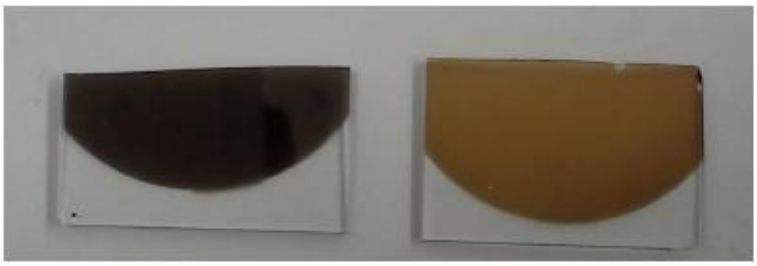

Figure 2.11: Magnetite (left) and Hematite (right)

The magnetite films can be identified easily by looking at them. If the stoichiometry is correct, then the resultant film will be black in color. If the O_2 amount is too low, then the film will look like a normal metal Fe film. If the O_2 amount is too high the film will become reddish brown due to hematite (Fe_2O_3). To fine tune the recipe, we used the Verwey transition (T_v). If the stoicheometry is perfect, the Verwey transition should occur around 125K for thick films. When the stoichiometry deviates from the ideal value the T_V, namely $Fe_{3-\delta}O_4$ with δ less than 10^{-3} [35].

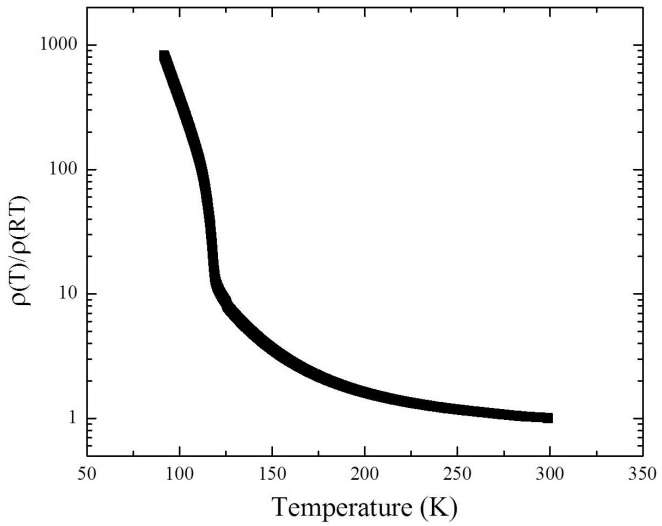

Figure 2.12: R vs T diagram of 300nm of Fe_3O_4 grown on top of MgO (100) substrates shows sharp Verwey transition at 120K.

In measuring the Verwey transition, the magnetite sample was connected to a resistivity measuring probe and pseudo four point measurement was used to obtain the resistance. Then the probe was slowly dipped into a liquid Nitrogen dewar to prevent thermal lag during the cool down and the resistance of the sample was measured simultaneously. All the Fe_3O_4 films we grew showed the Verwey transition in between 119 K to 125 K, which suggests the stoichiometry was Fe_3O_{4-x}. Figure.2.12 shows the change in resistance in magnetite as a function of temperature. The Verway transition can be seen around 120K. The epitaxy of the magnetite was confirmed by X-ray diffraction measurements. Higher orders of magnetite peaks can be distinguished

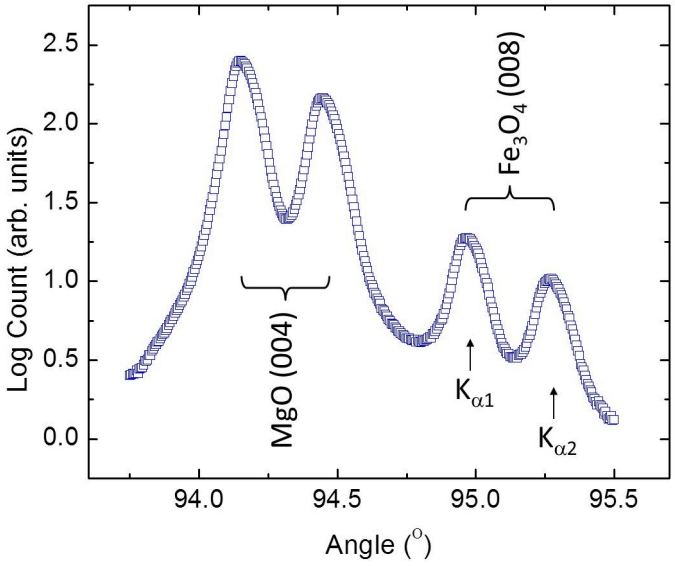

Figure 2.13: High angle x-ray of magnetite thin film at higher angles

from the MgO substrate peaks using high angle x ray diffraction. Figure 2.13 shows the Fe_3O_4 (008) peak and the MgO (004) peak at higher angles. Each peak has two maximums resulted from Cu K_α radiation.

Figures 2.14 and 2.15 shows the phi scans carried out focusing (311) and (220) orientations. First a $\theta/2\theta$ scan was carried out focusing the MgO(002) peak which is overlap with the Fe_3O_4 (004) peak. The MgO(002) peak was observed at 43.06°. Then the θ was fixed to 43.06°. Then the angle between the Fe_3O_4 (004) and (220)

planes was calculated to be 25.2°. So that the ψ was fixed at 25.2°. Finally the angle ϕ was changed from 0 °to 360°to obtain the ϕ scan. Same procedure was repeated for the Fe_3O_4 (311) peak. In this case the ψ was set to 35.47°.

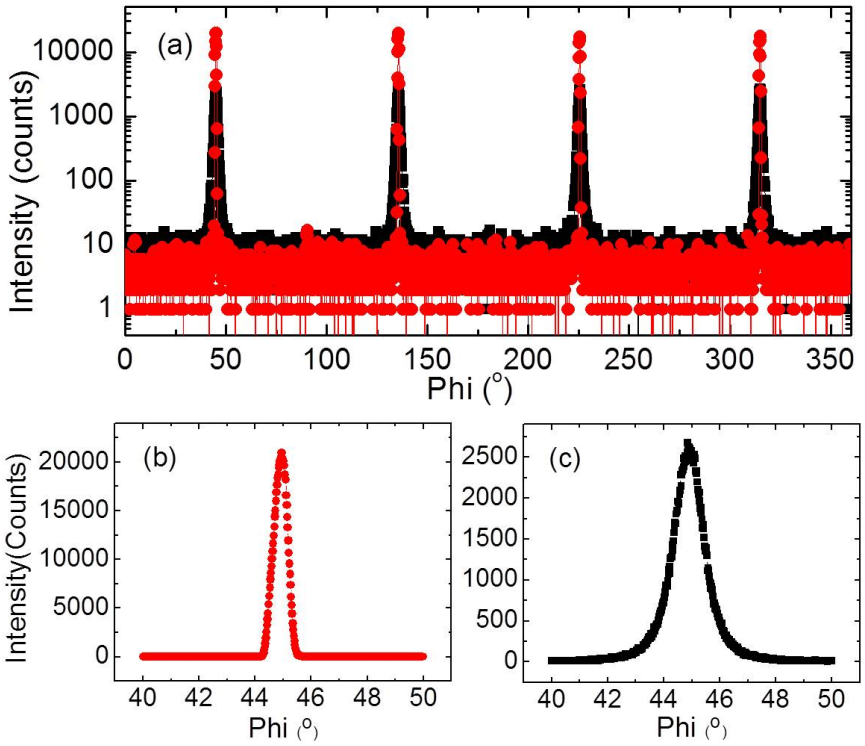

Figure 2.14: Phi scan of MgO and Fe_3O_4 (311) peaks. (MgO(311)-red, Fe_3O_4 (311) - black), (b) and (c) shows the focused scans of (311) peaks of MgO and Fe_3O_4.

Figures 2.14 and 2.15 confirm the epitaxial growth of magnetite on MgO(100) substrates. Figures 2.14(b) and (c) show the high resolution figures of (311) peaks of MgO and Fe_3O_4 respectively. The full width at half maximum (FWHM) of MgO(311) and Fe_3O_4 (220) were 0.56° and 1.34° respectively. Theoretically, the substrates peak should be a delta function with zero FWHM. But, due to the instrumental broadening, they showed finite FWHM for the substrate peaks. The magnetite (311) peak has slightly broadened FWHM compared to the MgO FWHM due to the finite size effect. Fe_3O_4 (220) peaks also show the same kind of behaviour. Figure 2.15 shows the (220) peaks of Fe_3O_4 and MgO. Here the Mgo (220) peak has a FWHM of 0.38°. and the Fe_3O_4 (200) has a FWHM of 1.36°. These low FWHM values confirms the quality of

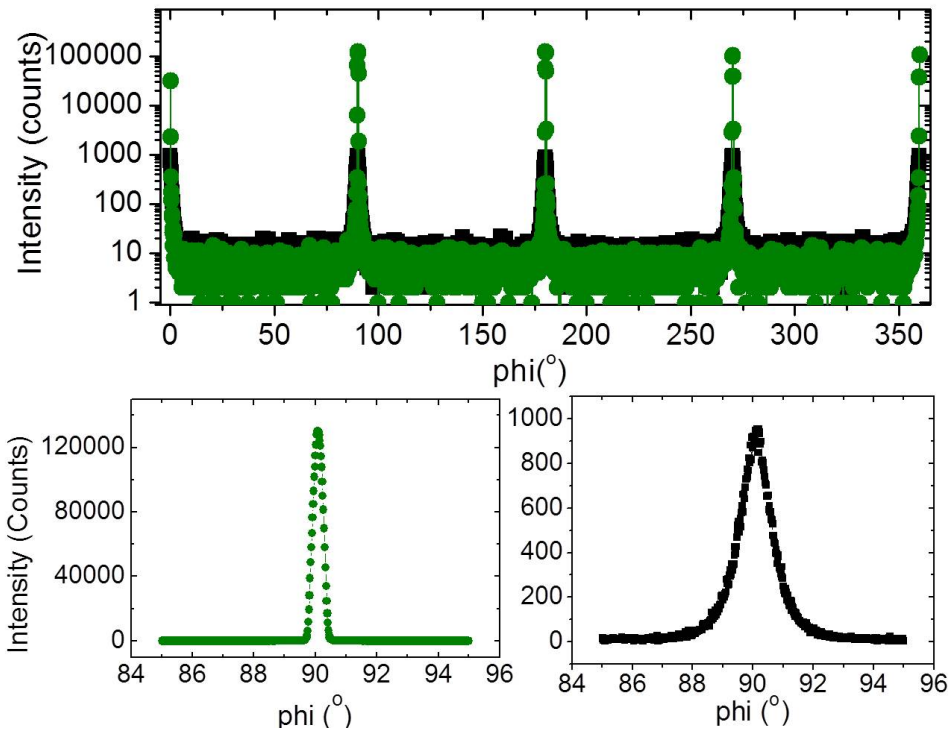

Figure 2.15: Phi scan of MgO and Fe_3O_4 (220) peaks. (MgO (220)-green, Fe_3O_4 (220) - black), (b) and (c) shows the focused scans of (220) peaks of MgO and Fe_3O_4.

the magnetite films grown on top of MgO(100) substrates.

3 Impact of transition metal buffer layers on magnetite thin films

3000 Å Fe_3O_4 (magnetite) thin films were simultaneously grown on (001) MgO single crystal substrates with and without 30 Å buffer layers of Fe, Cr, Mo, and Nb. Then the effect of these buffer layers on structural, magnetization and transport properties of Fe_3O_4 was studied. All the transition metals showed epitaxial growth on MgO (100) substrates. We observe highly oriented (001) Fe_3O_4 with Mo and no buffer layer, reduced (001) texture with Nb and Fe, and polycrystalline growth with Cr. Mo, Cr, and unbuffered magnetite show typical magnetic behavior, whereas Nb and Fe buffers lead to anomalous magnetic properties that may be due to interfacial reactivity.

3.1 Sample growth

All the films were grown in an Ar ion sputtering system with a base pressure of 20 nTorr. Ultra high purity gases were used for all the deposition. Samples were rotated at a speed of 40 rotations per minute during the deposition to obtain uniform film thickness. The most important step of the growth process is using the mask exchanging apparatus located in the load lock. This allows us to change the masks in between depositions without breaking the vacuum (Pressure rises to 200 nTorr when load lock is opened), so that the samples will not be exposed contaminants. This is an important capability to have when you need clean interfaces. In this experiment using this *in situ* mask exchanging apparatus 30 Å of four different transition metal buffer layers, namely Fe, Cr, Nb and Mo were grown separately on individual MgO substrates and one substrate was kept without any buffer layers. The transition metals

were grown at 300°C at 3 mTorr pressure with the Ar flow rate of 20 SCCM. At DC power of 100 W the depositions rates for Fe, Cr, Nb and Mo were 0.65, 0.68, 0.80 and 0.85Å/s respectively. After the buffer layer depositions, the mask was completely removed and 3000 Å of Fe_3O_4 was deposited on all the substrates simultaneously. The magnetite was grown by reactive sputtering of Fe in an O_2 environment as described before. After the Fe_3O_4 deposition, 30Å of Cr was deposited on all the samples as a capping layer to prevent oxidation [36].

3.2 Structural Characterization

3.2.1 Buffer layer material

As a controlled experiment we also grew 3000 Å of transition metals on MgO(100) substrates at 300°C. Then the high angle x ray diffraction was carried out to determine the structure of the films.

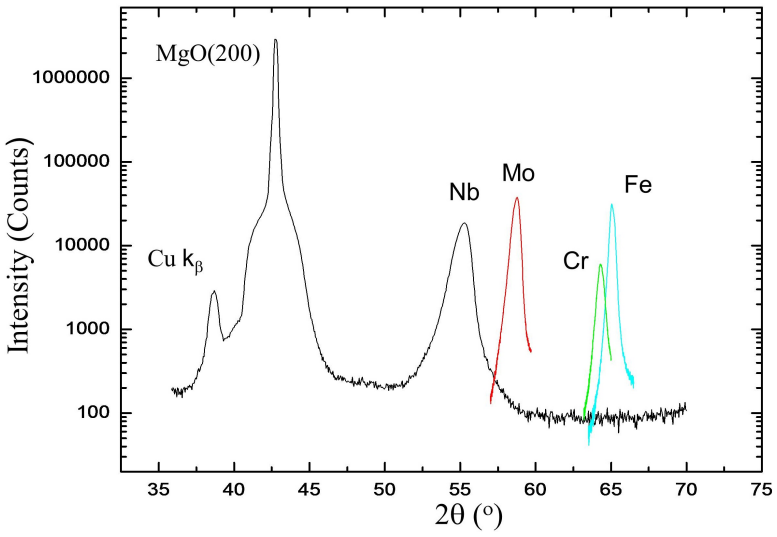

Figure 3.1: Wide angle x-ray diffraction measurements of MgO(001) /TM(3000 Å)

Figure (3.1) shows high angle x-ray diffraction data for MgO(001) /TM(3000 Å) grown at 300 °C. To understand the structural coherence of the films rocking curves were obtained around (200) peak.

Figure (3.2) shows the mosaic spreads of 3000 Å thick Mo, Cr and Fe thin films

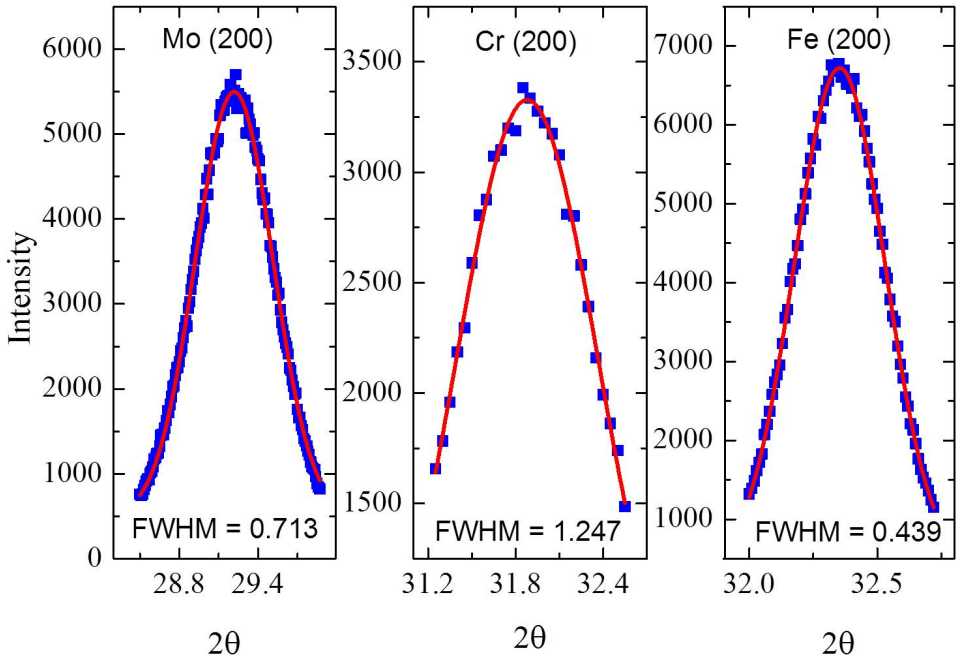

Figure 3.2: Mosaic spreads of (200) peak of Mo Cr and Fe layers on MgO(100) substrates)

on (200) peak. Low full width at half maxima of mosaic spreads suggests the good structural coherence in (100) direction.

Figure 3.3 shows x-ray diffraction scans of four buffer layer samples MgO(001) /TM(30 Å) / Fe_3O_4 (3000 Å) /Cr(30 Å), where TM=Nb, Mo, Cr, and Fe and one with no buffer (denoted N/A). Here,the magnetite (400) peak is coincides with the MgO (200) peak due to their nearly perfect lattice match. These cannot be distinguished because of the higher intensity of the MgO(100) peak due to it's larger thickness. A low intensity peak was observed around 54° in all samples, with the exception of the uncapped samples. This low intensity peak was identified as Fe_3O_4 (422) peak, which originates from the 30 Å of Cr capping layer. This suggests that the Cr capping layer affects the top surface of the magnetite. In addition to this peak Fe_3O_4 (311), (222), (333) peaks can be observed on the Cr buffered sample. These multiple orientations indicate that the Cr buffer layer leads to polycrystalline magnetite growth. All the

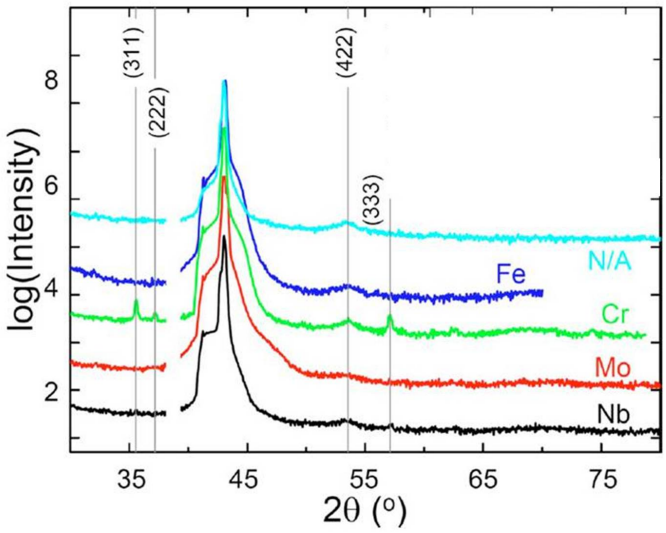

Figure 3.3: Wide angle x-ray diffraction measurements of MgO(001) /TM(30 Å) /Fe_3O_4(3000 Å) /Cr(30 Å). Each curve is labeled by its buffer layer.

other buffer layer samples didn't show any peak in addition to the MgO(200) peak, which suggests that they lead to strong (100) oriented Fe_3O_4 growth. Also we didn't observe any of the transition metal (100) peaks due to their thicknesses.

Figure. 3.4 shows that high angle X-ray diffraction on the buffer layered samples reveals that the high orders of MgO and Fe_3O_4 can be separated easily. The (004) peak of MgO is in the left of the graph and the (008) peak of the Fe_3O_4 is in the right of the graph. The peaks appear as doublets because of the Cu $K_{\alpha 1}$ and $K_{\alpha 2}$ wavelengths. Comparing the relative intensities, it's possible to conclude that the Mo and unbuffered samples give strong (008) texture to the magnetite. Also the Mo buffered peaks were shifted towards the MgO(400) peaks, suggests that the release of the strain of the system. Rocking curves of MgO(400)and the Fe_3O_4 (800) have 0.055° and 0.079° full width at half maximum, respectively, which implies low mosaic spread. This means the peaks are broadened due to the limitations of the instrument. There are no (008) peaks observed on Cr buffered sample. It might be due to the poor structure gives by the Cr buffer layer. Nb buffered sample shows relatively low intensity (008) peaks, but clearly observable. Those peaks also shifted toward

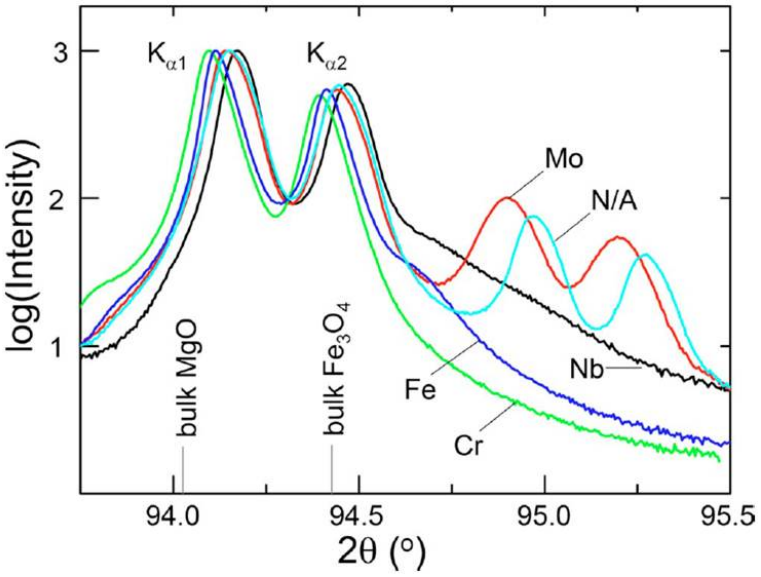

Figure 3.4: Resolved MgO and Fe_3O_4 diffraction peaks for higher order reflections.

the MgO (400) peak releasing the strain of the system. In Fe buffered sample only Fe_3O_4 (008) $K_{\alpha2}$ peak is observable, suggesting that the Fe_3O_4 (008) $K_{\alpha1}$ peak is coincident with MgO(400) $K_{\alpha2}$ peak. This implies that magnetite grown on Fe buffer layer is almost strain free compared to the bulk magnetite. This might cause the reduced density of anti-phase boundaries [37] in magnetite by the Fe buffer layer. We calculated the stress parameters for Nb, Mo and unbuffered samples relative to the bulk magnetite(d_{bulk} = 8.3967Å). By applying the θ value for Fe_3O_4 (008) peak obtained by the high angle X-ray data into the Bragg's equation ($2d\sin(\theta) = n\lambda$) lattice parameters of Fe_3O_4 grown on different buffer layers were calculated. The stress parameter was calculated using the difference between those calculated lattice parameter and the bulk lattice parameter. They are -0.26%, -0.38%, and -0.44% for Nb, Mo and Unbuffered samples, respectively. While the films are slightly strained relative to the bulk, the fact that the (008) peaks are instrumentationally broadened for Mo and N/A samples suggests that the d-spacing in the momentum transfer direction is uniform throughout the films thickness. It is difficult to conclude the same for the Cr, Nb and Fe samples [38]. The Fe buffered sample seems to be between

these limits, but we cannot say this with confidence unless they are measured on a better diffractometer.

Table 1: X ray data analysis

Film	t(Å)	a_0(Å)	a(Å)	ϵ(%)	Brag FWHM(°)	Rocking FWHM (°)
Nb	300	3.30	3.32	0.64	(002) 0.79	(002) 1.69
Mo	300	3.15	3.14	-0.24	(002) 0.46	(002) 0.63
Cr	300	2.91	2.90	-0.52	(002) 0.41	(002) 1.00
Fe	300	2.87	2.87	0.00	(002) 0.32	(002) 0.36
Fe_3O_4	3k	8.397	8.360	-0.44	(008) 0.118	(008) 0.079
Mo/Fe_3O_4	30/3K	8.397	8.365	-0.38	(008) 0.135	(008) 0.055
Cr/Fe_3O_4	30/3K	8.397	poly	(111), (311), (222), (422), (511), (440), (622)		
Fe/Fe_3O_4	30/3K	8.397	poly	(111), (311), (222), (422), (511), (440), (622)		
Nb/Fe_3O_4	30/3K	8.397	poly	(111), (311), (222), (422), (511), (440), (622)		

3.3 Effect of transition metal buffer layers on Verwey transition

Resistivity measurements were carried out to determine the effect of the transition metal buffer layers on the Verwey transition, as shown in Figure 3.7. Since the magnetite was grown on all the samples simultaneously, any differences in resistivities should be due to change caused by the buffer layer. In measuring the resistivity, we attached the samples to the measurement probe using double sided tape. Bigger samples (samples grown on glass slides) were diced into smaller sized samples, so that they would fit into the sample stage. If the substrate was completely covered with the deposition material it was scribed in to long skinny lines using a diamond-tipped scribe. Due to the high resistivity of magnetite, two point resistivity measurements were carried out. Wires were connected onto the sample using pressed indium con-

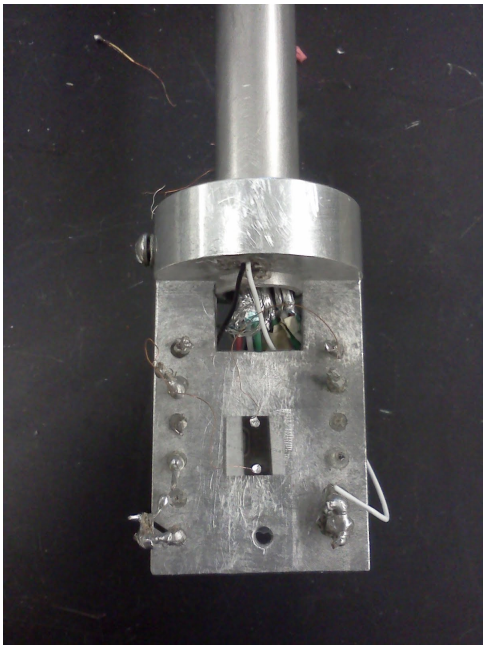

Figure 3.5: Resistivity measuring probe with a sample connected

tacts. Care should be taken while pressing the indium onto the sample, because extensive pressing can result cracks on the sample, which will break the conduction path.

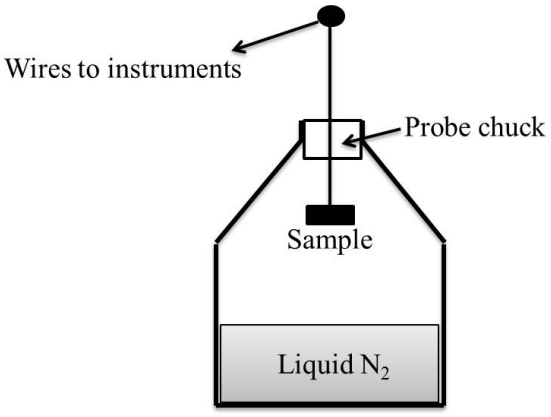

Figure 3.6: Resistivity vs temperature measuring set up

For temperature dependent measurements, the probe was partially dipped into a liquid nitrogen bath, allowing the sample temperature to cool from 300 K down to about 100 K in about 30 minutes. The resistivity is measured as the sample cools

down: the cooling rate is made sufficiently slow that no thermal lag is noted with subsequent warming.

The unbuffered magnetite shows the sharpest Verwey transition, with an increase in resistivity of more than an order of magnitude in just a few degrees. Cr, Fe, and Nb buffered samples showed higher transition temperatures than the unbuffered magnetite, but the transition was not sharp. This shift in the transition temperature may be due to the stress created from these buffer layers on the magnetite layer, or possibly the formation of an interfacial layer between the buffer and the magnetite (e.g., if the buffer became oxidized by reducing the magnetite, then the interfacial magnetite may have its stoichiometry altered).

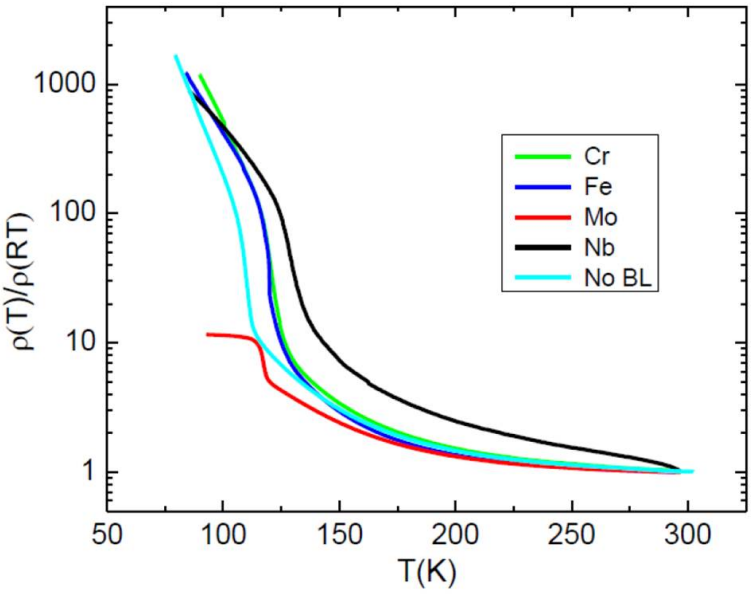

Figure 3.7: Change in resistivity as a function of temperature for magnetite simultaneously grown on different transition metal buffer layers, relative to the room temperature resistivity.

The Mo-buffered sample showed a transition point closer to the unbuffered sample, but the resistance saturates, unlike any other samples we investigated. We hypothesize this being due to the formation of conduction paths at grain boundaries; indeed, force microscopy images show that the Mo-buffered samples topography is

quite granular due to the formation of magnetite nanoparticles rather than a film. Additionally, these grains appear to have magnetic switching events during magnetic force microscopy that are caused by sample-tip interactions. This indicates the formation of grains that are weakly coupled to their neighbor [39].

3.4 Magnetization Measurements

Superconducting quantum interface device (SQUID) magnetometry was used for the magnetization measurements. After saturating the Samples at 300 K to 30 kOe, zero field cooled magnetization measurements were carried out along (100), (010) and (001) directions at 10 Oe applied field.

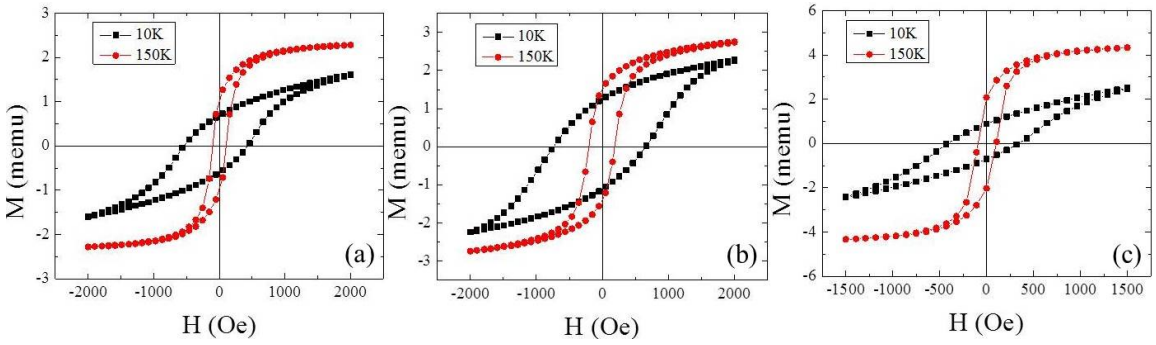

Figure 3.8: M Vs H loops for un-buffered, Cr and Mo buffered Fe_3O_4 samples at 10K and 150K along (100) direction

Magnetic hysteresis loops were also measured on those samples at various temperatures out to fields of $\pm 5\ Oe$. Figure 3.8 shows hysteresis loops of un-buffered, Cr and Mo buffered magnetite samples along the (100) direction at temperatures above (150 K) and below (10 K) the Verwey transition. All the samples show similar behaviour, with enhanced coercive and saturation fields at low temperatures. There is also a shearing of the low-temperature loops below the Verwey transition. This is a result of the rotation of the easy axis above and below the Verway transition due to the temperature dependent magnetic anisotropy.

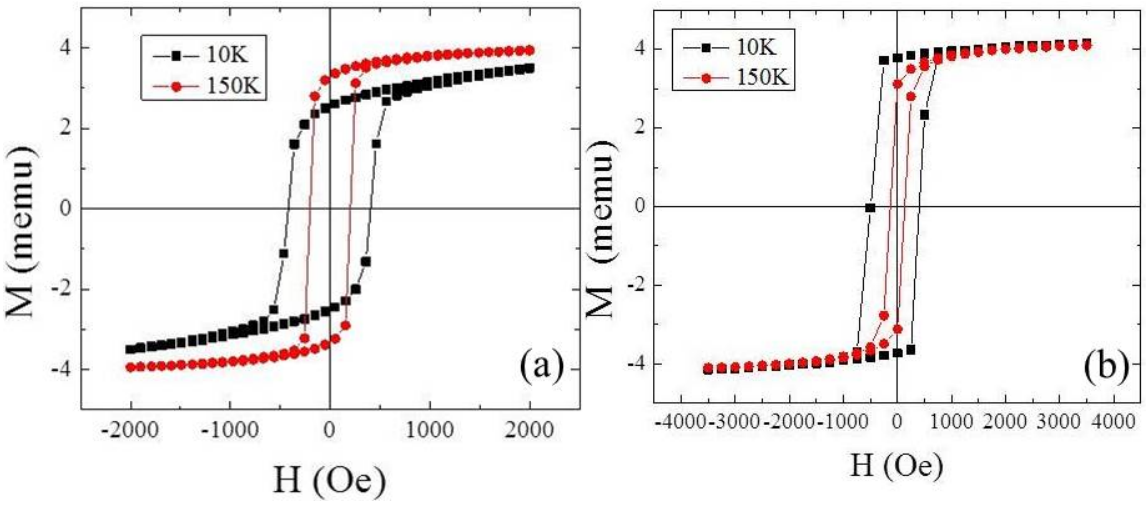

Figure 3.9: M Vs H loops for Nb and Fe buffered Fe_3O_4 samples at 10K and 150K along (100) direction

Fe and Nb-buffered samples also show an increasing coercivity at low temperatures. Nb buffered sample doesn't show any shearing at low temperature. Fe buffered sample shows slight shearing at 10K. But the shape of the loop is not as dramatically changed like in other buffered and unbuffered samples. These differences in magnetization measurements in Fe and Nb buffered samples might be related to their relatively high reactivity. It's possible that at the initial stages of reactive sputtering Fe and Nb becoming oxidized themselves. During this process those might have reduced the magnetite at the interface giving a different stoichiometry in the form of (Nb/Fe) $O_x - FeO_x$. This clearly leads to significant change in magnetic properties [40].

The temperature dependence of the magnetization was measured on all the magnetite samples with buffer layers along two in plane directions (100), (010) and out of plane (001) direction. All the samples exhibited change in magnetization around 120K indicating the good stoichiometry of Fe_3O_4.

In all the samples a change in magnetization was observed around 120 K. Along (001) direction, the magnetization values were relatively low indicating that the easy

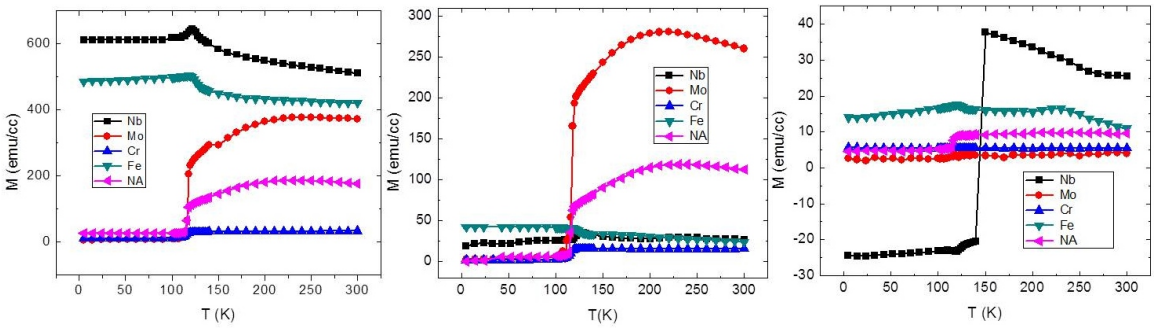

Figure 3.10: Magnetization measurements of Fe_3O_4 on buffer layers along (a)(100), (b)(010) and (c)(001) directions.

axis of the samples remains in-plane through out the transition. The largest magnetization values were observed along the (100) direction. Relatively bigger signals were also observed along the (010) direction. According to the easy axis of the samples were between (100) and (010) directions. Mo, Cr and un-buffered Fe_3O_4 samples showed a sharp drop in magnetization below the Verwey transition similar to the bulk Fe_3O_4. In Nb and Fe buffered Fe_3O_4 samples, the transition is relatively suppressed compared to other samples. This may be due to the formation of inhomogeneous oxide layer at the interface by absorbing O_2 from the Fe_3O_4 layer.

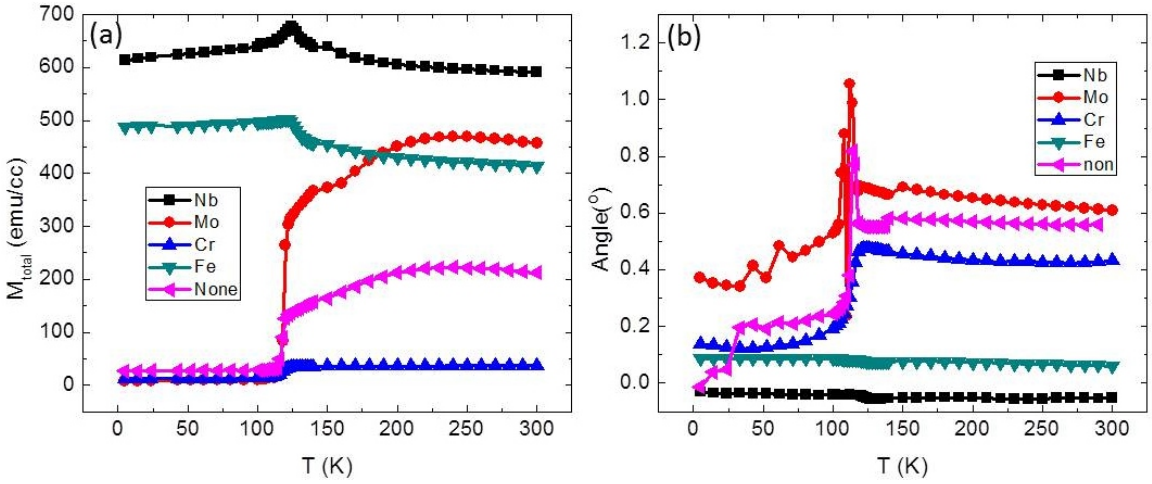

Figure 3.11: Total magnetization (a) and the angle (b) of Fe_3O_4 on different buffer layers .

Using the above data the total magnetization and the magnetization angle with

respect to the (100) direction were calculated separately for all the samples using following equations (fig.3.11):

$$M_{total}^2 = M_{100}^2 + M_{010}^2 + M_{001}^2$$
$$\theta_{total} = cos^{-1}(M_{100}/M_{total})$$

Cr, Mo buffered and un-buffered Fe_3O_4 samples showed similar magnetization behavior with respect to temperature. They all showed sharp magnetization drop at Verwey transition. Fe and Nb both showed significantly higher magnetization values compare to other samples and their change in magnetization was suppressed at the Verwey transition.

A Change in the magnetization angle was observed in Cr, Mo and unbuffered Fe_3O_4 samples. This indicates that the magnetic anisotropy is temperature dependent and it leads to temperature dependence rotation of easy axis above and below the Verway transition. Similar behavior was reported in past on bulk magnetite [41] but has not been observed in films. Measurement with a vector magnetometer should clarify these observations.

We also were able to calculate the approximate angle $\vec{M}_{Total}$ makes relative to the (100) direction using M_{Total} vs T data.

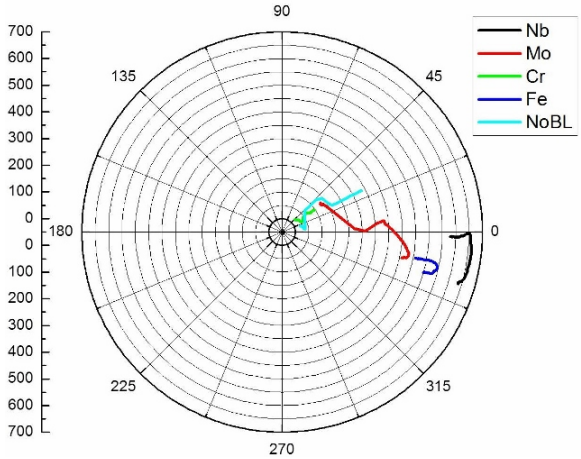

Figure 3.12: Change in total magnetization angle with respect to the (100) direction

Figure 3.13 shows the temperature dependence of magnetization on same set of samples along the (110) direction. Mo, Nb, and un-buffered samples show higher magnetization values above the Verwey temperature relative to the (100) direction. This indicates that the easy axis of all above samples are closer to (110) direction than (100) direction. A drop in the total magnetization was observed in Nb and Fe buffered Fe_3O_4 samples. However they showed considerable change in magnetization compared to (100) direction.

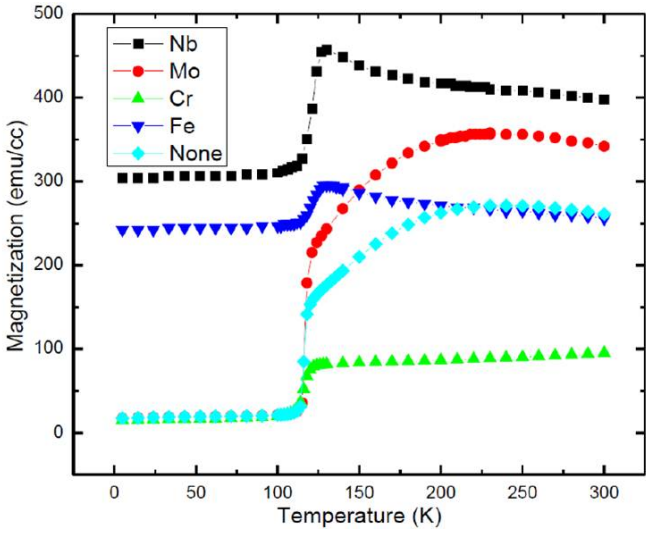

Figure 3.13: Magnetization of Fe_3O_4 on different buffer layers along (110) direction

3.5 Magnetic Force Microscopy on unbuffered Magnetite thin films

3.5.1 Magnetic Force Microscopy

Magnetic Force Microscope (MFM) produces a two dimensional map of magnetic surface. Here a small magnetic tip mounted on to a cantilever spring places very close to the surface of the magnetic sample. Using this magnetic tip the magnetic stray fields from the sample is detected. The magnetic force on the tip is calculated by measuring the displacement at the end of the cantilever. This is measured by a

deflection sensor, which uses a reflection of a laser beam off the cantilever end.

Considering the magnetic tip as a point dipole with magnetization oriented perpendicular to the sample plane, the potential energy (U) of the tip sample system is defined as:

$$\mathrm{U} = -m_z B_z(\vec{r_{tip}})$$

Where m_z is the magnetic moment of the tip and B_z is the stray field from the sample.

The force on the magnetic tip as a function of distance can written as:

$$\vec{F}(\vec{r}) = -\vec{\nabla}U = m_z \vec{\nabla} B_z(\vec{r_{tip}})$$

$$\vec{F}(\vec{r}) = m_z \left(\frac{\partial}{\partial x}\,\hat{x} + \frac{\partial}{\partial y}\,\hat{y} + \frac{\partial}{\partial z}\,\hat{z}\right) B_z(\vec{r_{tip}})$$

by assuming the motion of the tip is constrain to the $\hat{z}$ direction, the vertical force act on the magnetic tip by the sample stray fields can be reduced to

$$\vec{F}(\vec{z}) = m_z\left(\frac{\partial B_z}{\partial z}\right)$$

According to this equation the force on the tip is proportional to the field gradient. In magnetic thin films the field gradient is higher at the domain edges. Therefore high contrast can be obtain at the edge of the domains.

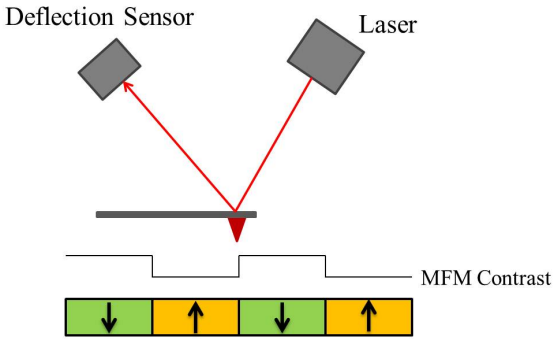

Figure 3.14: Mechanism of Magnetic Force Microscope

By scanning the cantilever over the sample in a raster style an image of magnetic domains on the surface of the sample can be obtained.

3.5.2 Magnetic Force Microscopy on Magnetite thin films

In this study the temperature dependence of magnetite thin films was studied using SQUID and MFM. Previous studies have shown that formation of anti phase boundaries (APB) on magnetite thin films. These APBs have out of plane magnetization due to anti-ferromagnetic coupling. This make MFM a perfect candidate to study the micro magnetic nature of magnetite thin films. Prior MFM studies have reported on magnetite in room temperature [42]. But our probe has the unique ability to perform the MFM as a function of temperature. This allowed us to study the magnetic structure of magnetite during the Verwey transition. For these measurements the films from the buffer layer study were used.

3.5.3 MFM on Unbuffered Fe_3O_4thin films

Here a 3000Å thick Fe_3O_4sample directly deposited on to the MgO(100) substrate was used. First, SQUID measurements were performed on the sample. The sample was saturated at 30kOe field along (100) direction and zero field cooled to 10K. Then the magnetization was measured from 10K to 300K in 10K discrete steps. Measurements were performed on (100),(010) and (001) directions.

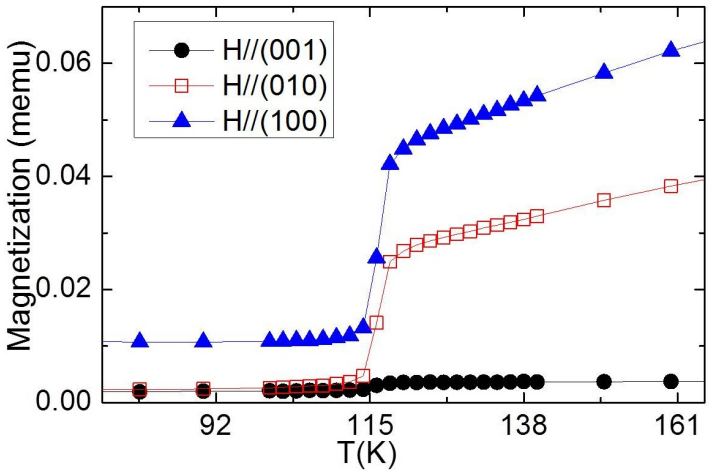

Figure 3.15: Magnetization Vs Temperature of Fe_3O_4thin films along (100),(010) and (001) directions

According to the figure(3.15) magnetization along (100) and (010) directions show higher values above the Verway temperature. The magnetization along (001) plane was remained low above and below Verway temperature. This indicates that the magnetization of the sample lies in plane of the sample. By considering the different magnetization values along above three directions, samples net magnetization is calculated to be 32°from the (100) axis. The highest magnetization value along (100) direction indicates that the sample has developed a slightly preferred direction along this axis.

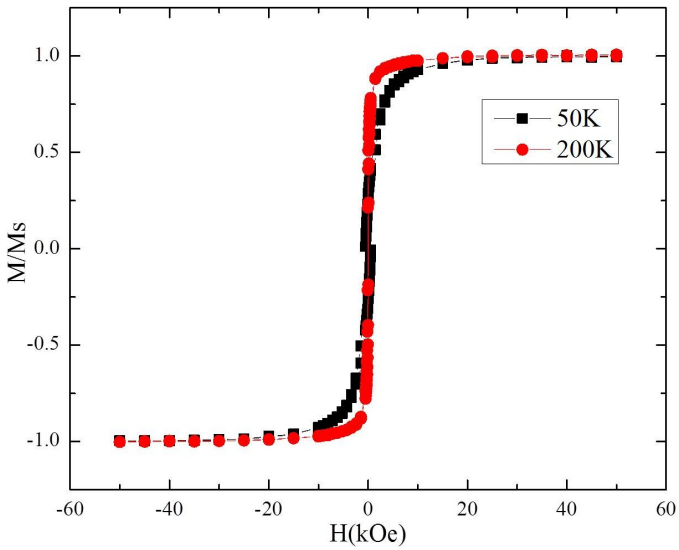

Figure 3.16: Magnetization Vs field curves of Fe_3O_4at 200K and 50K

Figure(3.16) shows the magnetization vs field curves for magnetite at 20K and 50K. The magnetization at 50K is deviated from the 200K. This might be due to the rotation of magnetization below the Verway transition. Other notable fact is that the samples haven't reach the saturation until 20kOe field. This indicates the presence of anti phase boundaries in the sample.

MFM images were acquired using a custom built scanning force microscope. To obtain topographic and resonant frequency images a commercial NanoScope IIIa controller with an extended module was used. The microscope has the ability to acquire

images at a particular location for a wide range of temperatures. The scanning window was selected by visually matching the features of the topological image during of data acquisitions.

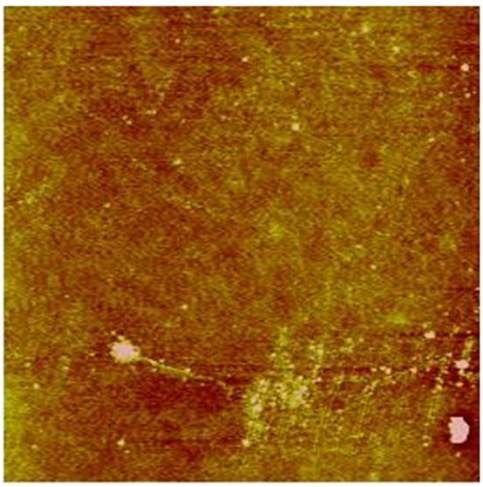

Figure 3.17: Topological image of Fe_3O_4surface at 120K

Figure(3.17) shows the topology of the area selected for MFM on surface of a magnetite film at 120K. First set of MFM images were acquired during the temperature sweeps through the Verway transition. Temperature was swept from 135K to 77K in 10K steps.

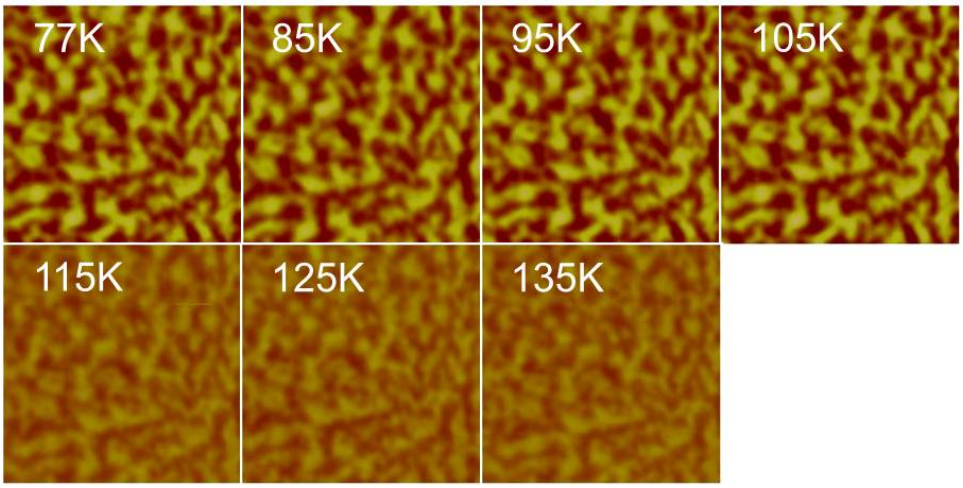

Figure 3.18: MFM images of Fe_3O_4thin film through Verway transition

Figure(3.18) shows the MFM images of Fe_3O_4during the Verway transition. The dark and bright areas represents the attractive and repulsive interactions respectively. Using this the domain size of the Fe_3O_4thin film can be obtained. Here the domain size found to be 300nm. Another noticeable fact is that all the features on this film remains unchanged during the Verway transition. This indicates that all the domains remains pinned through the Verway transition. A significant change in contrast in entire film was observed during the Verway transition. A high contrast can be seen below the Verway transition. The MFM contrast is directly proportional to the field gradient in z direction. Increasing contrast suggests the increase in field gradient in z direction. This indicates the rotation of magnetization slightly out of plane below the Verway transition.

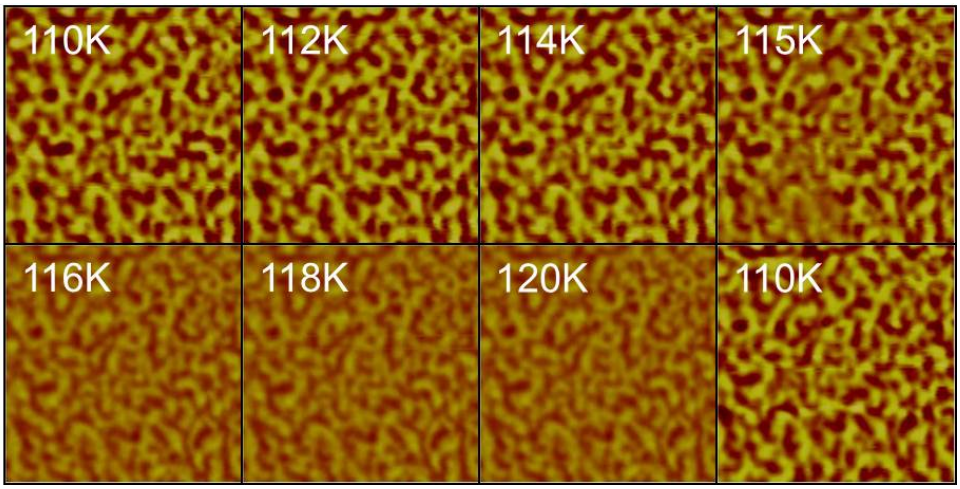

Figure 3.19: MFM images of Fe_3O_4thin film from 110K to 120K

Figure (3.19) shows the MFM images that were taken at fine temperature steps. The figure at 116K shows low contrast compared to the figure at 114K. The figure taken at 115K shows both regions with high and low contrast. This indicates that those areas in the film undergoes phase transition at 115K. From these figures we can conclude that the transition occurs locally within narrow temperature window bound above 2K. But, according to the magnetization data the transition take place across

a broad temperature range. This discrepancy is basically due to the measurement techniques. In SQUID the magnetization averages over the full area of the sample, while MFM is limited to a micron size field of view. Therefore using MFM, the exact transition point can be identified.

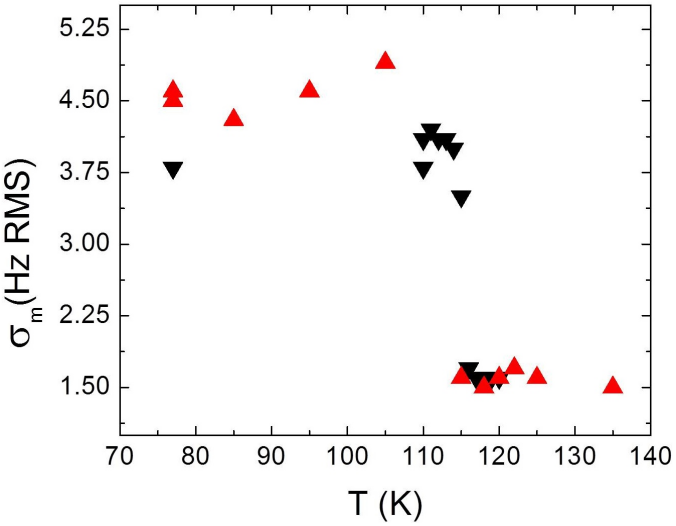

Figure 3.20: RMS values from MFM images with 10K steps (red, up-triangles) and 1K steps (black, down-triangles)

The tilting of magnetization out of plane below the Verway temperature can be also verified by frequency shift data. Frequency shift is proportional to the second derivative of the sample stray field in the direction parallel to the surface normal. Figure (3.20) shows a increment in frequency shift below the Verway transition. This suggests the tilt in magnetization below T_v. The angle of total magnetization with respect to the surface normal was also calculated using three orthogonal magnetization measurements.

$$M_{total} = M_{100}^2 + M_{010}^2 + M_{001}^2$$
$$\theta_{total} = cos^{-1}(M_{001}/M_{total})$$

Figure (3.21) shows the change in total magnetization and it's angle with respect to the surface normal. Here the rotation of angle is clearly visible. The angle of the total magnetization decreases by 6 °indicating the tilting of magnetization out of the

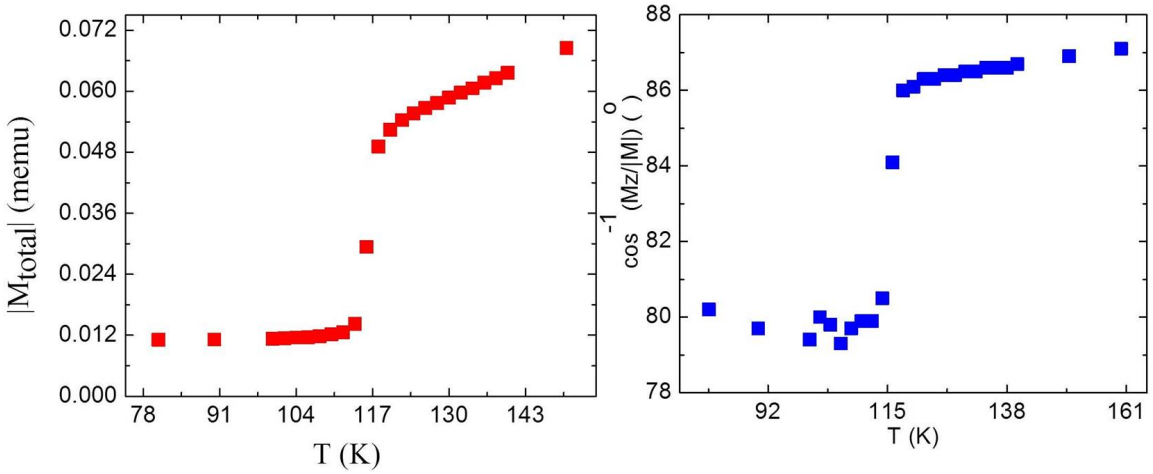

Figure 3.21: Change in Total magnetization with the temperature

plane at the Verway transition. This is the main reason behind the change in contrast in MFM images below the Verway transition.

3.6 Chapter Summary

We have demonstrated that ultra thin TM buffer layers can significantly impact the structural, transport, and magnetic properties of magnetite thin films. The fact is that the magnetite layers were grown simultaneously on all five substrates, allowing us to make conclusions based solely on the buffer layer material. Surprisingly, the Mo, Cr, and unbuffered samples all showed similar behavior, despite the fact that the Cr buffered magnetite appears polycrystalline. In contrast, the Nb and Fe buffered samples showed strong (001) texture but have anomalous magnetic properties. Noting that Nb and Fe are more reactive than Mo and Cr, a potential origin of these observations is that Nb and Fe may have reduced the magnetite, creating a stoichiometrically inhomogeneous material near the lower interface. Magnetization properties revealed the rotation of total magnetization below the Verwey transition. MFM measurements confirmed the rotation of magnetization slightly out of the plane below the Verwey transition.

4 Spin Valves using Magnetite

Reactively sputtered Fe_3O_4 on MgO(100) substrates were used to fabricate spin valve structures. Mainly two different types of spin valves were fabricated. Those were Fe_3O_4/Cr/$Ni_{80}Fe_{20}$(Py spin valves and Fe_3O_4/Cr/Fe_3O_4 spin valves. Here the main principle behind these type of spin valves is that they generate the spin polarized current through reflection rather than direct spin injection [43] [44]. Also the effect of uni-axial anisotropy induced by field growth was studied on Py, Fe_3O_4 single layers and Py/Cr/Fe_3O_4 spin valve structures.

4.1 Fe_3O_4/Cr/Py Spin Valves

Fe_3O_4 was used with Py and Cr spacer layer in the spin valve. Fe_3O_4 was directly deposited on the the MgO(100) substrate by reactive sputtering. The magnetite deposition rate was 0.26Å/s. Then it was followed by direct deposition of Cr and Py onto it. Both Py and Cr were deposited at room temperature and 3mTorr pressure using DC magnetron sputtering. The deposition rates for Py and Cr at 100W DC power were 0.6 Å/s and 0.3 Å/s respectively. To obtain good interface the sample was kept in vacuum during deposition; this helps to prevent oxidation from taking place at the interfaces. The thickness of Fe_3O_4 and Py was kept constant at 300 Å. To study the thickness dependence of the spacer layer the Cr layer thickness was varied from 41 Åto 107 Å. This was done by growing a Cr wedge during the deposition.

To grow a wedge of any material the rotation of the sample holder should be stopped during the deposition so that the area closest to the sputtering gun gets more material flux and thus grows thicker than the far end of the substrate holder(fig. 4.1a).

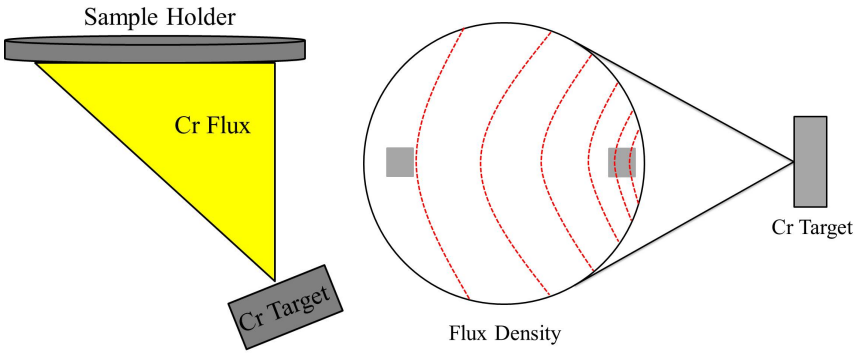

(a) Side View (b) Bottom View

Figure 4.1: Deposition flux density map

When doing this as shown in figure 4.1b the substrates place along the diameter of the substrate holder and that line align with the target material. So the closer substrates get more material flux than substrates on the far side.

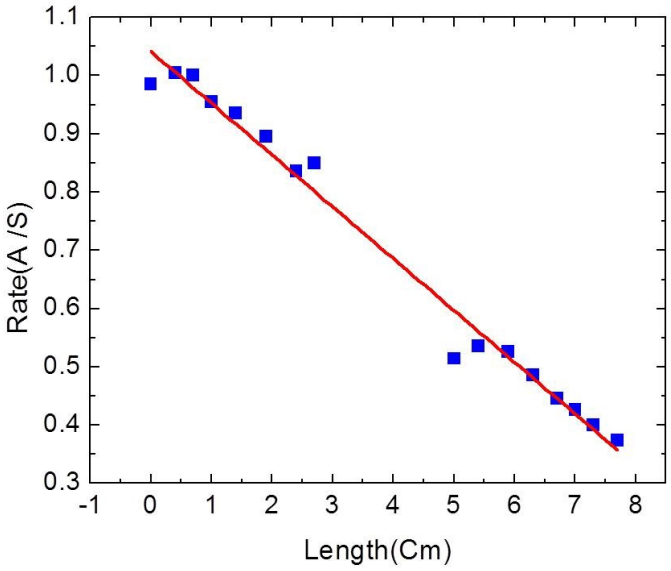

Figure 4.2: Deposition rate of as a function of the position of the sample.

Figure 4.2 shows the variation of deposition rate as a function of the sample position. A factor of 3 difference in thickness was observed by this method. This allows us to grow all the spin valve structures in one deposition run, so the Fe_3O_4 and Py is the same for all the samples and any difference in MR should be due to the Cr

thickness.

4.1.1 Measuring Magneto-resistance

Current in-plane magneto-resistance measurements were carried out in these samples. A solenoid which can output 1500 Oe field with 30A current was used to apply the magnetic field. It was connected to a 30 A power source which is controlled through a Labview interface. This allowed us to sweep the magnetic field from +1500 G to -1500 G in desired step sizes. To measure the resistance change, a Wheatstone bridge circuit was used with a lock in amplifier.

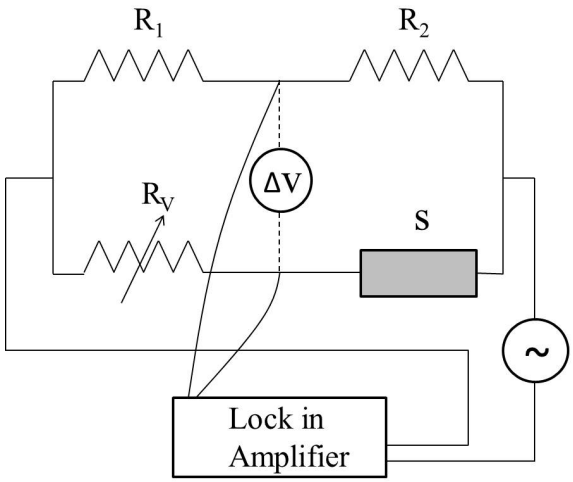

Figure 4.3: Experimental set up for MR measurements

The sample was attached to the probe using double sided tape, taking special care to make sure that the sample sits parallel to the surface of the probe. Air bubbles trapped in side the tape can make the sample to become tilted, which could lead to errors in measurement. To measure the MR, Cu wires were connected to the sample using Indium. Here a small amount of Indium was put on top of the sample and placed the wire on top of it and squished it, so that the wire and Indium stick to the sample. The final contact is typically about 1 mm in diameter. If the MR is directly measured using a multimeter it's necessary to do real or pseudo four probe measurement to

remove the effects of the contacts. In pseudo four point measurement both current and voltage leads connect to a single Indium contact as shown in figure 4.4b. This does not fully remove the effect of contact resistance on the sample resistance, but is reasonable to do and easier if the resistance of thin film is 100 Ω or more.

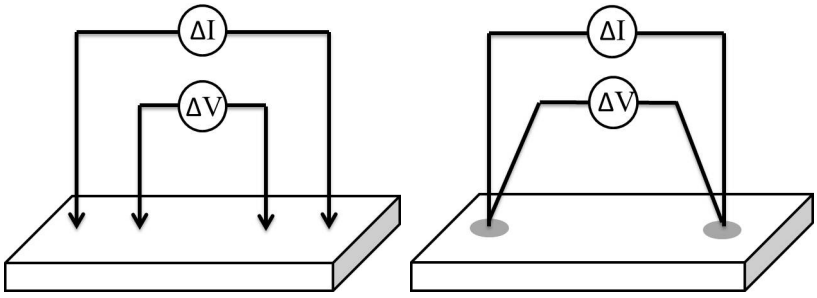

(a) Four point method (b) Pseudo four point method

Figure 4.4: Four point method of resistance measurement

Since we only measure the voltage change, when using the bridge circuit, there is no need to use the four point method. In this method, the sample (S) was connected to the Wheatstone bridge circuit as shown in the figure (4.3) with a variable resistor R_v. A sine signal of 1 kHz with 0.5 V amplitude was applied to the bridge using a lock-in amplifier. The resultant voltage was measured using the same lock-in amplifier. In preparing to measure the voltage, the bridge was balanced by varying the resistance of R_v and $R_1 : R_2$. Then the resistance of the sample R_s was estimated using the equation

$$R_s = R_v \frac{R_1}{R_2}$$

After that the sample was temporarily removed from the circuit and replaced with a decade resister box in order to calibrate the voltage to resistance conversion. The circuit was calibrated by measuring the resultant voltage difference (ΔV) by changing the resistance of the decade resistor. This ΔV *vs* ΔR data was plotted to get a calibration curve. Using this plot it's possible calculate the resistance change of the

sample by measuring the change in voltage (ΔV). After this step, again the sample was connected to the bridge circuit to carry out magneto resistance measurements. This procedure was carried out before each and every measurement without any external magnetic field. Room temperature GMR measurements were carried out for all the Fe_3O_4/Cr/Py spin valves. The magnetic field was applied parallel to the current flowing direction.

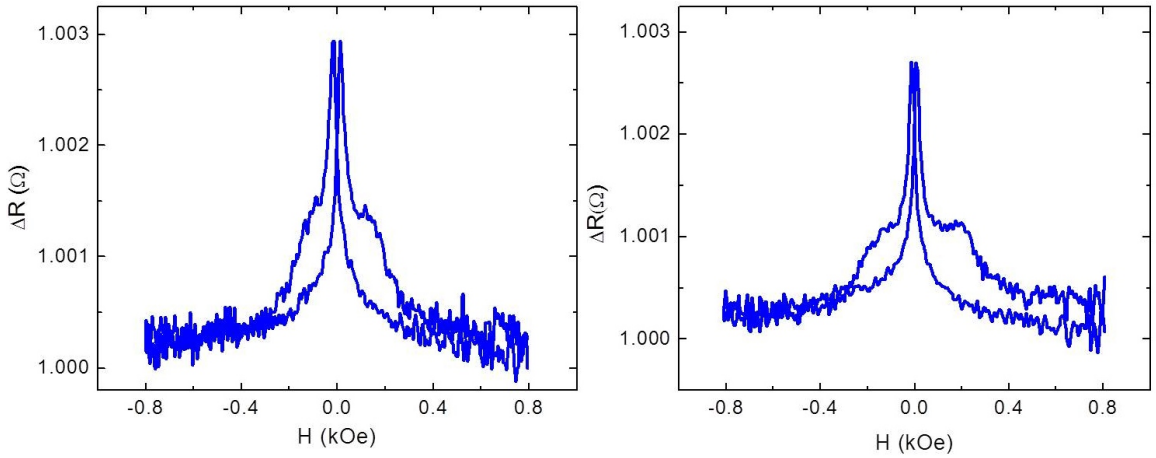

Figure 4.5: Fe_3O_4/Cr/Py spin valves with different spacer layer thicknesses. (a) Cr - 41 Å (b) Cr - 107 Å

A clear GMR signal was observed on all the samples. When the current is applied to the spin valve, due to the higher resistance of Fe_3O_4 layer most of the current flows in Cr and Py layers. The current flow close to the Fe_3O_4/Cr interface in Cr layer gets reflected off the Fe_3O_4 interface and may become spin polarized. Then these electrons scatter from the Cr/Py interface and leads to GMR. Figures(4.5) show the MR data for spin valves with 47 Å and 107 Å thick Cr spacer layers. In addition to a small GMR signal, we also observed an anisotropic magneto resistance(AMR) signal from the Py. This is mainly due to the reversal of the magnetization of Py with the applied magnetic field. This is an unavoidable issue because of the higher resistance of the Fe_3O_4 most of the current flow through the Cr and Py layers. The current flow through the Py layer generates these AMR peaks due to the bulk scattering. Nevertheless the intensity of the peak can be reduced by applying a magnetic field

during the deposition as will describe later in this chapter. Even with the higher AMR peak the GMR signal is still observable.

In all the samples the parallel and anti-parallel states can be identified clearly. The parallel state is saturated with a low resistance and the anti-parallel state is the shoulder with high resistance. This indicates the switching of two FM layers separately with the applied field. Py switches magnetization around ±10 Oe and Fe_3O_4 switches magnetization around ±200 Oe. The GMR ratio was calculated by subtracting the resistance of saturated parallel state by resistance of the anti-parallel shoulder normalized by the resistance of the saturated parallel state.

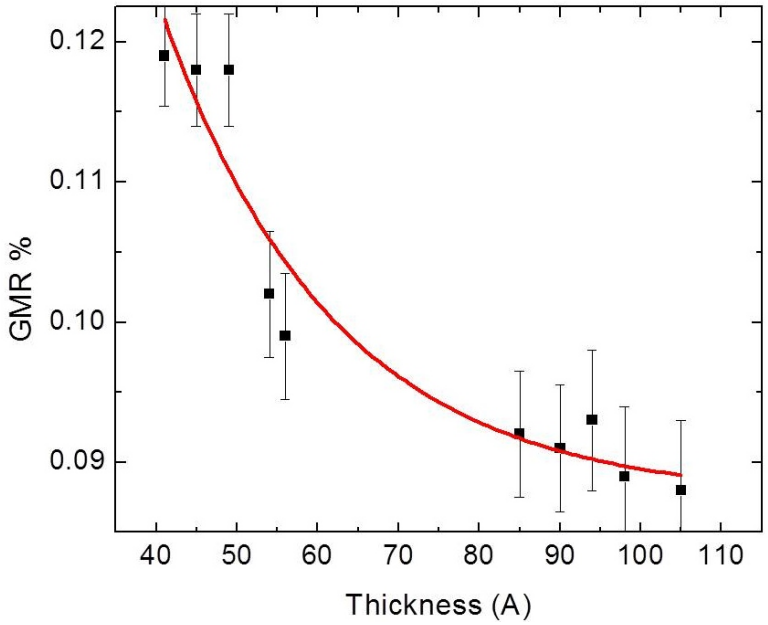

Figure 4.6: GMR Vs Cr thickness of Fe_3O_4/Cr/Py. No samples were made with thickness range between 60 Å to 80 Å due to the shadowing of the sample holder.

Though small, the GMR showed an exponential decay with increasing Cr film thickness. By fitting to an exponential curve the decay constant was found to be 19Å at room temperature. This is smaller than the reported spin diffusion length of Cr at 4K [9]. We didn't observe any oscillatory behaviour in GMR due to the larger Cr film thickness. Another possible explanation for the lack of oscillatory coupling is,

the resultant GMR on these samples can be from bulk scattering rather than interface scattering.

4.2 $Fe_3O_4/Cr/Fe_3O_4$ Spin Valves

In these spin valves different Fe_3O_4 film thicknesses were used to get different coercive fields. First a 500 Å of Fe_3O_4 was directly deposited onto the MgO(100) substrates. It was followed by a Cr wedge with thicknesses from 57 Å to 151 Å. Then 1000 Å of Fe_3O_4 was deposited as the top layer. Similar to the previous experiment, current in plane MR was measured with field parallel to the current flowing direction. In this case the switching of magnetization of Fe_3O_4 was observed at different applied fields, indicating the different coercive fields from the different Fe_3O_4 thicknesses. Generally the thicker film gives the higher coercivity.

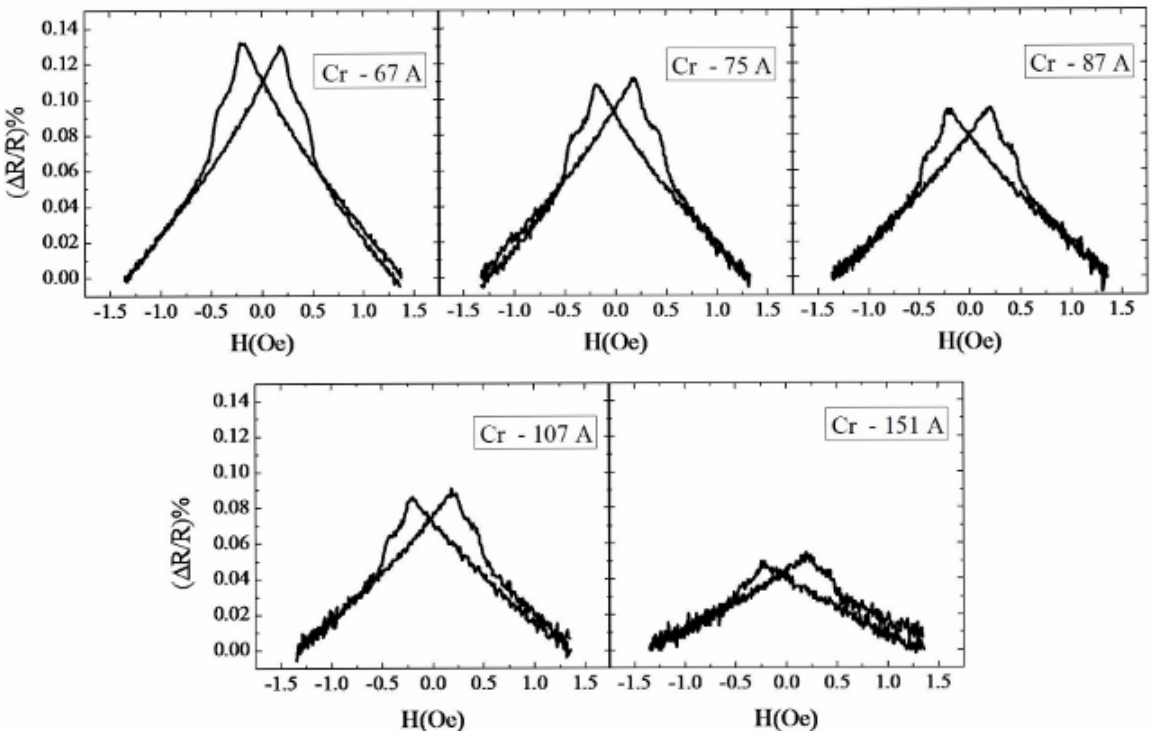

Figure 4.7: Variation of GMR with Cr spacer layer thickness ion $Fe_3O_4/Cr/Fe_3O_4$

Figure(4.7) shows the variation of GMR in $Fe_3O_4/Cr/Fe_3O_4$ spin valve with the Cr layer thickness. The main difference in these spin valves compared to $Fe_3O_4/Cr/Py$ spin valves is that $Fe_3O_4/Cr/Fe_3O_4$ spin valves do not saturate at higher fields. The samples show butterfly like AMR behavior, which is intrinsic to Fe_3O_4 [45] and the different switching fields can be clearly identified. In calculating the GMR, the shift of the signal relative to the AMR signal was considered (fig. 4.8).

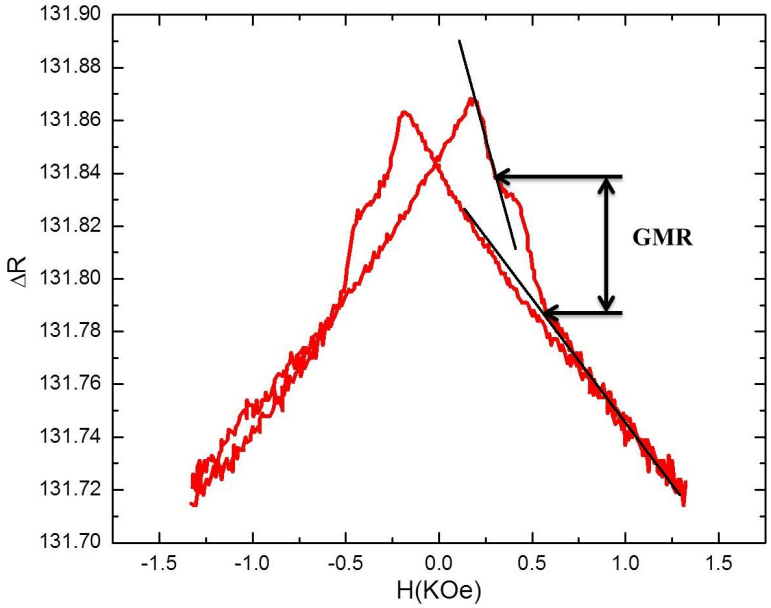

Figure 4.8: Calculation the GMR on $Fe_3O_4/Cr/Fe_3O_4$ spin valve

Similar to the previous experiment here also the GMR was measured as a function of Cr spacer layer thickness. The GMR showed an exponential decay with the increasing Cr spacer layer thickness. The decay constant was determined to be 33Å at room temperature.

In both types of spin valves the observed GMR values are quite small relative to the all metal spin valve structures, but they are well within the reported magnetite/NM/FM spin valve structures. This can be due to combination of effects. Oxidation of Cr layer at the Cr/Fe_3O_4 interface can be a major problem. Since the Cr was deposited after the reactive sputtering of magnetite it's possible the residual

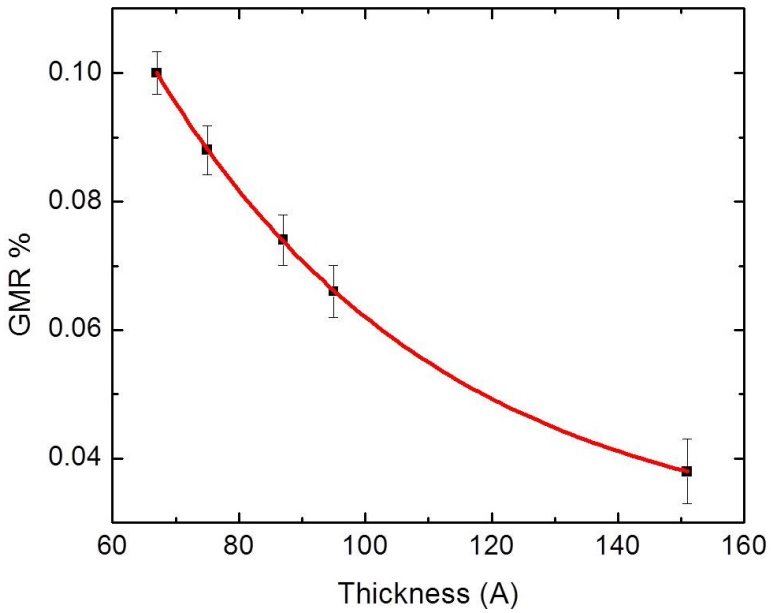

Figure 4.9: GMR Vs Cr thickness on Fe_3O_4/Cr/Fe_3O_4 spin valve

oxygen in the chamber might have oxidized the Cr interface. This oxide layer might act as a barrier to the spin dependent reflection which is necessary for larger GMR. Also, impurities present in the Cr spacer layer can reduce the spin diffusion length of the Cr, which will lead to lower GMR. This also might be the reason behind the different decay constants in Fe_3O_4/Cr/Py and Fe_3O_4/Cr/Fe_3O_4 spin valves. This is possible if the Cr spacer layer in the two spin valves have different impurity levels. Also the GMR in Fe_3O_4/Cr/Fe_3O_4 spin valves are lower compared to Fe_3O_4/Cr/Py spin valves. This is expected because in Fe_3O_4/Cr/Fe_3O_4 spin valves spin polarization is entirely occur through spin dependent reflection. The efficiency of this process might be less compared to the Py/Cr interface due to above mentioned reasons and leads to lower GMR. Also in Fe_3O_4/Cr/Py spin valves the resistivity mismatch between magnetite and metals might cause shunting of the current, giving low current density close to the Fe_3O_4 interface and reduced the opportunity for spin dependent reflection. In addition the higher spacer layer thickness is also a major reason for the lower GMR values. Here the spacer layer thickness values are above the spin diffusion

length of Cr. Another possibility is that, since the film thicknesses are relatively high, what we might have seen here is a significant contribution to the GMR from the bulk scattering rather than the interface scattering. Previous studies have shown that low GMR values arise from bulk scattering in CIP geometry. Also in previous chapter, the Cr buffered Fe_3O_4 layer showed some extra Fe_3O_4 peaks in X-ray diffraction study suggesting the polycrystalline nature of Fe_3O_4. Therefore the surface in contact with the Cr may have not be ideal and may have lead to lower spin polarization.

4.3 Influence of Growth Field on Py, Fe_3O_4 and Py/Cr/Fe_3O_4 Spin valves

As described in the last section, Fe_3O_4/Cr/Py spin valves have a significantly large signal due to the AMR of Py. We tried to minimize the intensity of the AMR peak by introducing an uni-axial anisotropy to the Py by growing it inside a magnetic field. We also did the same experiment for Fe_3O_4 and Py/Cr/Fe_3O_4 spin valve structures. A similar experiment could be pursued in the future by lithographically introducing the uni-axial anisotropy. This is complicated by the high temperature processing of Fe_3O_4, as well as our desire to keep the interfaces as clean as possible; post deposition milling is possible, but can potentially damage the magnetite. In contrast, field deposition is straight forward and avoid these possible major complications.

4.3.1 Introducing Uni-axial Anisotropy

The anisotropic magneto-resistance of a ferromagnetic sample is defined by,

$$R(\theta) = R_0 + \Delta R_0 \cos^2(\theta),$$

where R_0 is the average resistance of the sample and θ is the angle between the current direction and the magnetization direction of the sample. Accordingly

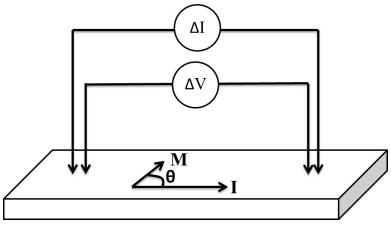

Figure 4.10: AMR measurement

When, $\theta = 0°$: $R(\theta) = R_0 + \Delta R_0$,gives a maximum.

When $\theta = 90°$: $R(\theta) = R_0$

That is when the magnetization of the sample is parallel to the current flowing direction, the resistance of the FM should reach a maximum and when the magnetization is perpendicular to the current flowing direction the resistance should come down to the average value. Figure(4.11) shows a cartoon of the variation of the AMR signal with an external magnetic field. The spin diagrams at the top and the bottom show the rotation of spins with increasing and decreasing applied fields.

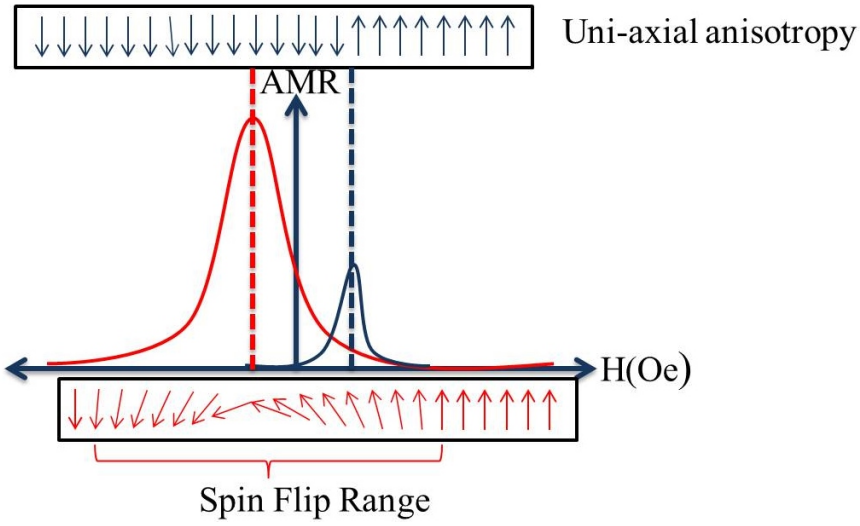

Figure 4.11: Spin rotation during AMR measurement. Red curve represents the normal magnetization reversal in a ferromagnet; blue curve represents the magnetization reversal in a sample with uni-axial anisotropy.

As shown in figure (4.11) the rotation of spin takes place in a wide field range and leads to a broad intense peak rather than a short sharp peak. If an uni-axial

anisotropy induced into the FM then the spin rotation will take place in a smaller field range. This should also cut down the intensity of the AMR peak significantly.

Uni-axial anisotropy can be induced into a film with couple of methods. One is lithographically patterning the film in to a long skinny wire. Due to the shape anisotropy, the magnetization of the sample will align parallel to the length of the sample. When the applied field changes, the magnetization directly jumps from parallel to the anti-parallel position skipping the perpendicular orientation, which is prohibited due to the shape anisotropy. Another method to obtain the uni-axial anisotropy is to apply a magnetic field during the growth process. This aligns the magnetization of all the atoms along the field direction during the growth leading to an uni-axial anisotropy. In this experiment we used the growth field method.

A 200 Oe field was applied to Py, Fe_3O_4 and Py/Cr/Fe_3O_4 spin valves during the growth process. Since Fe_3O_4 was reactively deposited at high temperatures a special sample holder was designed(fig. 4.12).

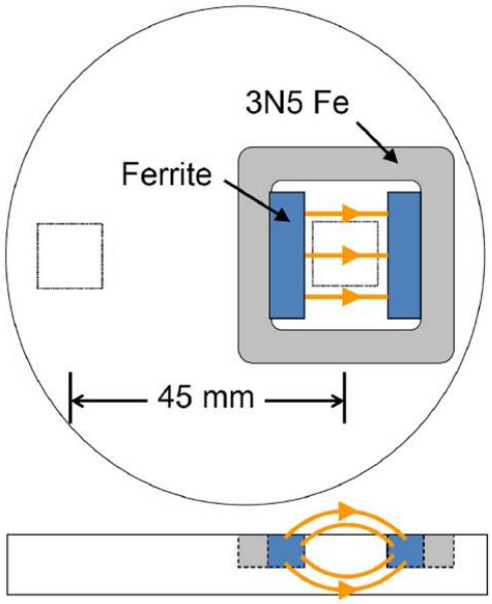

Figure 4.12: Sample holder designed for apply a field during the growth process

Most of the rare earth magnets lose their magnetization at modest temperatures (100°C). Therefore we used commercially available ferrite magnets, which can be used

up to 450°C. Before they were used in the experiment the magnets were baked in the sputtering chamber at 300°C for 2 hours and took out to measure the magnetic fields. Magnetic field values didn't show any difference before and after the baking. In the sample holder two ferrite magnets were placed on inner perimeter of a Fe yoke, which is machined from 99.99% purity Fe (an old sputtering target). Then this set up was placed in a square shaped trench that was machined in an aluminum plate. The sample can be placed in between the magnets as shown in the figure(4.12). Since the Fe yoke and the magnets do not come out of the plane of the Al plate there is no shadowing during the deposition. Also this sample holder allows us to make two samples simultaneously, one in a field and other without a field. As shown in the figure (4.12) the sample in the left grows under nearly zero field. Stray fields from the Fe yoke and the magnets are not in the measurable magnitudes using a Gauss meter.

Using this sample holder three sets of samples were deposited. Two 100Å Py films were deposited by DC sputtering at room temperature and 3 mTorr pressure onto a Si(100) substrate with a native oxide layer, one inside the magnetic field and other without the magnetic field. Similarly two 500Å Fe_3O_4 samples were deposited onto MgO(100) substrates at 300° C and 10 mTorr pressure by reactive sputtering. Then two Py/Cr/Fe_3O_4 spin valves were also deposited on to MgO(100) substrates one inside the magnetic field and other without the magnetic field.

4.3.2 Effect of Growth field on Py and Fe_3O_4 thin films

Current in plane MR measurements were carried out at room temperature for all the samples. The resistance was measured using the previously defined pseudo four point measurement protocol. The sample is oriented such that the current path is parallel to the growth field and the applied field for MR is perpendicular to the growth field.

The Py sample grown without a field exhibits a normal AMR behavior with two

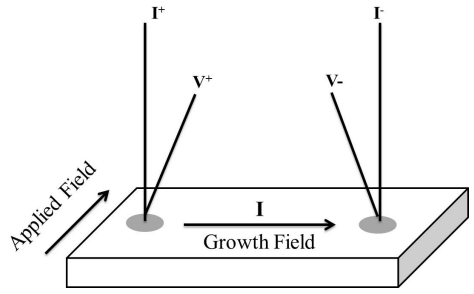

Figure 4.13: CIP AMR measurement set up

broader peaks at the coercive fields (150°C). The sample grown in the magnetic field shows a reduction in coercivity and the amplitude of AMR signal. This is a signature of uniaxial anisotropy. Now the magnetization reversal occurs in reduced field range, because the magnetization is constrained by the anisotropy to stay along the growth field direction except near the reversal region. At the reversal field rather than rotating slowly with the magnetic field, the magnetization rotates sharply by 180°.

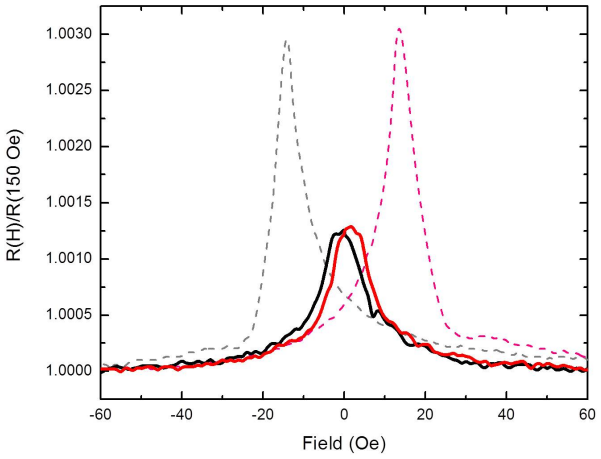

Figure 4.14: AMR of Py film with and without growth field (Dotted line represent the sample grow without a field)

This leads to sharp AMR peak with reduced amplitude. The breadth of the peak implies imperfect uni-axial anisotropy. This could be due to the large area of the

substrate allowing non-uniform current flow. Also a gradient in the deposition field can cause the imperfect uni-axial anisotropy.

The Fe_3O_4 sample also showed similar behavior with reduced coercivity and AMR peak amplitude. In magnetite the signal does not saturate at low fields due to anti phase boundaries [46]. Therefore, the breadth of the AMR peak cannot be impacted as easily as in Py. The growth field does not change the structural or transport properties of Fe_3O_4 and no changes were observed in resistivity and Verwey transition temperature.

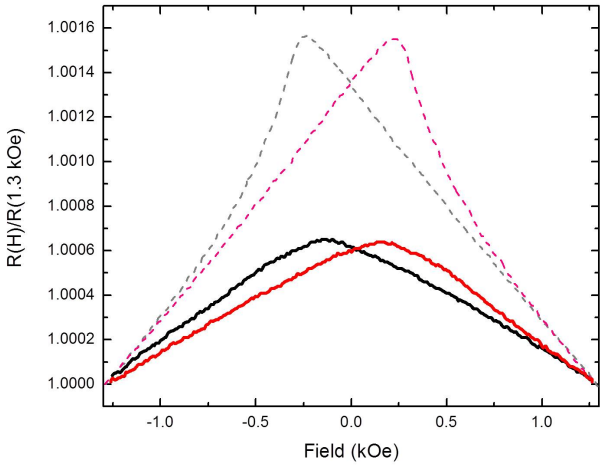

Figure 4.15: AMR of Fe_3O_4 film with and without growth field (Dotted line represent the sample grow without a field)

4.3.3 Effect of growth field on Py/Cr/Fe_3O_4 spin valves

Current in plane GMR was measured on the spin valve at room temperature. As shown in figure(4.16), the spin valve with the growth induced anisotropy has formed well defined parallel and anti parallel states compared to the sample grown without a field. Because of the uni-axial anisotropy being enhanced, a clear shoulder has developed at the anti parallel state. The parallel state also shows much more saturated behaviour, which means the $\vec{M}$ is no longer rotating in the plane. This makes defining

GMR much easier. Despite these improvements, the Py AMR peak is still remains above the GMR signal.

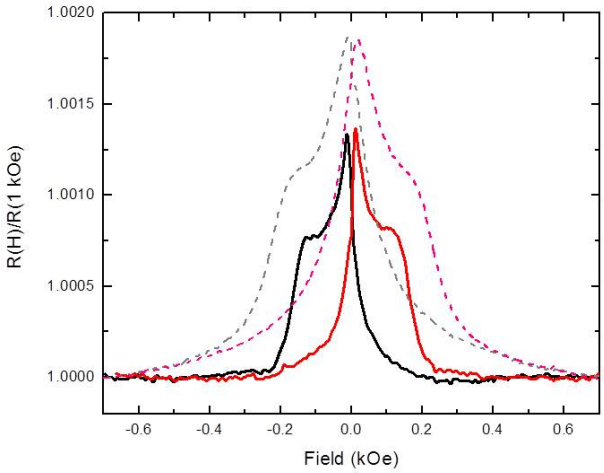

Figure 4.16: GMR of Py/Cr/Fe_3O_4 spin valve with and without growth field (Dotted line represent the sample grow without a field)

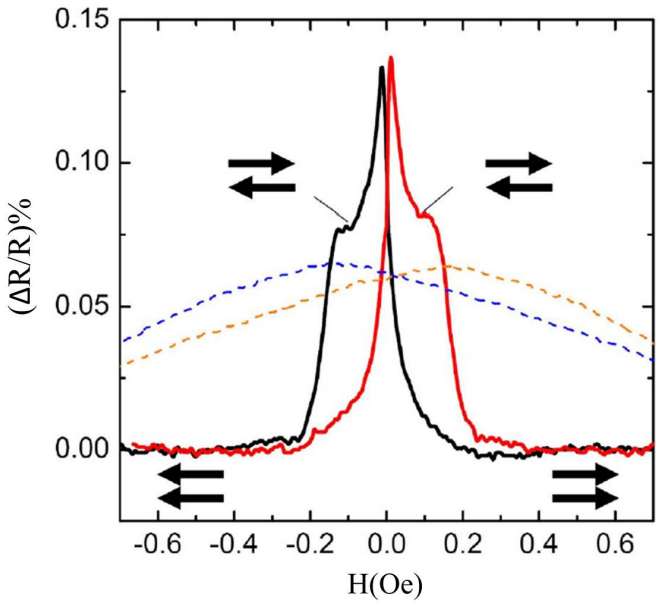

Figure 4.17: GMR of Py/Cr/Fe_3O_4 spin valve with Fe_3O_4 AMR signal (Dotted line represents the Fe_3O_4 AMR signal)

Figure(4.17) shows the GMR signal with the Fe_3O_4 AMR signal. The transition

from the parallel state to anti-parallel state is sharper than the AMR of single layer of Fe_3O_4 film. Even though the Fe_3O_4 doesn't saturate, the spin valve showed saturation after magnetization reversal of Fe_3O_4. The transition occurs at the same coercive field as single layer magnetite. This indicates that the current flow in Fe_3O_4 layer is insignificant and most of the current flow through the Py and Cr layers due to the higher resistivity of Fe_3O_4. This also underscores the presence of GMR not only the AMR. The GMR was defined as the difference between the saturated parallel state and the anti-parallel shoulder.

If the origin of GMR is from current become polarized by reflection off the Fe_3O_4 interface and interact with the Cr/Py interface then the efficiency of the process is low. Therefore the observed GMR values are also relatively low.

As a conclusion the growth field induced an uniaxial anisotropy on both Py and Fe_3O_4 thin films by reducing the coercivity and the AMR peak intensity. In spin valve the growth field produced a well defined parallel and anti-parallel states.

Assume that the Julliere's TMR model is applicable to CIP GMR [47]. Tunnelling magneto resistance (TMR)

$$\text{TMR} = \frac{2P_1P_2}{1 - P_1P_2}$$

where, P_1 and P_2 are the spin polarization of two ferromagnetic materials.

$$\text{Assume; } P_1 = P_{Py} = 0.4 \; P_2 = P_{Fe_3O_4}$$

According to our experiments the GMR of Fe_3O_4 spin valve is 0.10%. Therefore;

$$TMR \sim GMR = 0.001$$
$$P_2 = \frac{1}{799.6}$$
$$P_2 = 0.13\%$$

But we assumed that the Fe_3O_4 has 100% spin polarization at the Fermi level ($P_2 = 1$). This means that the spins mostly retain their state upon collision with interface. Only

1 out of 799 flips its spin. This value is too small for a spin valve, but reasonable for other applications such as spin torque oscillators.

4.4 Chapter summary

We successfully demonstrated use of Fe_3O_4 in spin valve structures with Py and Cr spacer layers. This indicates that the process of spin polarization by reflection can be use in spin transport devices though it does not appear very efficient. The GMR reduced exponentially with the Cr layer thickness. RKKY oscillations were not observed due to the higher Cr layer thickness. The GMR values were relatively low compared to all metal spin valve structures. This is mainly due to the low efficiently of the spin flipping process. The growth field induced an uniaxial anisotropy to both Py and Fe_3O_4 reducing the intensity and the coercivity of the AMR peaks. Spin valve structures obtained more well defined parallel and anti-parallel states due to the use of growth field.

5 Spin Caloritronics

The relationship between heat and charge currents have been known for centuries. For example this phenomenon has been used, in thermoelectric applications from advanced power generators to simple coolers. The heat current also interacts with the magnetic spins [48], [49], [50], [51]. The study of this interaction between heat and spin is known as the "spin caloritronics". While this is an emerging area, several effects have already been observed: spin dependent Seebeck effect [52], Peltier effect [53], spin Seebeck effect [54], anomalous Nernst effect and planer Nernst effect. The field of spin caloritronics had a resurgence after the supposed discovery of spin Seebeck effect. Because the area is still developing, the quality and correctness of both experiments and theory are still developing [55].

In this section I have mainly focused on our effort to measure Spin Seebeck, anomalous Nernst effect, and planar Nernst effect in thin films as well as measuring spin dependent Seebeck effect of spin valve structures.

5.1 Spin Seebeck Effect

When a temperature gradient is applied to a ferromagnet, a spin current generates due to the thermal non-equilibrium of magnons in the ferromagnet. This spin current produces a spin accumulation at two ends of the ferromagnet and leads to different chemical potentials for spin up and spin down electrons. This chemical potential difference can be changed in to an electric field using Inverse Spin Hall effect (ISHE) by making contact with a paramagnetic material (PM) with relatively large spin Hall angle. The electric field that results from the ISHE is

$$E_y = \frac{\theta_{SH}\rho}{A}(\frac{2e}{\hbar})\vec{J}_s \times \vec{\sigma}$$

where, θ_{SH} the spin hall angle, ρ the electric resistivity of the PM, A the contact area between the FM and the PM, J_s the spin polarized current and $\vec{\sigma}$ the spin polarization direction of the ferromagnet (either parallel or anti-parallel to $\vec{M}$ depending on material). This effect was first observed by Uchida, *et.al* in 2008 [56] on Py thin films. In their experiment a constant temperature gradient and an external magnetic field were applied along the ferromagnetic material deposited on a Al_2O_3 substrate.

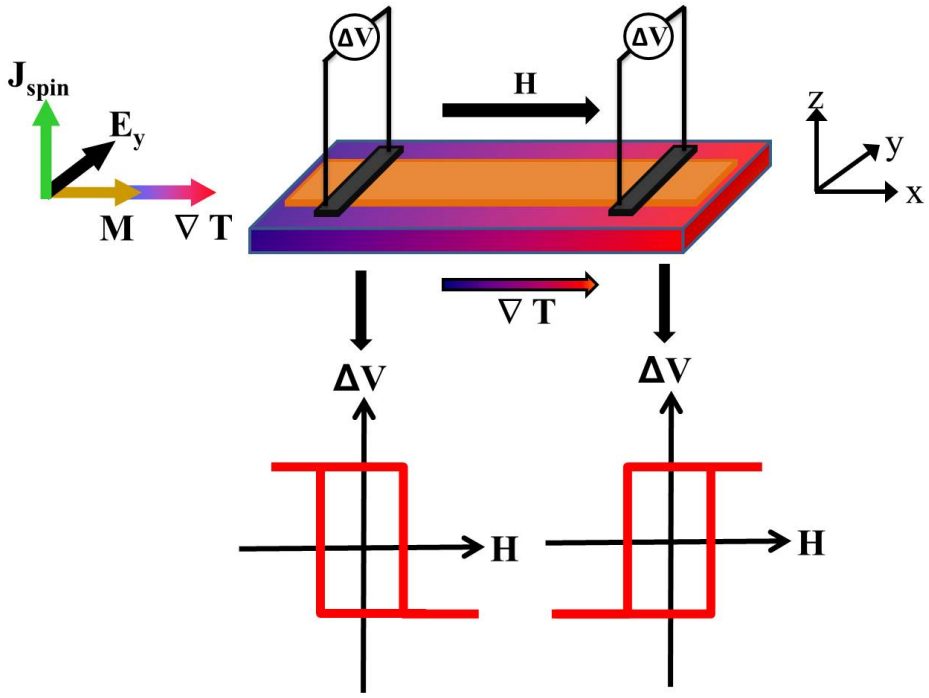

Figure 5.1: Spin Seebeck effect

Then the resultant voltage (E_y) was measured across Pt electrodes deposited onto the Py film. The Pt electrodes were deposited transverse to the length of the ferromagnet. The real spin Seebeck effect should give a hysteretic V-H loop upon sweeping the external magnetic field with opposite signs in each end (hot and cold) as shown in the figure 5.1. First this phenomenon was explained considering the different chemical potentials of spin up ($\mu_\uparrow$) and spin down ($\mu_\downarrow$) electrons [57] [58]. Since spin

up and spin down electrons have different scattering parameters they have different Seebeck coefficients [10]. This is similar to having two materials with different Seebeck coefficients in a single ferromagnet. When a thermal gradient is applied along the ferromagnet, electrons with different Seebeck coefficients move in different conduction channels [59] [60]. This unequal flow of electrons in two channels creates a spin accumulation at the ends of the ferromagnet, with spin up electrons accumulating at the cold end and spin down electrons accumulating at the hot end (fig. 5.2).

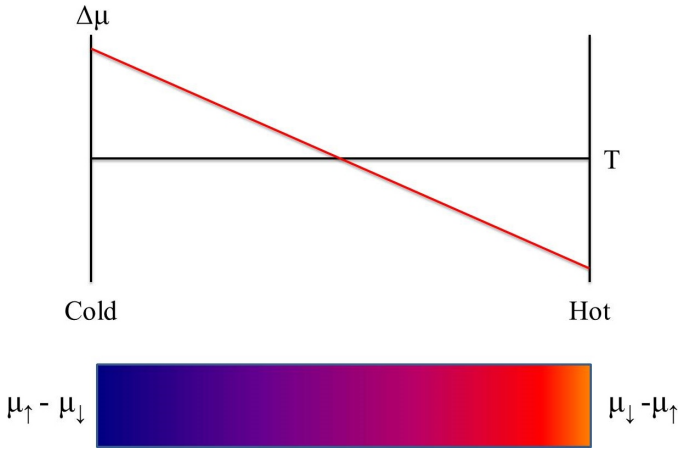

Figure 5.2: Chemical potential difference generated by spin accumulation

This accumulation of spins at the two ends of the ferromagnet generates asymmetric chemical potential difference for spin up and spin down electrons ($\mu_\uparrow - \mu_\downarrow$ and $\mu_\downarrow - \mu_\uparrow$), with opposite signs at two ends. This difference in spin chemical potentials creates a spin current flow along the ferromagnet. To detect the spin accumulation the inverse spin Hall effect was used.

5.1.1 Inverse spin Hall effect

The inverse spin hall effect(ISHE) is a method that can convert spin current into an electromotive force using spin-orbit coupling [61]. This is the reciprocal of the spin Hall effect, in which there is the generation of spin current transverse to the electric current due to different scattering parameters of spin up and spin down electrons.

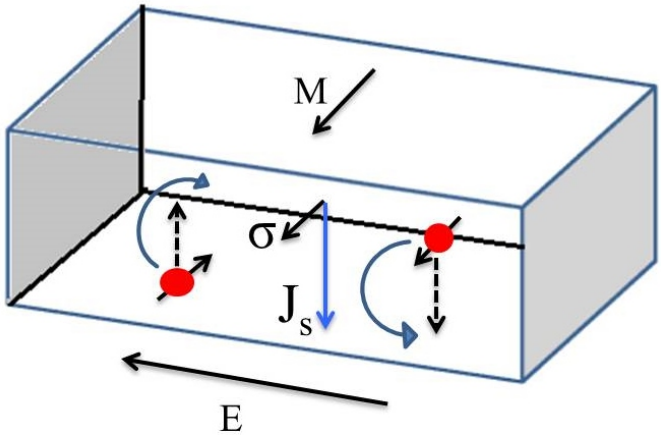

Figure 5.3: Schematic diagram of inverse spin Hall effect

Consider a spin current injected into a paramagnetic material with high spin-orbit coupling. It's possible to treat the spin current as a flow of spin up and spin down electrons in opposite directions. These spin up and spin down electrons flow in different directions undergo spin-orbit coupling and move orthogonal to both J_S and $\vec{\sigma}$. This creates an electron accumulation at one surface of the PM generating an electric field orthogonal to the magnetization [62]. The resultant electromotive force is $E = D.\vec{J_s} \times \vec{\sigma_j}$. Where, D= $\frac{\theta_{SH}\rho}{A}(\frac{2e}{\hbar})$, is the efficiency of the process. D is directly proportional to the spin hall angle of the PM. Therefore, to get a higher efficiency from the ISHE, materials with high spin hall angles should be used. Pt, Pd, Au are some materials with high spin hall angles [63].

In spin Seebeck effect the ISHE is used to convert the spin current produced by the temperature gradient in to an electromotive force. This is done by depositing a metal with high spin-orbit coupling on top of the ferromagnetic material [56].

The spin current flow from the ferromagnet to the cross electrode scatters due to the ISHE and produces an electromotive force across the electrode. The direction of the electro motive force is orthogonal to both spin current and the magnetization. Due to the opposite accumulation of spin up and spin down electrons in opposite ends of the ferromagnet the resultant electromotive force also has the opposite signs.

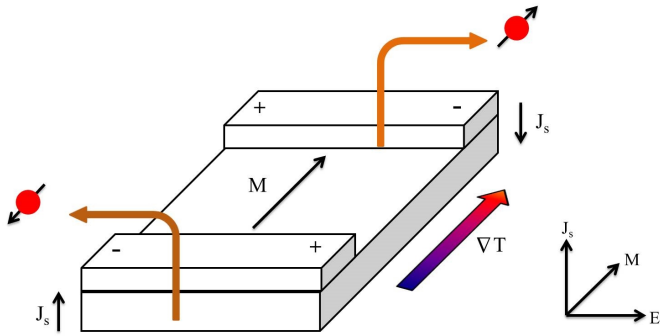

Figure 5.4: Schematic diagram showing the origin of spin Seebeck effect in thin films

When the applied field is swept between positive and negative fields, a hysteresis loop shaped signal with opposite signs can be obtained at both ends, but they are inverted.

The above explanation of SSE opened up lots of questions regarding spin transport. Especially transport of spin polarization well beyond the spin diffusion lengths of materials . Usually the spin diffusion length of ferromagnetic materials limited to nanometre scale and up to μm in Al/Cu at low temperatures. But if the above theory is correct, in ferromagnetic materials the electrons should be able to maintain their spin polarization for centimetres. This contradicts the established understanding of spin transport. In 2010 Jaworski *et al* reported the observation of SSE on a discontinuous ferromagnetic layer (i.e. they cut the FM in half, but still observed the signal) [64]. With this observation the above theory has proven to be incorrect. So the spin accumulation does not occur though the spin current flowing through the ferromagnetic layer.

Later Jaworski *et.al* explained the spin distribution using phonon-magnon drag through the substrate [65]. Here non-equilibrium phonons generated from the temperature gradient move the magnons away for their equilibrium position through phonon-magnon interactions. Since phonons can pass through any substrate and especially well in single crystals (used in most experiments) this phonon mediated transport can drag the magnons through the substrates without a continuous ferromagnetic

layer [66]. This explained the observation of SSE on discontinuous ferromagnetic layers. This remains as the most accepted explanation for the spin Spin Seebeck effect.

Similar to the theory of the SSE, experimental data also opened up a lot of question. Recent studies have shown that improper sample mounting techniques can lead to inhomogeneous temperature gradients in the film leading to other phenomenon similar to SSE. One of those effects is the Anomalous Nernst effect (ANE), which originates from out of plane temperature gradients. In this chapter first we describe measuring ANE in thin films and then the methods to minimize the effect.

5.2 Anomalous Nernst effect in Py and Co thin films

Anomalous Nernst effect (ANE) is another phenomenon relating temperature gradients (i.e. heat flow) and ferromagnetic materials. ANE origins from the out of plane ∇T interacting with the in-plane magnetization. The ANE voltage (E_y) is given by

$$\nabla E_y = -\alpha m_x \times \nabla T_z$$

Where α is the anomalous Nernst coefficient, m_x is the in-plane magnetization and the ∇T_z is the out of plane temperature gradient.

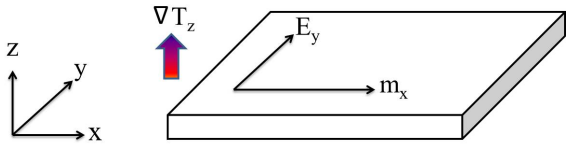

Figure 5.5: ANE voltage due to out of plane ∇T and in-plane magnetization.

Here the magnetization and the resultant ANE voltage are both in the xy plane and the temperature gradient normal to the xy plane. Recent studies have shown that the out of plane ∇T can be present in a substrate due to an in-plane applied ΔT [67]. This can lead to major confusion in spin Seebeck effect measurements, because both

have the same field dependence and angular dependence. it is essentially impossible to distinguish the two effects. In this study we are showing how the spin Seebeck effect measurements can be affected by the ANE signal and ways that can be used to minimize the parasitic ANE.

When a substrate is placed on two thermal baths (one hot and other cold), the heat is transferred into the substrate from the under side, as shown in fig. 5.6. This creates an unintended temperature gradient component parallel to the surface normal, especially "close" to the thermal baths. In addition to this at the sample the heat is dissipated to the environment by either radiation or conduction, creating a temperature difference across the thickness of the thin film. Even though the magnitude of this difference is small, the small film thickness (10 - 20 nm) leads to high temperature gradient (∇T) parallel to the surface normal. This ∇T_z can lead to larger ANE signals in thin films (e.g. 1 mK across 10 nm, ∇T= $\frac{10^{-3}\ K}{10^{-8}\ m} = 10^5\ K/m$)).

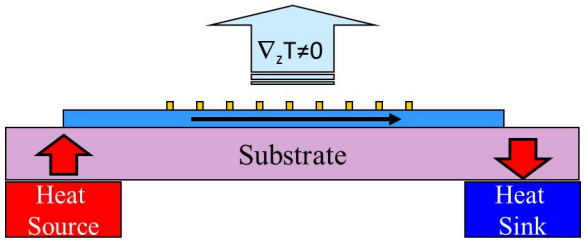

Figure 5.6: Heat dissipated in to air creating a temperature gradient parallel to the surface normal

Therefore it is important to take care in sample mounting and affecting contacts.

5.2.1 Sample preparation

In these types of experiments the interface between the ferromagnet and the other material plays an important role. Therefore having a clean interface is a must for these experiments. In our case we used an *in situ* mask exchanging system during the growth process. It allowed us to use different masks for different depositions

keeping the sample inside a vacuum, which prevents any kind of contamination of the interfaces reaction with atmosphere. Figure 5.7 shows the main steps of the deposition process using a *in situ* mask exchanging system. All the samples were made using an Ar ion sputtering system. Mainly Si/SiOx and MgO(100) were used as substrates for depositions. All the samples were grown with a ferromagnetic layer deposited through a long mask (18 × 5) mm and cross electrodes deposited transverse to the length of the ferromagnetic layer. Different types of cross electrodes (8 × 0.2) mm including Au, Ta, Cu and Ag were used depending on the experiment.

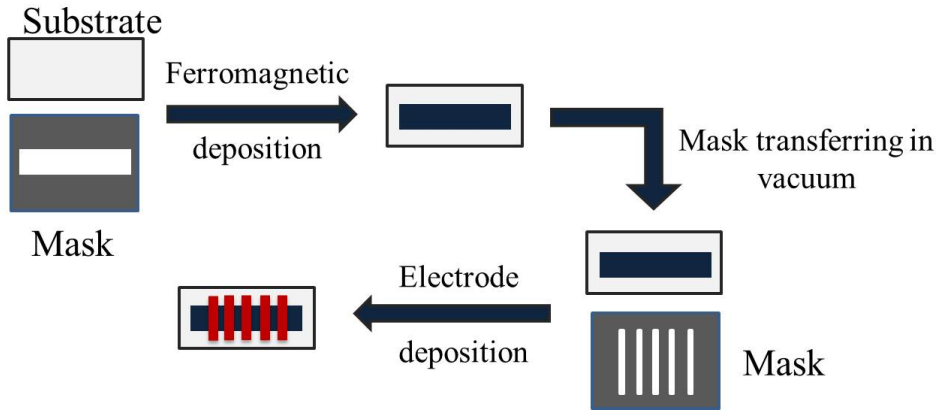

Figure 5.7: Using the *in situ* mask exchanging system for sample preparation

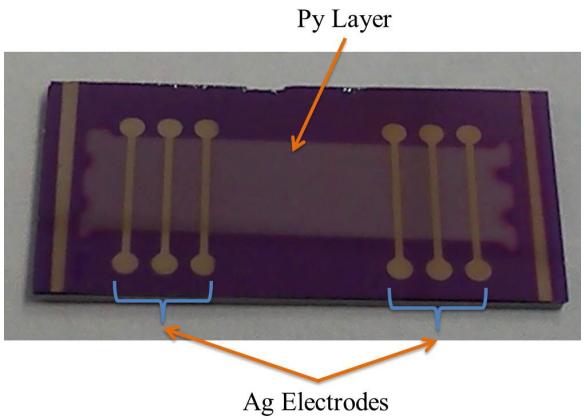

Figure 5.8: Sample after the deposition

First the mask with a long slit was placed on top of the substrate and the ferro-

magnetic layer was deposited. Then that mask was replaced with a mask with cross electrodes to deposit the Ag layers. The entire mask exchanging process was carried out at 200 nTorr vacuum. Figure 5.8 shows an example sample after the complete deposition process.

5.2.2 Measurement set up

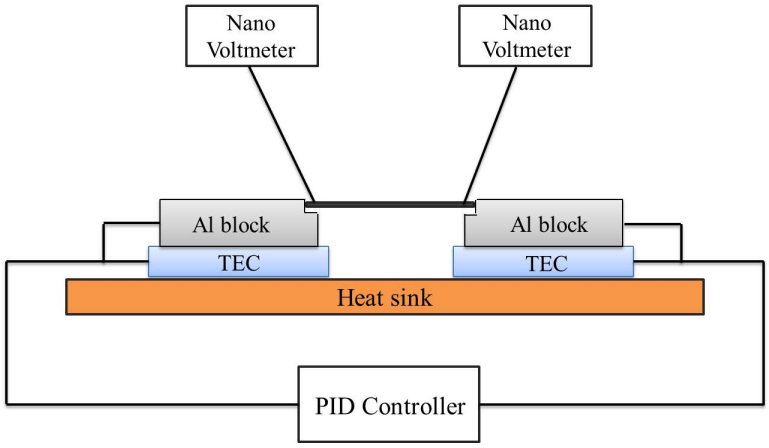

Figure 5.9: Schematic diagram of the experiment set up of measuring SSE

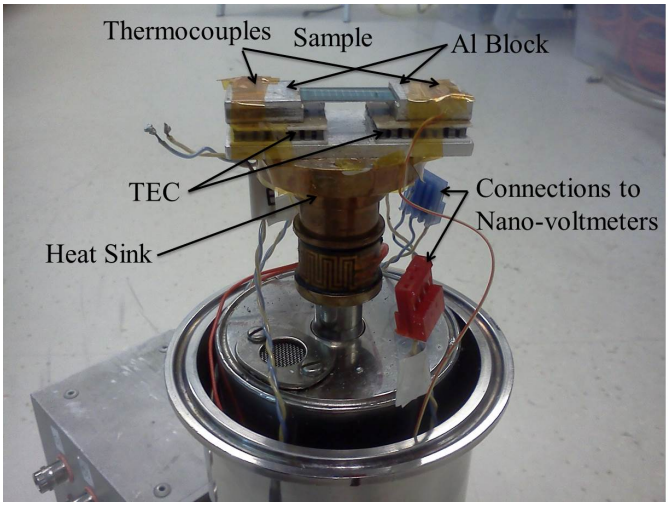

Figure 5.10: Experimental set up of the SSE

Our set up consists of two thermoelectric modules, a two channel PID controller, two nano-voltmeters, and a electromagnet. Figure 5.9 shows the schematic drawing of

the measurement set up where we apply a constant temperature gradient and then the resultant voltages are measured through nano-voltmeters. Figure 5.10 shows the actual set up.

5.2.3 Controlling the temperature

Since the measuring is directly dependent on the temperature, controlling it plays a significant role in this experiment.

Figure 5.11 shows the variation of the sample temperature and the measured voltage signal with the time, where only one TEC is under PID control. They exhibit a strong correlation with each other. Which demonstrates that it's necessary to have proper temperature during the experiment.

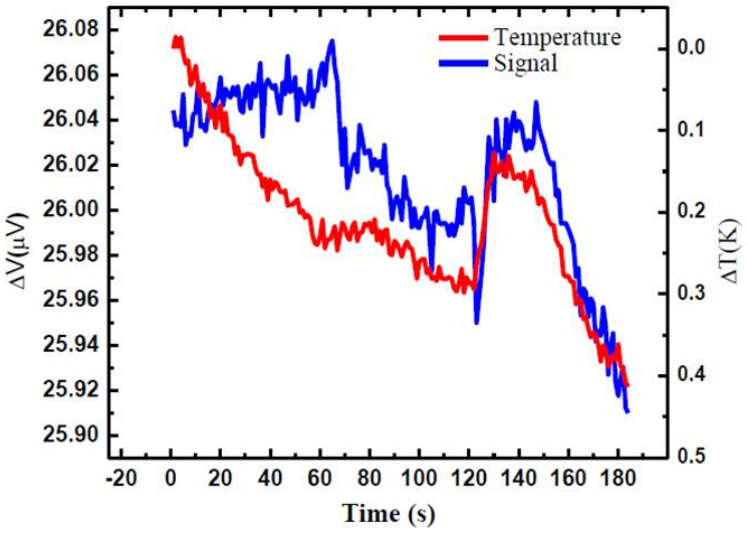

Figure 5.11: Variation of the signal and the temperature with the time

We used a STANFORD Research PTC10 PID controller for the temperature controlling. Two thermoelectric modules were directly powered through the PID controller. The temperatures were measured using two type K thermocouples placed on the Al blocks. When connecting the thermocouples to the Al block, a piece of Al_2O_3 substrate was used to avoid any electric contact between the thermocouple and the

Al block. Since we placed our samples directly on the Al blocks, current can leak into the Al. Use of Al_2O_3 prevents the flow of this current into the thermocouple and vice versa. Since Al_2O_3 is a good thermal conductor it does not creates a big temperature gap between the thermocouple and the Al blocks. To make good thermal contact between the Al blocks and the thermocouples, all the surfaces were connected with Ag paint. Finally the Al blocks were placed on top of the thermoelectric modules using a thermal compound "Arctic Ag", which provides a good thermal contact and at the same time prevents any current flowing in to the Al block.

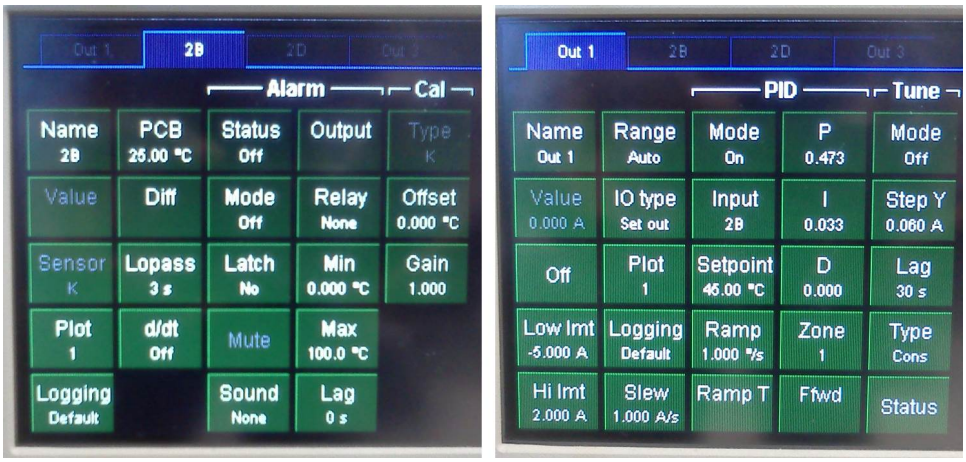

Figure 5.12: PID controller display. (Thermocouple settings(left) and PID parameters (right))

Before the experiment the temperature needs to have the optimum PID parameters for both channels. Since we were bridging the two thermal baths using the substrate, it's important to produce a similar environment during the calibration process. Otherwise the competition of the hot end and the cold end can lead to continuous fluctuations of temperature. During the calibration a constant current was applied to one TEC and allowed it to reach a relatively stable temperature near its ultimate operating temperature. After it stabilized, the PID parameters for other TEC were optimized using auto calibration mode. To avoid sudden temperature fluctuations the calibration process was done in "conservative mode". Once the P-I-D

for the first TEC was optimized, the other TEC's P-I-D were determined in similar manner. To reduce the noise on the temperature measurement, a 3 s low pass filter was used.

Once the PID settings were optimized, the temperature can be controlled with milli-Kelvin accuracy (using a 3 s low pass filters).

5.2.4 Measuring ANE on a Py thin film

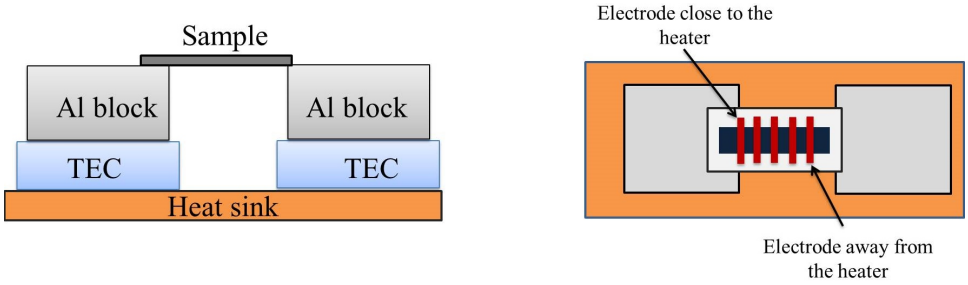

Figure 5.13: Sample mount for the ANE experiment. Top view (right), side view (left)

In this experiment, a 30 nm thick Py layer was deposited onto Si/SiO_x substrates, followed by 15 nm thick Ag cross electrodes were used. Ag electrodes were used due to their small spin hall angle, which leads to negligible SSE signal. Sample was mounted so that in one side the electrode is close to the heater and the other side the electrode is was away from the heat sink (fig.5.13). The ∇T_z should be higher close to the heater and lower as you move away from the heat sources.

The sample was mounted on the Al pieces using Arctic silver. A 90°C temperature difference was applied along the sample. The voltage signal was measured using nano-voltmeters, while sweeping the field between ±70 Oe.

Figure 5.14 shows the field dependence of the ANE signal in Py thin film with 90 K temperature difference along the sample. A hysteretic voltage signal was observed while sweeping the magnetic field. A bigger ANE signal was observed on the electrode closer to the heater, indicating the higher ∇T closer to the heater.

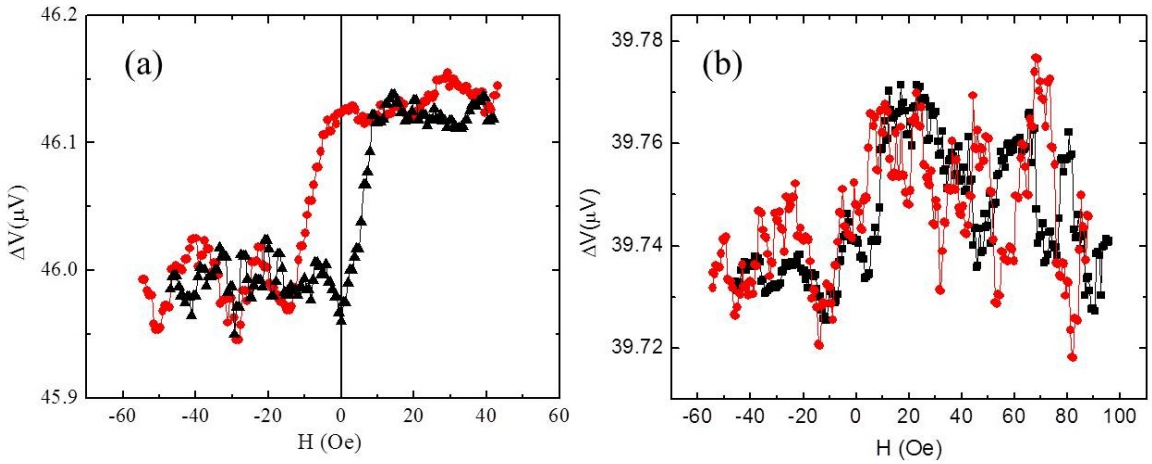

Figure 5.14: ANE signal on Py thin film when the magnetic field is parallel to the ∇T and 90 K temperature difference along the sample. electrode closer to the heater (left): electrode away from the heater (right)

The electrode placed away from the heat source showed an ANE signal, but with the same sign. To minimize the ANE signal on thin films, we find that the measurement electrodes should be placed away from the heat sources by at least 3 mm (about 6 times the substrate thickness).

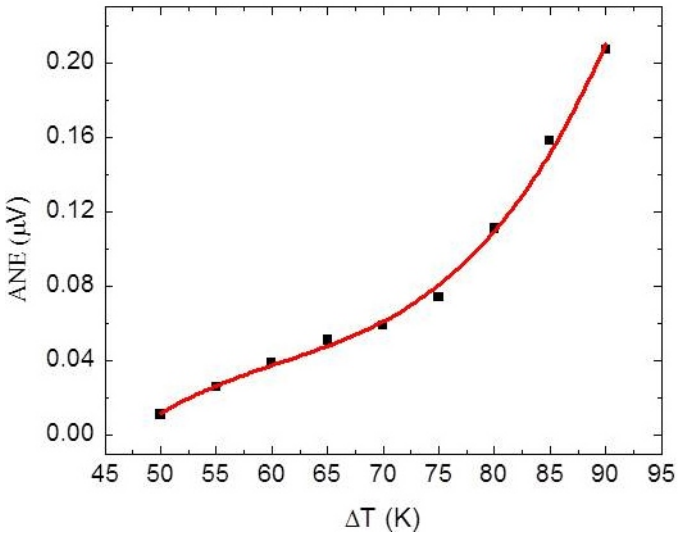

Figure 5.15: Temperature gradient dependence of the ANE signal

A dependence of the ANE signal on the in-plane temperature gradient was measured by changing the temperature difference in 5° steps. After changing the tem-

perature the measurement was paused until the temperature stabilizes. In each step a full field sweep was carried out.

The ANE signal shows cubical variation with respect to in-plane temperature difference (fig. 5.15). When the temperature difference is Below 50°C, the signal was disappeared (i.e. fell below the detection limit of $\sim$ 10 nV). This suggests that, if the in-plane temperature difference is kept below 50°C, it's possible to eliminate the ANE signal.

5.3 Efforts to minimize ANE in thin films.

Several experiments were carried out to find an effective method to remove the ANE from the thin films. In this section we describe a study we did by placing a SiO_x cap on the sample to minimize the out of plane temperature gradient.

A 20 nm thick Py layer was deposited onto Si/SiO_x substrates, by 10 nm thick Ta cross electrodes were used. The sample was mounted onto the set up as shown in fig. 5.16. First the sample was placed on two Al pieces with ledges. Then another piece of Si/SiO_x substrate was placed on top of the sample so that it covers the entire ferromagnetic layer to reduce the heat dissipation from the top of the sample. The width of this cap was greater than the width of the ferromagnetic layer but smaller than the length of the cross electrodes (fig.5.16 (left)) so there is enough space for making the contacts.

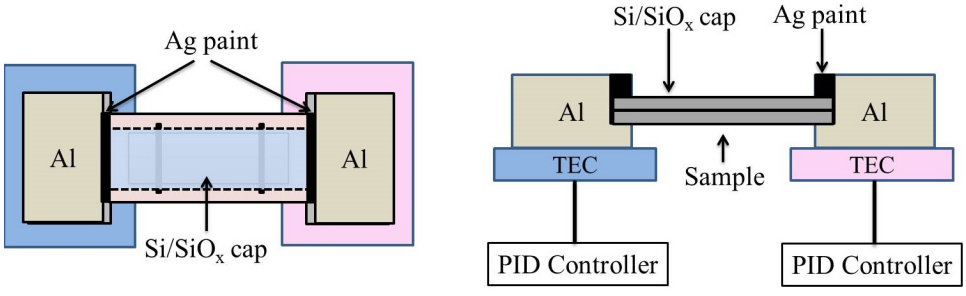

Figure 5.16: Sample mount for the ANE experiment. Top view (left), side view (right)

The entire ledge in Al block was filled with Ag paint, which effectively embeds the chip in the thermal bath. This should reduced the ∇T in z direction because both the top and bottom of the substrate are attached directly to the heat source. Also the Si/SiO_x cap should reduce the heat dissipated into the vacuum, further reducing the ∇T_z.

A temperature difference of 50 K was applied along the 20 mm length of the sample with cold side at 0 °C and hot side at 50 °C. This gave a ∇T of 2.5 K/mm along the sample. The resultant voltages transverse to the temperature gradient were measured across the Ta stripes on the hot and cold sides simultaneously. The field dependence of the signal was measured by placing the set up inside an electro magnet and sweeping the field between ± 200 Oe.

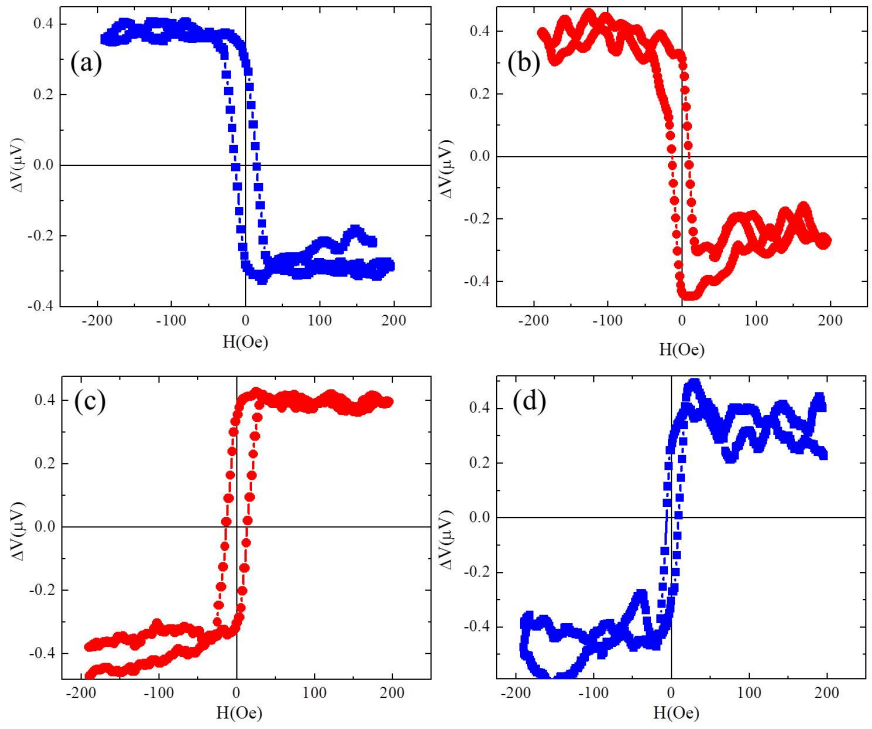

Figure 5.17: Field dependence of anomalous Nernst effect signal on cold side (a) and hot side (b) of a 20 nm of Py layer with 10 nm thick Ta cross electrodes with ∇T of +2.5 K/mm:(c) and (d) show the ANE signal when the sign of the ∇T (-2.5K/mm) flipped.

A hysteretic voltage was observed with the sweeping field. Both loops showed the same coercivity. In contrast to the spin Seebeck effect, both ends exhibited a the signal with same sign. This confirms the presence of anomalous Nernst effect in the sample even with the efforts to minimize the ∇T_z. The direction of the temperature gradient was changed by flipping the temperatures of individual thermoelectric modules and then the resultant voltages were measured similar to the previous case. The sign of the signal flipped when we changed the sign of ∇T as expected.

The dependence of the transverse voltage signal on the magnitude of the temperature gradient was measured by changing the temperature difference from +90 K to -90 K. At each step a full field sweep was carried out.

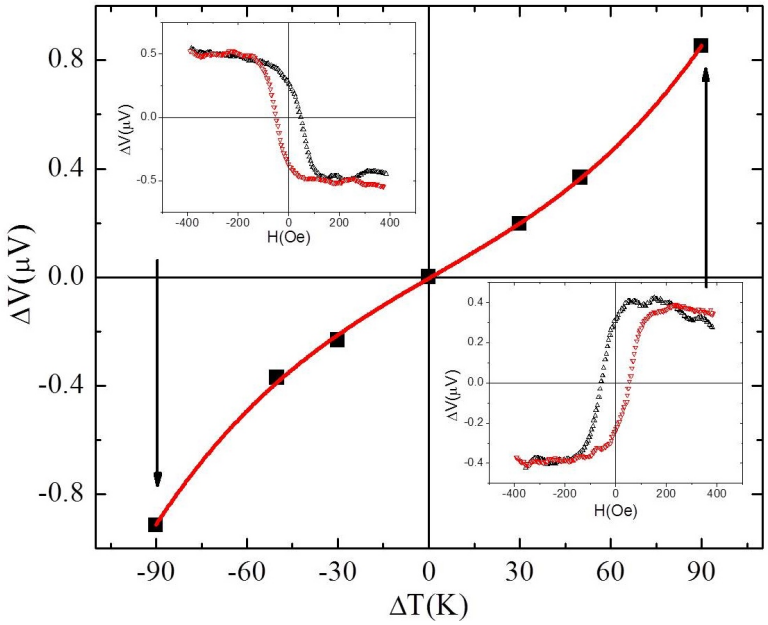

Figure 5.18: Temperature difference dependence of ANE signal on a Py/Ta sample at $\theta = 0$. Insets show the field dependence of the signal on $\pm$ 90 K temperature differences.

As shown in fig.5.18 the ANE signal showed a cubic relation with the temperature gradient. At lower temperature gradients the signal changed nearly linearly with the temperature difference. But with the higher temperature differences the signal deviated from the linear regime. This suggests that when the in-plane temperature

difference is increased, a larger out of plane temperature gradient (∇T_z) results.

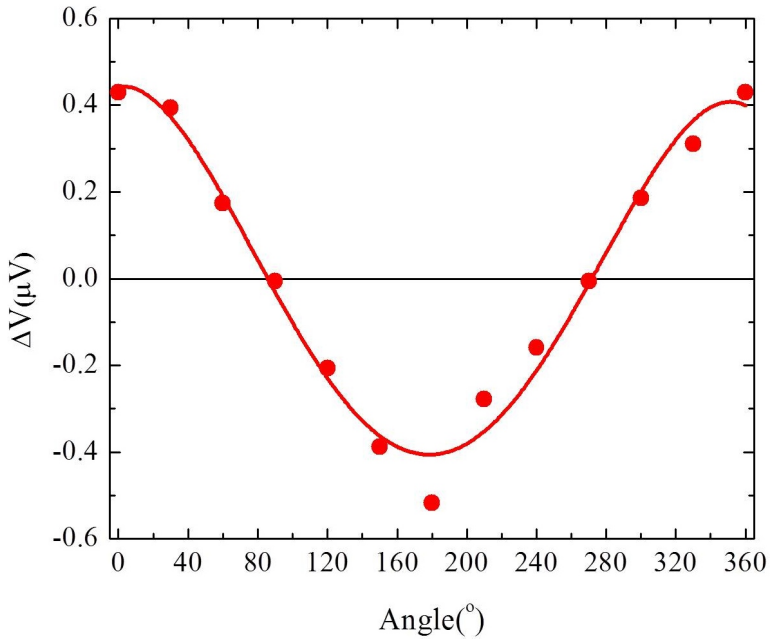

Figure 5.19: Dependence of ANE signal of a Py/Ta sample on angle between the in-plane temperature gradient and the field.

The angular dependence of the ANE signal was studied by changing the angle between the in-plane temperature gradient and the applied magnetic field in 30° steps, and completing a field sweep at each angle. The ANE signal showed a $\cos\theta$ relation as shown in fig.5.19 which is expected because $E_y \propto -M_x \times \Delta T_z$.

This study confirms that the cap placed on top of the sample has created an additional out of plane temperature gradient leading to an ANE signal on the Py thin film. The ANE signal with same sign at hot end and cold end suggests that the resultant out of plane temperature gradient is in same direction at both ends(fig.5.20).

In the next study, we demonstrated that ANE can lead to opposite out of plane temperature gradients at the two ends. Here a sample with 20 nm thick Co layer deposited on to a Si/SiO_x substrate was used with 10 nm thick Ta stripes. To create opposite temperature gradients at the cold and hot ends two separate Si/SiO_x

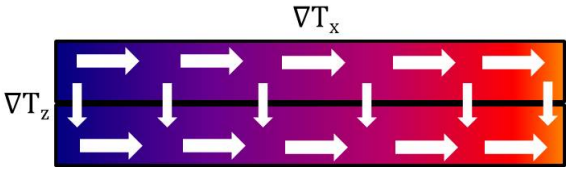

Figure 5.20: Direction of the temperature gradients in the sample and the cap.

substrates were placed on top of the sample with a gap at the middle.

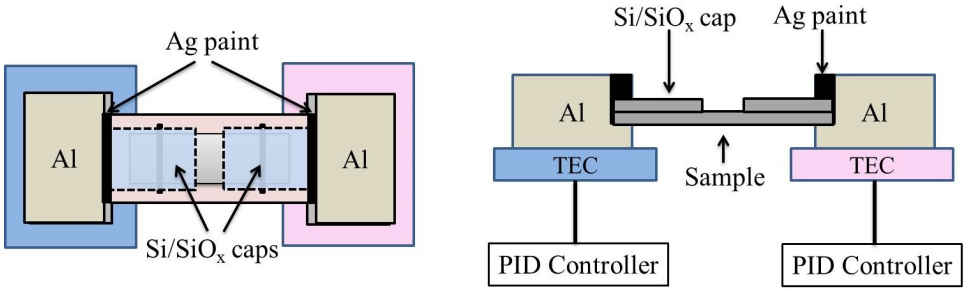

Figure 5.21: ANE set up with two Si/SiO_x caps on the sample. Two caps generates out of plane temperature gradients in opposite directions in tow ends

As shown in the fig. 5.21 two caps were place on top of the sample and Ag painted at the ends to maintain the same temperature at ends.

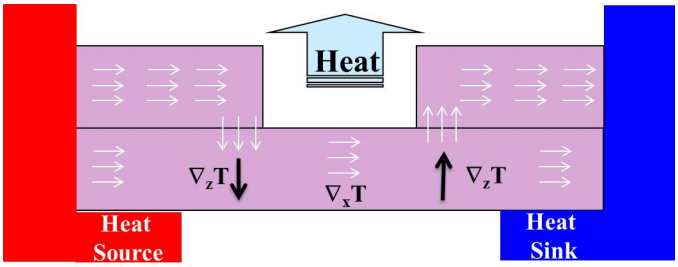

Figure 5.22: Cartoon of heat flow on the ANE set up with who Si/SiO_x caps on the sample with a gap at the middle

When a temperature gradient was applied to the set up, heat flows through both substrates parallel to each other. When it reaches the gap, the heat current through the top substrate must enter the bottom substrate creating a heat flow from top to bottom. This allows us to intentionally create temperature gradient in the z direction.

As the heat current flows past the gap, the top substrate on the cold side absorbs heat from the bottom substrate creating a heat flow from bottom substrate to the top substrate. This creates an out of plane temperature gradient in z direction with opposite sign to the left cap (from bottom to top) (fig.5.22).

A 90°C temperature difference was applied between two thermal baths, giving a supposed 4.5 K/mm in-plane ∇T. The field dependence of the signal was measured by sweeping the external magnetic field between $\pm$ 400 Oe .

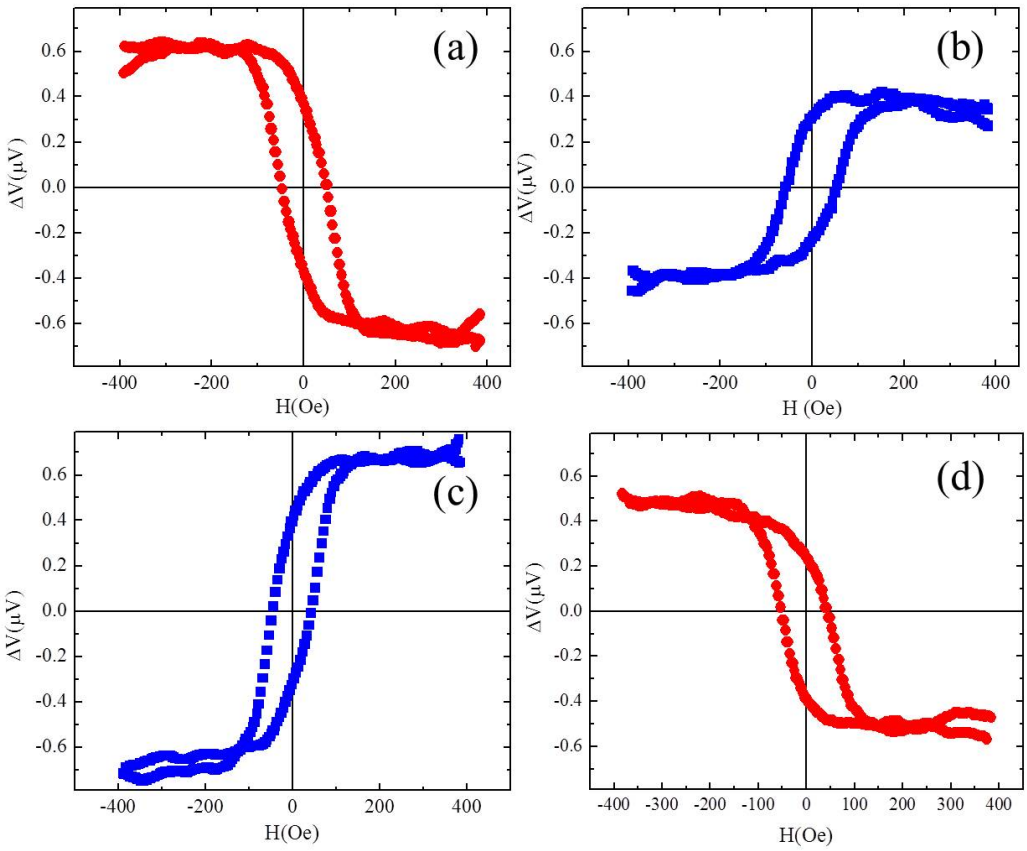

Figure 5.23: Field dependence of the ANE signal of Co/Ta sample with two Si/SiO_x chips on top of the sample with a gap in the middle at 90°. (a)hot end,(b)cold end with ∇T of +4.5 K/mm: (c) cold side,(d) hot side after changing the sign of ∇T (= -4.5 K/mm)

A hysteretic change in the voltage was observed for both the hot and cold ends with

similar coercivities. In contrast to the previous experiment, the signs of the signals at each end were opposite to each other (fig.5.23). The origin of this sign difference is the opposite temperature gradients along z, as indicated in fig5.22. When the direction of the temperature gradient was flipped, an inverted field dependence was observed with the signals from both ends (fig. 5.23 (c),(d)). These data confirm that the sign of the ANE signal depends on the direction of the out of plane temperature gradient, even with the in-plane ∇T, it's possible to generate an out of plane temperature gradient.

To study the angular dependence of the ANE signal the sample was rotated by changing the angle between the applied field and the ∇T.

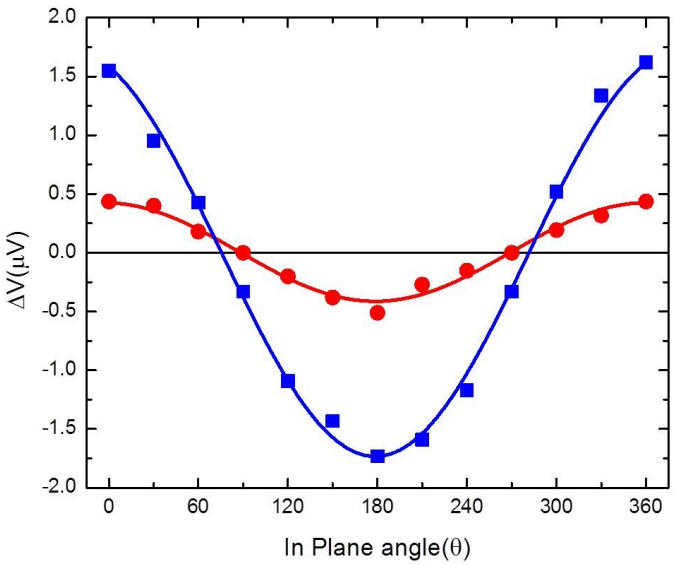

Figure 5.24: Dependence of ANE signal of Co/Ta sample with one (red) and two (blue) Si/SiO_x chips on the angle between the in-plane temperature gradient and the magnetic field.

Figure 5.24 shows the complete angular dependence of the ANE signal of the Co/Ta sample with two Si/SiO_x chips on it. The ANE signal changed in a $\cos\theta$ relation. In comparison to the single cap experiment, the ANE signal magnitude was relatively larger in the two cap experiment. This indicates that the two cap configuration generates a greater out of plane temperature gradient. It is possible that there might be a spin Seebeck signal inside the above signal. However it is impossible

to resolve due to the ANE signal. The Si/SiO_x caps placed on top of the samples generates out of plane temperature gradients by absorbing the heat from the sample. Therefore it's not a suitable method to use in these type of measurements. In measuring spin Seebeck effect care has to be taken to avoid these out of plane temperature gradients. Because spin Seebeck effect like ANE signal can be easily obtained by out of plane temperature gradients generated by improper sample mounting. Since both spin Seebeck effect and ANE have similar properties like field dependence and angular dependence it's impossible to distinguish the two effects unless an electrode that has nearly zero spin hall angle is used.

5.3.1 Sample Mounting and connecting leads

As we showed in the previous section temperature profile of the sample can be significantly affected, depending on the sample mounting. In SSE measurements the temperature gradient should be in the sample plane and along the length of the substrate. Any temperature gradient out of the plane would lead to other phenomenon like anomalous Nernst effect [67]. Therefore the sample should be mounted in a way that minimizes the out of plane temperature gradient.

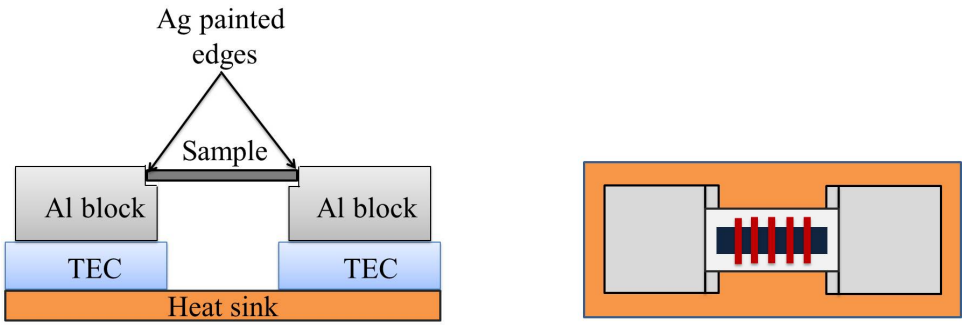

Figure 5.25: Sample mount from the side view(left) and the top view (top)

As shown in the figure 5.25 we have found it important to mount the sample to the Al blocks from the edges using Ag paint. In this way thermal current can only

flow into the sample from its edges. This minimizes the out of plane temperature gradient close to the heat sources. Figure 5.26 shows the flow of thermal current inside the substrate from hot end to the cold end.

Figure 5.26: Thermal current flow inside the substrate

To measure the resultant voltages across the electrodes, thin Cu wires were connected to the electrodes using Ag paint. As shown in figure 5.8 we made the cross electrodes longer than the width of the ferromagnetic layer. This allowed us to make electrical contacts away from the ferromagnetic layer (Fig. 5.27). If those contacts were close (or on top of) to the ferromagnet they can absorb heat out of the ferromagnet/substrate and create non-uniform temperature gradients around the contacts (possibly leading to ANE).

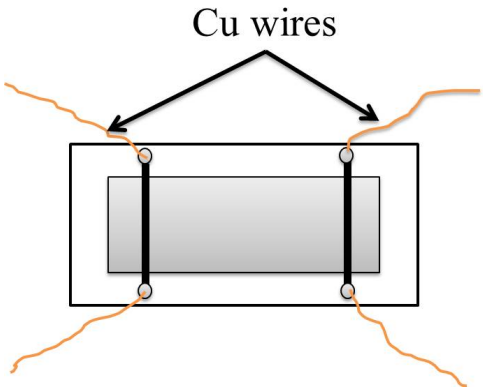

Figure 5.27: Cu wires connected to the sample

5.3.2 Efforts to measure the spin Seebeck effect

Several attempts were carried out to measure the SSE on Py thin films with Au cross electrodes. First a 10 nm thick Au cross electrodes were directly deposited onto

Si/SiO_x substrates using e-beam evaporation. Then the sample was transferred into the Ar ion sputtering system for the Py deposition. Before Py deposition, the sample was rf-bias sputtered for 1 minute at 3 mTorr pressure to get rid of any contamination at the Au surface. 20 nm of Py layer was deposited onto those electrodes at room temperature and 3 mTorr pressure. The sample was mounted on the measurement set up and contacts were made for voltage measurements. A temperature gradient of 1.8 K/mm was applied along the sample to produce the spin accumulation on the Py layer. The resultant voltages at both the hot end and the cold end were measured simultaneously using nano-voltmeters, as the field was swept.

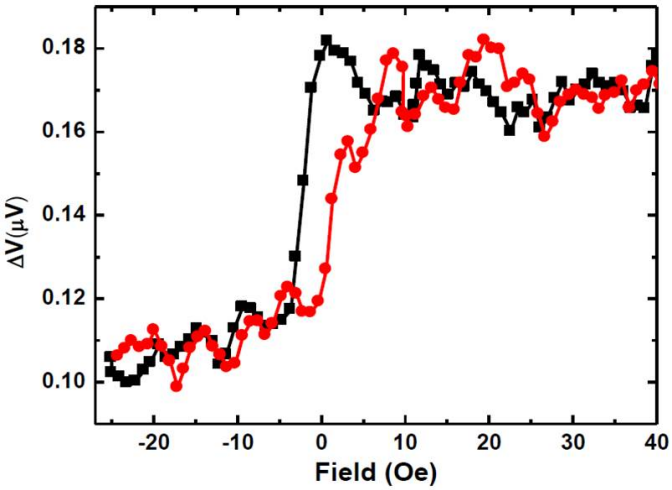

Figure 5.28: SSE measured on Ag/Py sample

With our first attempt we observed a hysteresis curve shaped signal at the hot end of the sample with 50 nV magnitude (Fig.5.28), but we did not observe any change at the cold end. Then the same experiment was repeated several times with the same sample and a new sample with same configuration. The previous signal was not reproducible. However, an anisotropic magneto resistance shaped signal was observed on the both sides of these sample reproducibly. Furthermore, the signals from both ends had the same sign, suggesting they are not related to the SSE. Anything related to SSE should have opposite signs at opposite ends because J_s has opposite sign at

hot and cold sides.

The signals at both ends flipped sign upon changing the sign of the temperature gradient. This indicates that the signal only depends on the direction (and magnitude) of the temperature gradient and not the individual temperatures of the side. This observation matches with planar Nernst effect not SSE or ANE.

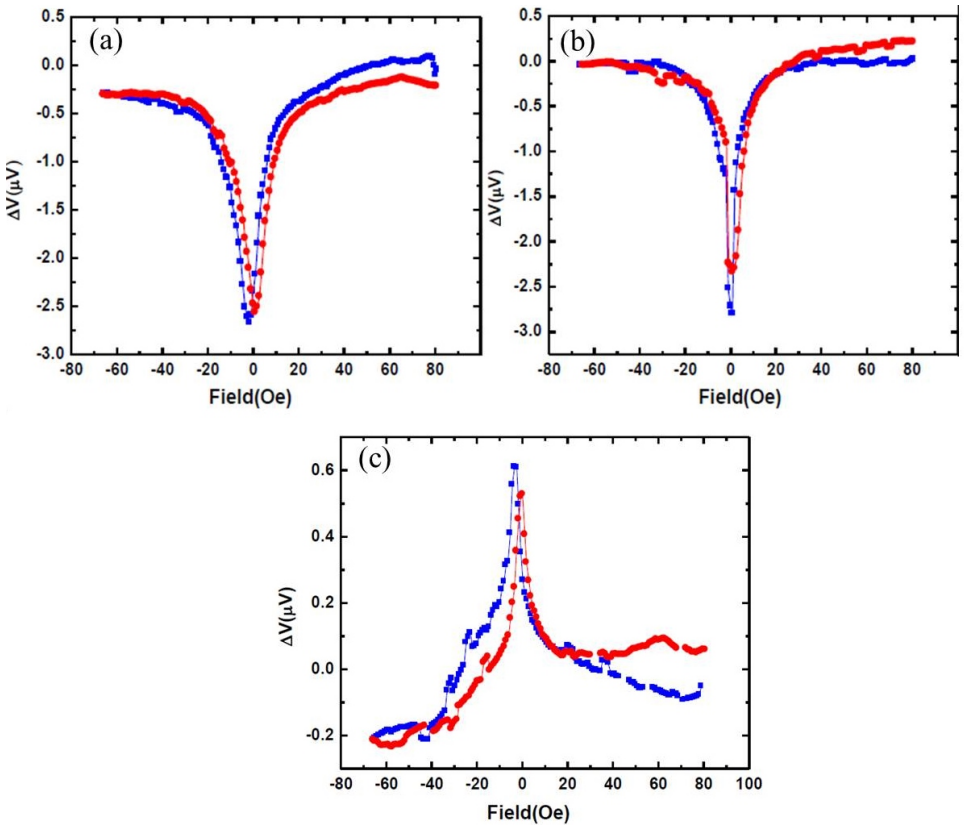

Figure 5.29: Signal on the hot(left) and cold(right) sides of the Ag/Py sample

The same experiment was repeated with different materials. Here 20 nm of Co was used as the ferromagnetic material and 10 nm thick Ta was used as the cross electrodes. Then a 1.8 K/mm temperature gradient was applied along the sample and resultant voltages were measured.

In this case also a signal that looks somewhat similar to an AMR peak was observed on both sides with same sign at both ends. And the signs of the signals at both ends were flipped upon changing the direction of the temperature gradient from

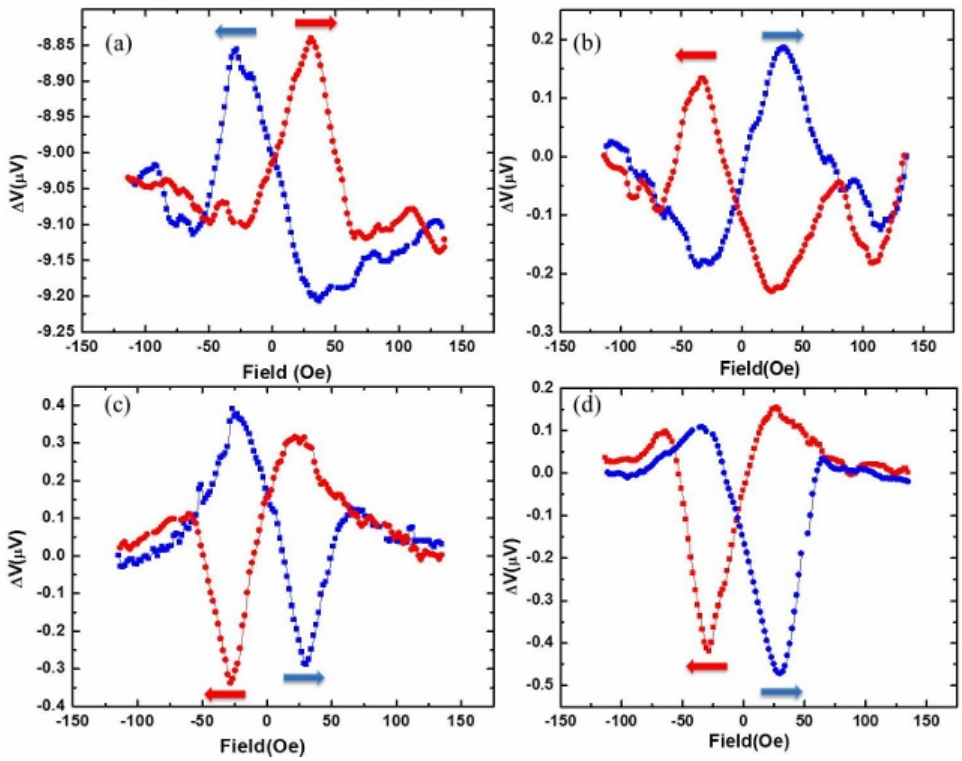

Figure 5.30: PNE Signal from the hot side(a) and the cold side(b) of the Co/Ta sample with $\nabla T = 1.8K/mm$. PNE signal when the sign of the ∇T changed. (c) cold side, (d) hot side.

+1.8K/mm to -1.8K/mm (fig. 5.30).

All the above data indicates that the resultant voltage signal was related to the direction of the temperature gradient and it's magnitude. Considering this face with the shape of the signal it is possible to conclude that the above signal was related to planar Nernst effect.

5.4 Anisotropic Magnetothermopower on Py thin films

When a temperature gradient is applied to a material an electrical voltage develop along the temperature gradient. This is called the Seebeck effect or longitudinal thermopower. The longitudinal thermopower of a metal with ∇T temperature gradient is described by the Mott equation.

$$\alpha(E) = -\frac{\pi^2 {k_B}^2 T}{3e}[\frac{1}{\rho(E)}\frac{\partial\rho(E)}{\partial E}]_{E=E_F}$$

where, ρ is the resistivity of the metal and E_F is the Fermi energy and k_B is the Boltzmann constant.

The thermopower has an inverse relation with the resistivity of the metal. Similarly, when a temperature gradient is applied to a ferromagnetic material, thermopower interact with the magnetization of the material to give magnetothermopower. Due to the anisotropic nature of the resistivity in ferromagnetic materials, the magnetothermopower should also be anisotropic.

When a temperature gradient and a magnetic field are applied to a ferromagnetic material, an electric field is induced on the same plane. This effect depends on $\vec{M}$ and ∇T known as magnetothermopower. Two types of magnetothermopowers can be defined according to the voltage measurement configuration: longitudinal magnetothermopower (also known as spin dependent Seebeck effect), where the resultant voltage is measured parallel to the temperature gradient and transverse magnetothermopower (known as planar Nernst effect), where the resultant voltage is measured transverse to the temperature gradient [68]. The mechanism behind the magnetothermoeffect is believed to be the spin dependent scattering, but this has not been thoroughly treated in thin films [69]. In this study we report measurements of both longitudinal and transverse magnetothermopowers and provide a comparison with anisotropic magneto-resistance. The origin of AMR is also spin dependent of scattering of conduction electrons. Therefore it's worth looking into both magnetothermopower and magnetoresistance in the same sample.

5.4.1 Transverse magnetothermopower (Planar Nernst effect)

The magnitude of the planar Nernst effect (E_y) is proportional to

$$E_y \propto M^2 \ \sin\theta.\cos\theta.\nabla T$$

Where M is the magnetization, ∇T is the temperature gradient and the θ is the angle between the magnetization and the temperature gradient [70].

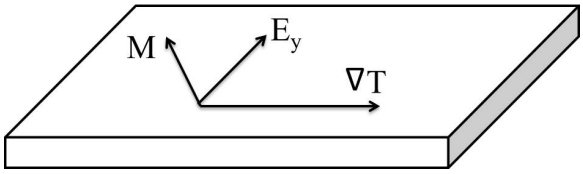

Figure 5.31: PNE on a thin film, magnetization is confined to the plane.

Here both magnetization and the temperature gradient are in the same plane and the resultant voltage is also in the same plane

5.4.2 Longitudinal magnetothermopower (Spin Dependent Seebeck Effect)

In longitudinal magnetothermopower measurements the temperature gradient is applied along the length of the sample and the resultant voltage measured parallel to the ∇T. Similar to PNE the M is confined to the plane.

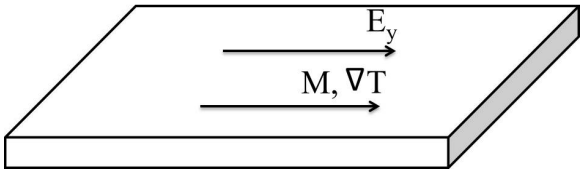

Figure 5.32: The Longitudinal magnetothermopower was measured parallel to the ∇T on same plane.

The origin of this effect is related to spin dependent scattering of conduction electrons similar to the AMR [71]. Since the voltage is measured parallel to the ∇T, a strong background signal due to the regular Seebeck effect of the ferromagnet exists in addition to the SDSE of the ferromagnet.

5.4.3 Sample Preparation

Samples were prepared using an Argon ion sputtering system similar to the SSE measurements. A 20 nm thick Py layer was deposited on to (2×1) cm Si/SiO_x substrates at room temperature with an applied growth magnetic field of 100 Oe. The magnetic field was applied during the deposition to give the sample uni-axial anisotropy. 15 nm thick Ag cross electrodes were deposited at room temperature on the Py layer for the voltage measurements. The *in situ* mask exchanging system was used during the deposition to prevent any kind of oxidation occurs at the interfaces. Ag was used as the cross electrode material because it's spin hall angle is almost zero. Therefore, there will be no voltage generated from the inverse spin hall effect,and this zero contributions from any spin Seebeck effect.

5.4.4 Longitudinal and Transverse Magnetoresistance measurements on Py thin film

Anisotropic Magnetoresistance (AMR) is an phenomenon that explains the dependence of electrical conductivity on the direction of the magnetization of a ferromagnet. The origin of the AMR is believed to be the spin dependent scattering (s-d scattering) facilitated by the spin orbit interactions [72]. AMR of any ferromagnetic material varies as

$$\Delta\rho(H) = \Delta\rho\ (\cos^2\theta - \tfrac{1}{3})$$

where $\Delta\rho = \rho_{\parallel} - \rho_{\perp}$ and θ is the angle between the current and the magnetization [72]. $\rho_{\parallel}$ is the resistivity of the sample when the magnetization is parallel to the current flow direction and $\rho_{\perp}$ is the resistivity when the magnetization is perpendicular to the current. In this experiment both longitudinal and transverse magneto-resistance (MR) measurements were carried out at room temperature.

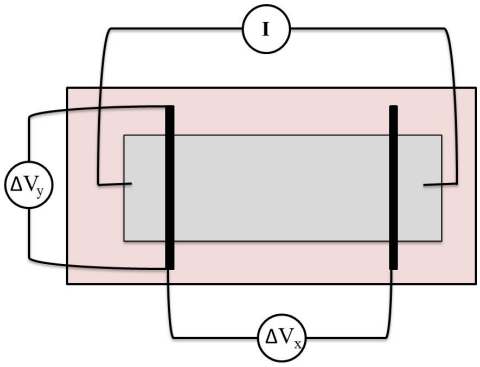

Figure 5.33: MR measurement set up

As shown in the fig. 5.33 a constant current of 200 μA was applied along the length of the sample using a current source. The longitudinal and the transverse voltages were measured using nano-voltmeters. The MR was calculated using Ohm's law.

The field dependence of the MR was measured by sweeping the external magnetic field parallel to the current between $\pm$100 Oe at a rate of 4 Oe/s. Both longitudinal and transverse MR showed traditional AMR behavior with the same coercivities (5.34). The magnitude of the transverse MR was smaller by an order of magnitude relative to the longitudinal MR. This could be an effect of shorting out electrons within the Ag stripe. In traditional AMR measurements the voltages are measured through point contacts, but in this case a continuous Ag stripe was used to measure the resultant voltage for consistency with the SSE geometry. Therefore the electrons passing into the Ag stripe from the Py layer can be shorted within the Ag layer, lowering the resultant voltages. Therefore it may not be suitable to compare the magnitudes of the signal from the transverse MR to that of longitudinal MR.

The angular dependence of the PNE was measured by changing the angle between the current (I) and the magnetic field (H) by rotating the sample in the electromagnet (fig. 5.35).

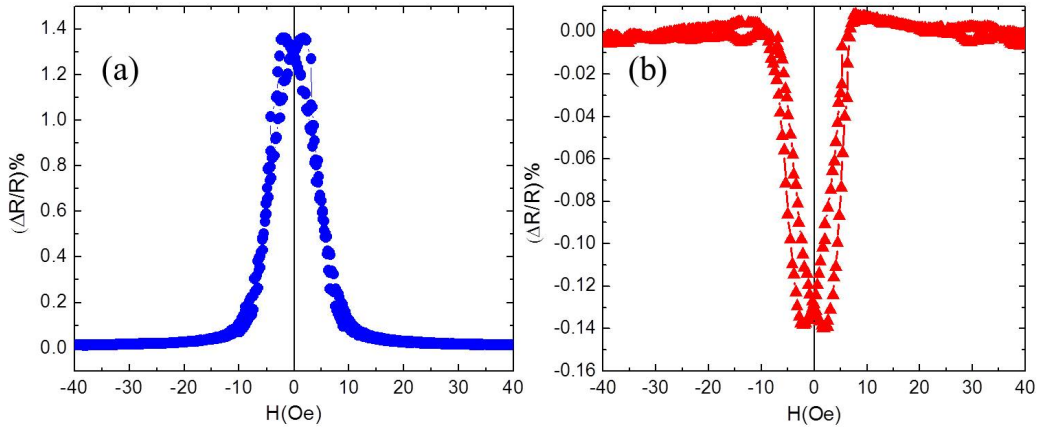

Figure 5.34: Field dependence of longitudinal (a) and transverse (b) MR

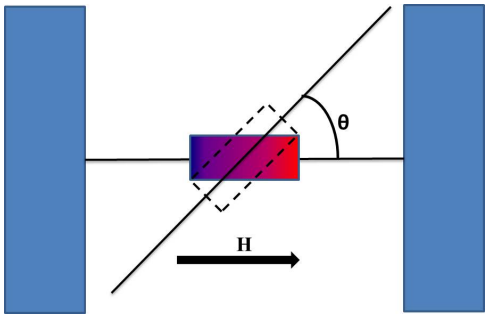

Figure 5.35: Sample was rotated between the poles of the electromagnet to change the angle between ∇T and H

The set up was rotated from 0° to 360° and the data was collected in 20° steps. A full field sweep was carried out at each angle as both longitudinal and transverse MR were measured. The percentage change of ΔR was plotted against the respective angle. The ΔR was calculated by subtracting the $R_{\perp}$ from the $R_{\parallel}$ values. Previous studies have shown that changes in $R_{\parallel}$ only do not represent the correct behavior of AMR relative to the angle [73]. For proper interpretation, the percentage change in $(\frac{\Delta R}{R})$ was plotted against the respective angle. For both longitudinal and transverse MR, $(\frac{\Delta R}{R}) = \frac{R_{\parallel} - R_{\perp}}{R_{\parallel}}$.

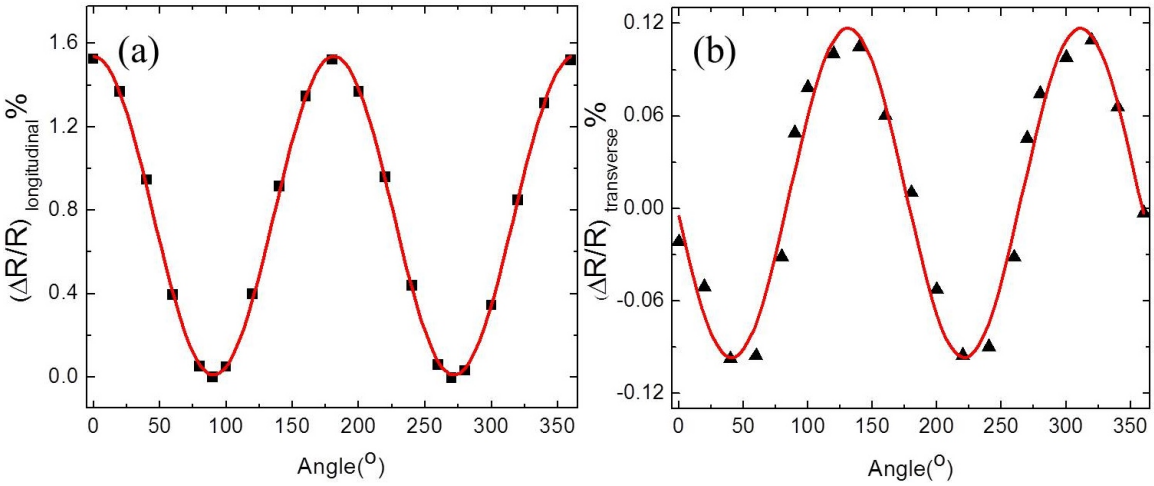

Figure 5.36: Dependence of longitudinal (a) and transverse (b) MR on the angle between current and magnetic field

The maximum MR was observed when the current and the field were parallel to each other (fig.5.36 a); zero MR was observed when they were normal to each other. Therefore longitudinal MR showed $\cos^2\theta$ relation to the angle between the current and the field proving the traditional AMR behaviour. In contrast, the transverse MR showed a different angular dependence. It showed zero MR when current and the field are parallel and normal to each other, and showed maximum MR when the angle between the current and the field is equal to odd multiples of 45° (fig.5.36 b). This implies a $\sin(2\theta)$ dependence.

After the above experiments the same sample was used to measure the magnetothermopower measurements.

5.4.5 Measuring Transverse and longitudinal magnetothermopower of Py thin films

The sample was mounted on the set up using Ag paint similar to the SSE measurements. A 30K temperature difference was applied along the length of the sample creating 1.5K/mm temperature gradient with hot side at 50 °C and cold side at 20 °C.

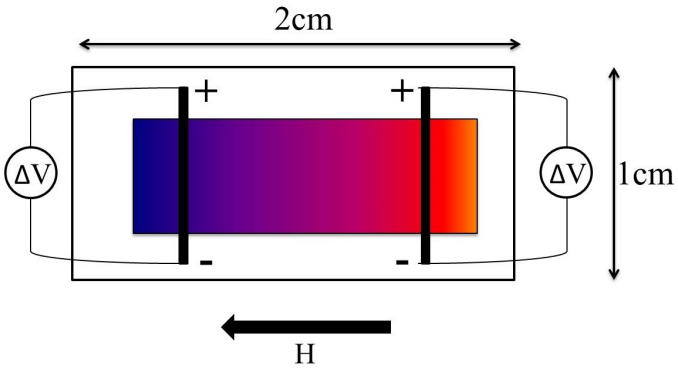

Figure 5.37: Longitudinal magnetothermopower measurement

The resultant voltage was measured transverse to the temperature gradient as shown in the fig. 5.37. When connecting the nano-voltmeters to the sample, the same polarity was used in all the measurements. The voltages were measured on both the hot side and the cold side simultaneously. An external magnetic field was swept between ± 100 Oe at a rate of 4 Oe/s parallel to the temperature gradient. This $\frac{dM}{dt}$ was optimized so that no smearing of data occurred. We tried stepping the field, but this was abandoned because it gave the same results but too much longer.

Continuous sweeping of the field induced a significantly large signal due to induction. Figure 5.38 shows the induction of the data cause by the field sweeping. This was removed by averaging the saturated values of the curves. The induction can never be eliminated but can reduced by decreasing the sweeping rate of the field and the minimizing the area created by wire loops, though this will vary with θ.

Since the ∇T and M have a $\sin(2\theta)$ relationship with the PNE, the largest signal is expected when the angle between the those two are $45°(2n+1)$, where n is an integer.

Figure 5.39 shows the field dependence of the biggest PNE signal observed at both hot and cold ends at 45° after removing the induction. The signals show field dependence similar to the AMR, where voltage peaks were observed at fields corresponding to the magnetization reversal. The signals from both ends have the same sign. This confirms that the PNE depends on the ∇T but not the individual temperatures at

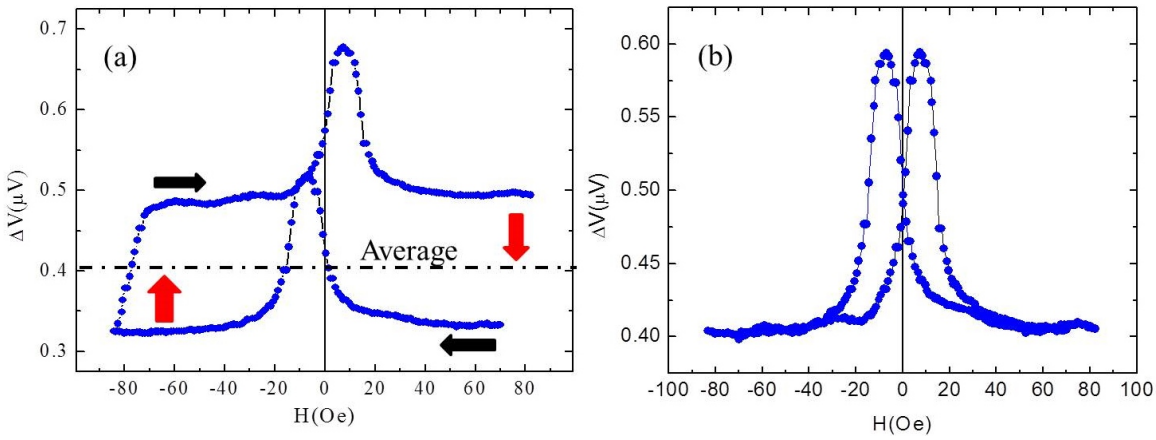

Figure 5.38: Induction cause by the sweeping of the field removed by averaging the curves.(a) raw data, (b)after removing the background. at $\theta = 90°$

each end. PNE showed a higher percentage change in the signal relative to the background voltage. The background voltage was resultant from the longitudinal ∇T. Since the effect of longitudinal ∇T on the transverse direction is low, the resultant background voltage in the transverse directions is also low. Therefore relative to that background signal the percent voltage change in PNE is significant.

Next the field dependence of the longitudinal magnetothermopower (MTP) was measured with the same set up. In this case the resultant voltage was measured parallel to the ∇T as shown in the fig. 5.40.

When connecting the nano-voltmeters to the sample the positive terminal was connected to the hot side and the ground terminal connected to the cold side. The field dependence of the signal was measured by sweeping the external magnetic field between $\pm$100 Oe at a rate of 4 Oe/s. All the experimental parameters such as sweep rate and the field range kept fixed in all the experiments for proper comparison.

Similar to the PNE, an AMR like field dependence was observed. This indicates the anisotropic nature of the SDSE. Due to the significantly larger background signal the percentage change in the SDSE is relatively low.

The angular dependence of the PNE and SDSE was measured by changing the

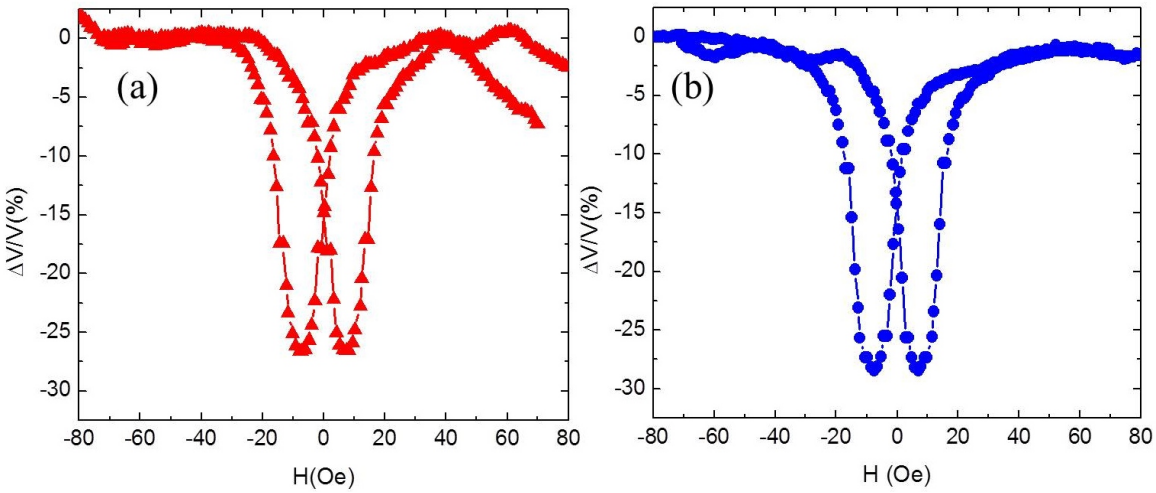

Figure 5.39: PNE when $\theta = 45°$at hot side (a) and cold side (b)

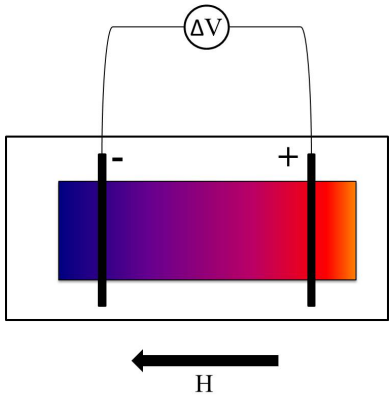

Figure 5.40: Longitudinal magnetothermopower measurement set up.

angle between ∇T and H by rotating the sample in the electromagnet .

The set up was rotated from 0° to 360° and the data was collected in every 20° steps. In each step a full field sweep was carried out. Similar to the AMR data in plotting the angular dependence data instead of plotting the raw voltages, the ΔV was calculated using $V_{\parallel}$ and $V_{\perp}$ ($\Delta V = V_{\parallel} - V_{\perp}$). Then the percentage $\frac{\Delta V}{V_{\parallel}}$ change was plotted against the respective angle. $V_{\parallel}$ is the resultant voltage when the magnetization of the sample is parallel to the ∇T. $V_{\perp}$ is the resultant voltage when the magnetization of the sample is perpendicular to the ∇T.

Figure 5.43 shows the angular dependence of longitudinal (a) and transverse (b)

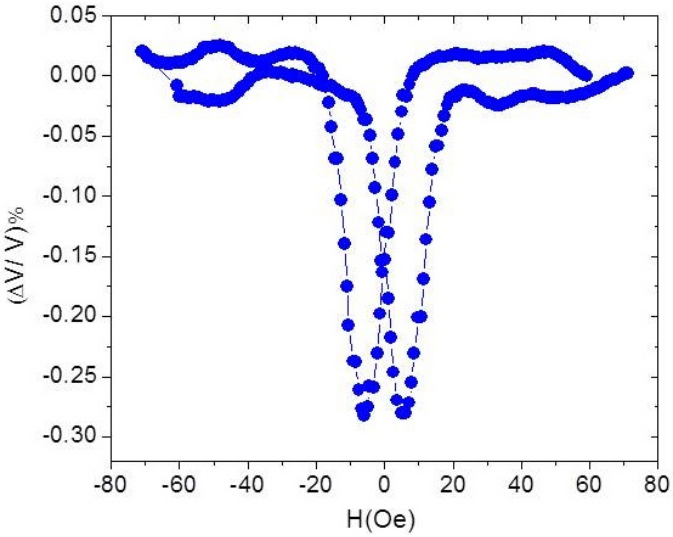

Figure 5.41: Field dependence of longitudinal magnetothermopower at $\theta = 45°$

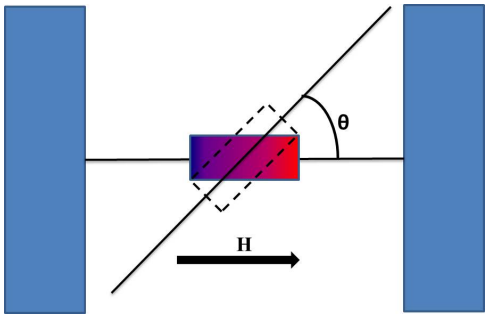

Figure 5.42: Sample was rotated between the poles of the electromagnet to change the angle between ∇T and H

magnetothermopower. Longitudinal MTP showed maximum voltage change when the magnetic field is parallel to the ∇T and didn't change the sign of the signal throughout the rotation giving a $\cos^2(\theta)$ relationship. This is exactly similar to the behaviour of the longitudinal magnetoresistance of fig. 5.36. The transverse MTP showed maximum voltage change at odd multiples of 45° and zero ΔV when the current and the field are parallel and normal to each other. The sign of the signal changes every 90°, leading to a $\sin(2\theta)$ type of relation as shown in previous studies [70].

Next the PNE signal was measured as a function of ∇T. As shown in fig. 5.44, the temperature of one end was changed while other end was hold at constant tem-

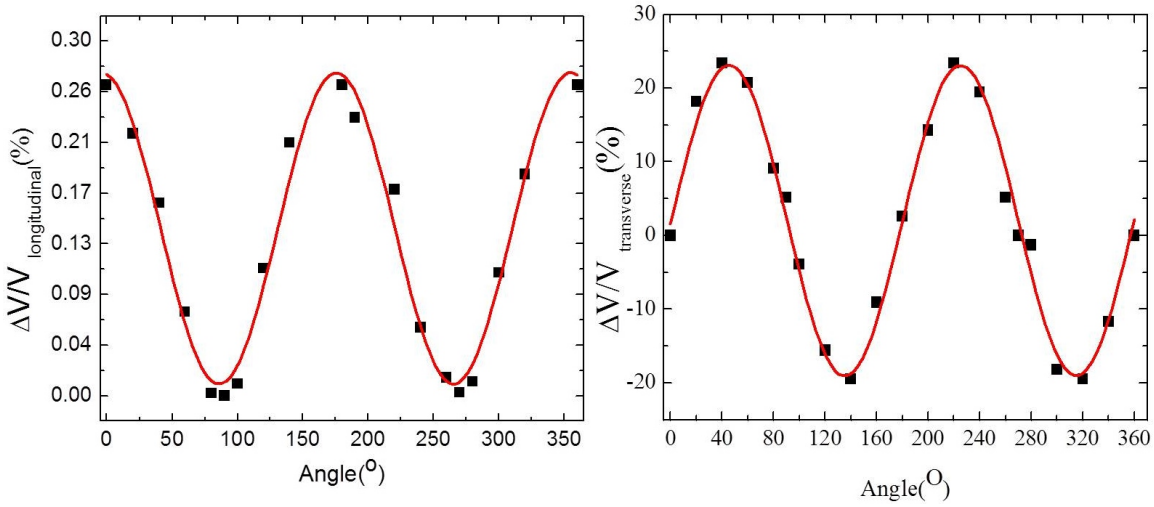

Figure 5.43: Dependence of longitudinal (a) and transverse (b) magnetothermopower on the angle between the ∇T and H (ΔT=30 K)

perature.

Side 1	Side 2	ΔT (K)
20 °C	50 °C	+ 30
	↓	
20 °C	20 °C	0
	↓	
20 °C	0 °C	- 20

Figure 5.44: ∇T was change from +30 K to -20 K in 5°C steps

The experiment was started with +30 K ∇T with side 1 at 20°C and side 2 at 50°C. Then the temperature of side 2 was decreased in 5°C steps. After changing the temperature, the data acquisition was paused until the temperature was stabilized at the new set value (e.g. 3 minutes), at which point a complete field sweep was carried out. As shown in fig. 5.45 the PNE signal changed linearly with the ∇T. This also suggests the absence of out of plane temperature gradient within this temperature range. The out of plane ∇T has a cubic relation with the resultant voltage.

In comparing the magnetoresistance and the magnetothermopower data both longitudinal and transverse components of MR and MTP exhibited the same field and

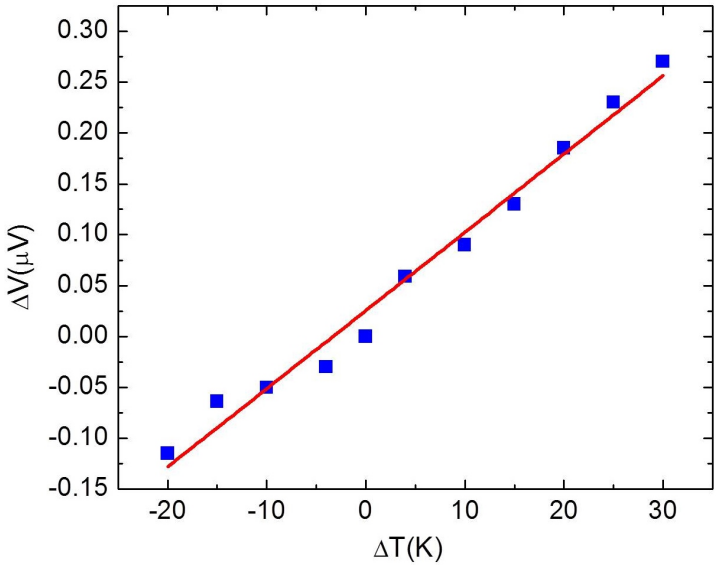

Figure 5.45: ∇T dependence of the PNE, where ∇T was changed from +30 K to -20 K.

angular dependencies. This suggests that both heat current and charge current are impacted by the same effects (spin dependent scattering) inside the ferromagnetic layers leading to two different phenomenon with the same physical origin. While the angular dependence data showed a nearly perfect match in both cases, the field dependence showed a few mismatches. The MTP peaks showed broader peak width relative to the MR peaks. This may be due to the different scattering parameters of charge and heat currents. For further investigation the MOKE and MR measurements were carried out with the ∇T on. One could imagine the high temperature region behaves differently from the low temperature region. Here the same sample was used with the same temperature gradient. For MOKE measurements the field was applied parallel to the ∇T. The MOKE measurements were carried out at different spots on the sample to see the effects of local absolute temperature. Finally one MOKE measurement was carried out at the middle of the sample with no applied temperature gradient.

MOKE measurement data from all the positions showed the same behavior includ-

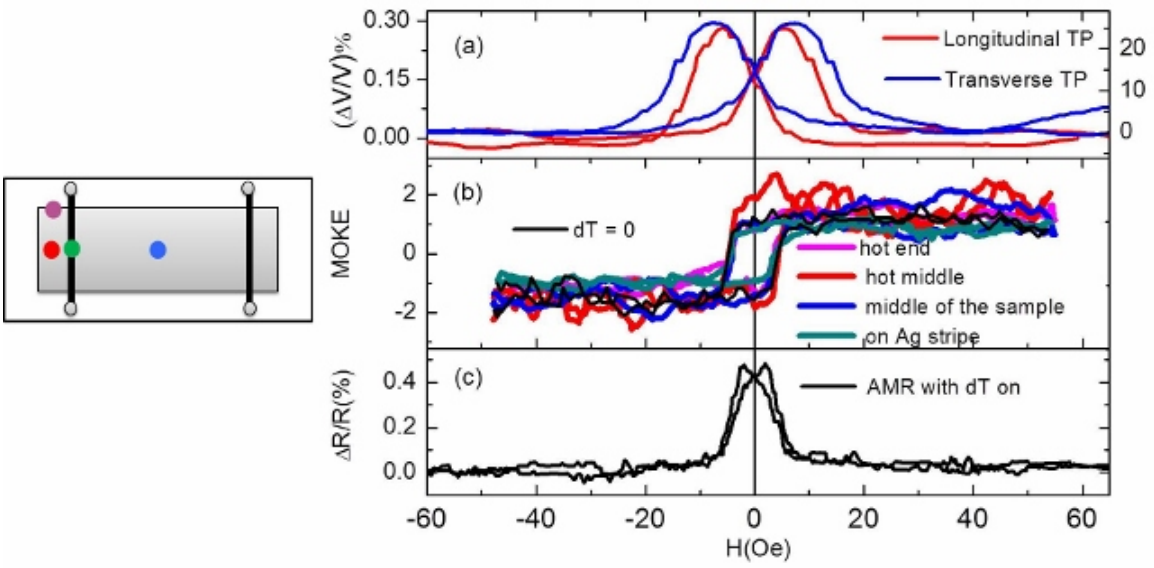

Figure 5.46: Longitudinal and transverse MTP (a) with MOKE (b) and AMR (c) measurements with the ∇T on. Schematic diagram on the left shows the places used in MOKE measurements.

ing the one with no temperature gradient. This suggests that neither the temperature gradient nor the position have any significant effect on the magnetism of the sample. The transverse MTP has a slightly broader peak relative to longitudinal MTP. This is due to the uniaxial anisotropy induced by the 100 Oe growth field. Since the growth field was applied along the length of the sample, the easy axis of the sample was also in that direction [74]. This gives broader peak widths in transverse directions.

An AMR measurement was also carried out with the same ∇T is on. Figure 5.46 (a) and (b) show the comparison of magnetothermopower measurements with the MOKE measurements. Figure 5.46 (c) show the AMR data with the temperature gradient on. It indicates the same coercivity as the MOKE data, and is different in field position peak width from the MTP data. This broadening of the peak in the MTP measurements could be related to thermal smearing. Due to the different temperatures, the Fermi function at hot and cold sides are smeared differently.

Since the temperature difference at hot and cold ends are relatively larger (10 %) the smearing can be significant (fig. 5.47). This can lead to different Fermi functions

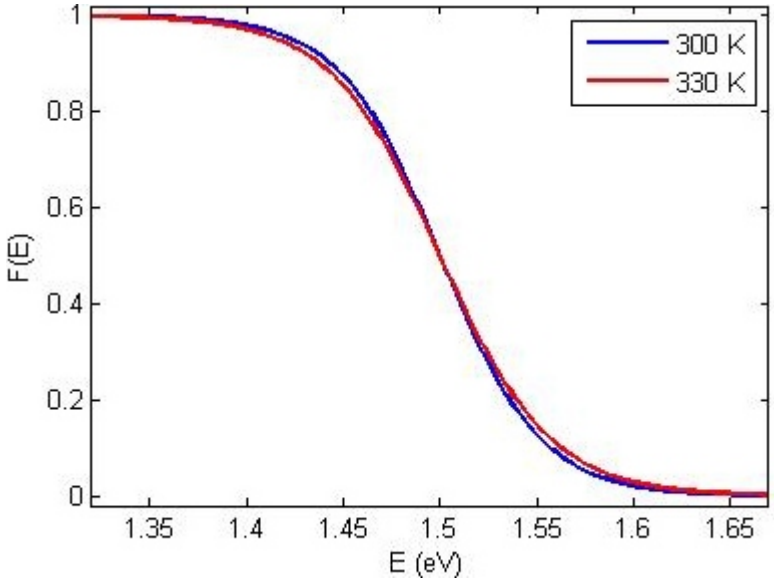

Figure 5.47: Fermi function at 300 K and 300 K

at two ends resulting charge carriers with different Fermi energies and velocities. These charge carriers due to the temperature gradient can have different scattering parameters relative to the normal charge carriers in MR measurements. This could be the main reason to have broaden peaks in MTP measurements relative to MR measurements.

Apart from this broadening, our measurements indicate that the origin of the magnetothermopower and the magnetoresistance is the same physical phenomenon, namely spin dependent scattering of conduction electrons.

5.4.6 Pinning of magnetic domains deposited on the cross electrodes

This effect was observed on a 20nm thick Ni layer deposited on 10nm Au cross electrodes. The Au cross electrodes were deposited on to Si/SiO_x substrates using e-beam deposition and followed by sputter deposition of Ni. The sample was mounted onto the set up and ∇T of 1.8 K/mm was applied along the sample. The resultant voltage was measured using nano-voltmeters as above. The set up was placed inside a electromagnet and the magnetic field was swept in a hysteretic manner. In this case

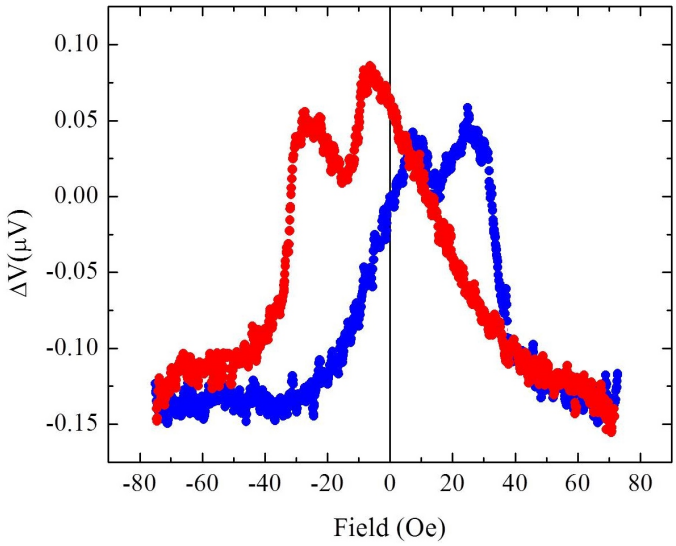

Figure 5.48: Twin peaks on Au/Ni sample with ∇T of 1.8 K/mm

also an AMR shaped signal was observed on both ends, but they consisted of twin peaks instead of a single AMR shaped peaks. This suggests presence of pinned domains on the sample. For further investigation the sample was measured by Magneto Optical Kerr effect (MOKE) magnetometry.

MOKE measurements were taken on two different spots on the sample: One on the Ni layer on Au electrode, and the other on the Ni layer directly on the Si/SiO_x substrate.

MOKE data on the Ni only exhibited a normal hysteresis curve. The coercive field of the hysteresis loop did not match with thermal measurement peaks. But it was placed exactly between two peaks. This suggests a presence of a negative peak within a positive peak. The MOKE data on Ni on Au (black curve on fig. 5.50) showed double hysteresis loops. One hysteresis loop was matched with the previous measurement done on the Ni layer and the other one had a larger coercivity relative to the above. The coercivity of the second hysteresis loop was matched with the second peak on the thermal measurement. This double hysteresis loop indicates the presence of different domains oriented in different direction in the same sample. The

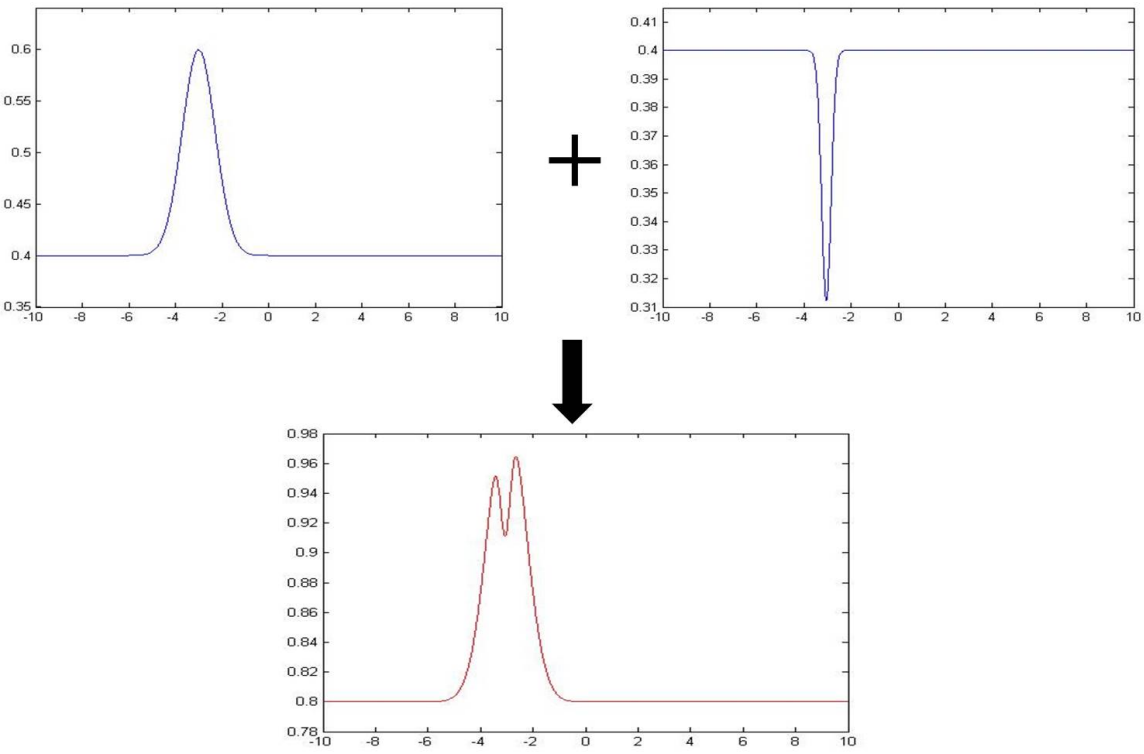

Figure 5.49: Two peaks in opposite directions can form double peaks

only possible way for this to occur is to form some pinned domains around the Au electrodes due to the geometry. This is measured because the larger spot spills off the electrode.

Figure 5.51 shows the possible ways of forming pinned domains in the Ni film around Au stripe. These types of pinned domains can produce multiple hysteresis loops with different coercivities. Therefore in MOKE data the double hysteresis on the Ni on Au confirms the presence of pinned domains around the Au electrode. The single hysteresis loop is from the rest of the sample where the Ni layer was not affected from the Au layer. Finally it's possible to conclude that the twin peaks observed in the Au/Ni sample was due to a positive and a negative peak formed as a result of pinned domains around the Au stripes in the Ni layer. Apart from the twin peaks this sample also gave normal AMR shaped field dependence and showed no signs of SSE. This led us to investigate more about the Nernst effect (magnetothermopower)

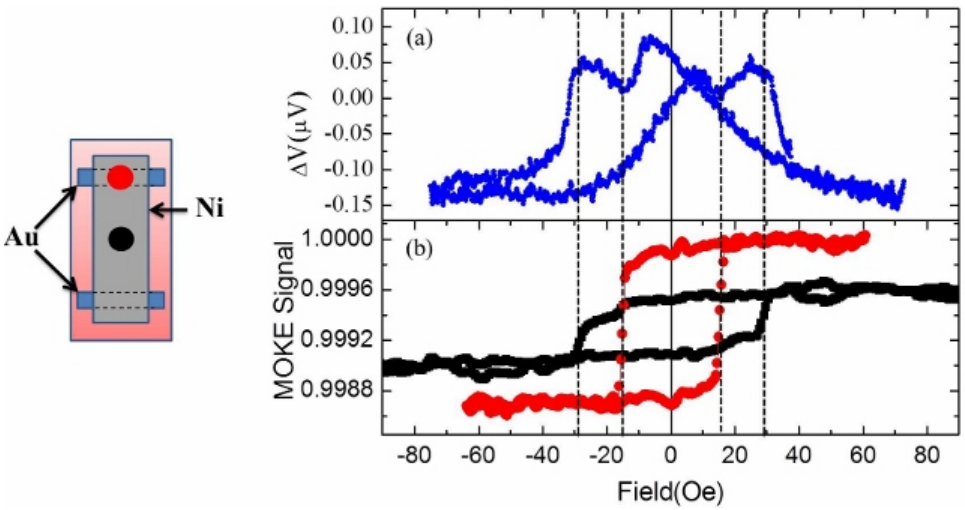

Figure 5.50: PNE (a) and MOKE (b) data of the Au/Ni sample. black - Ni on the Au stripe and red - Ni on the Si/SiO_x substrate

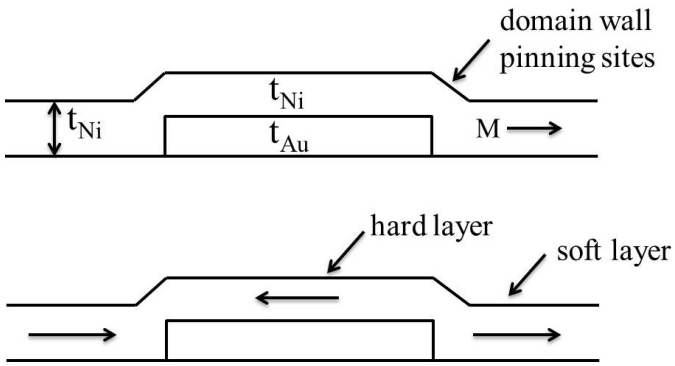

Figure 5.51: Different domains formed on Ni on Au stripe

and related phenomenon.

5.5 Spin dependent Seebeck effect on spin valve structures

In previous chapters we have demonstrated that both heat current and the charge current behave similarly inside materials and lead to similar properties. In ferromagnetic materials the heat current combined with magnetization to generate various effects including planar Nernst effect, Anomalous Nernst effect, Spin Seebeck effect and Spin dependent Seebeck effect. In this section the spin dependent Seebeck effect

was measured on metallic spin valve structures. In traditional current in plane spin valve measurements a constant charge current was applied to the spin valve and the resultant voltage was measured along the length of the spin valve. In this experiment a heat current was supplied to the spin valve through an in plane temperature gradient. Then the resultant voltages were measured by nano-voltmeters.

5.5.1 Py/Cu/Py/FeMn Spin Valves

The spin valve structures were grown on top of Si/SiO_x substrates with a 100 Oe growth field. First a 5 nm thick Ta seed layer was deposited on to the Si/SiO_x substrate and followed by 5 nm of Py, 5 nm of Cu, 10 nm of Py and 15 nm of FeMn layers. Here the purpose of FeMn is to exchange bias the top Py layer to ensure the two ferromagnets switch independently. Previous studies have shown that the FeMn (111) orientation gives the maximum exchange bias value [75]. The first Ta seed layer leads to polycrystalline growth of Py with (111) texture along the growth direction. All the metal Py, Cu, FeMn are FCC with similar enough lattice parameters 3.55 Å, 3.61 Å and 3.23 Å respectively, that the (111) texture progress throughout the structure's thickness. Figure 5.52 shows the schematic cross section of the sample with film thicknesses noted.

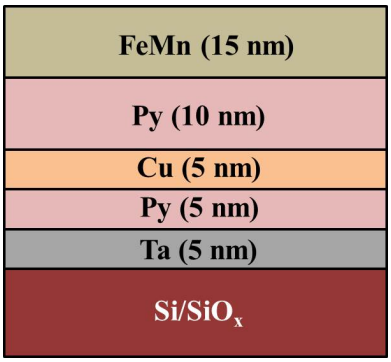

Figure 5.52: Si/SiO_x/Ta/Py/Cu/Py/FeMn Spin valve

Next the sample was mounted in the same setup used for the previous thermal experiments and a 30 K temperature difference was applied across the sample along

the easy axis. The voltage was measured parallel to the temperature gradient. To measure the field dependence of the signal the external magnetic field was swept between ± 400 Oe and the field was applied along ∇T.

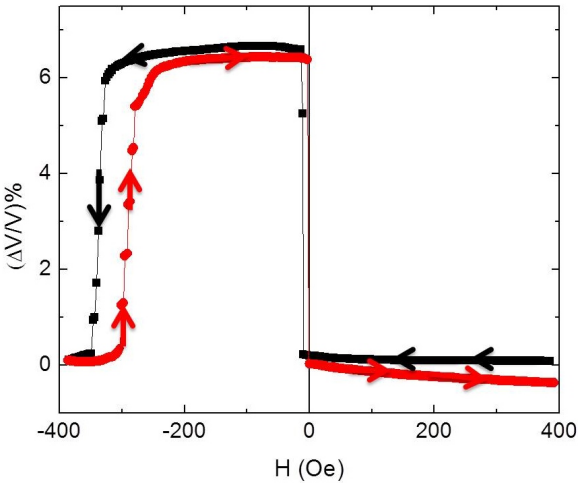

Figure 5.53: Spin dependence Seebeck effect of Si/ SiO_x/ Ta/ Py/ Cu/ Py/ FeMn Spin valve with 30 K temperature difference.

A giant magneto-resistance shaped signal was observed upon sweeping the magnetic field (fig. 5.53). The independent switching of two Py layers leads to two voltage levels with the percentage change(ΔV/V%) close to 7 % ($\Delta V = V_{parallel} - V_{anti-parallel}$). The top Py layer was exchanged biased by 300 Oe giving well defined parallel and anti-parallel states.

The magnitude of the signal was measured as a function of temperature gradient with the temperature difference changed from +30 K to -30 K in 5 K steps. In each step a full field sweep was carried out. The signal magnitude with respect to the background was plotted against the corresponding temperature difference. A linear change in SDSE signal was observed relative to the temperature gradient (fig.5.54). The sign of the signal was also flipped when the direction of the temperature gradient was flipped. Symmetric behaviour was observed in the signal in negative and positive temperature gradients.

Next the SDSE signal was measured as a function of the top Py layer thickness.

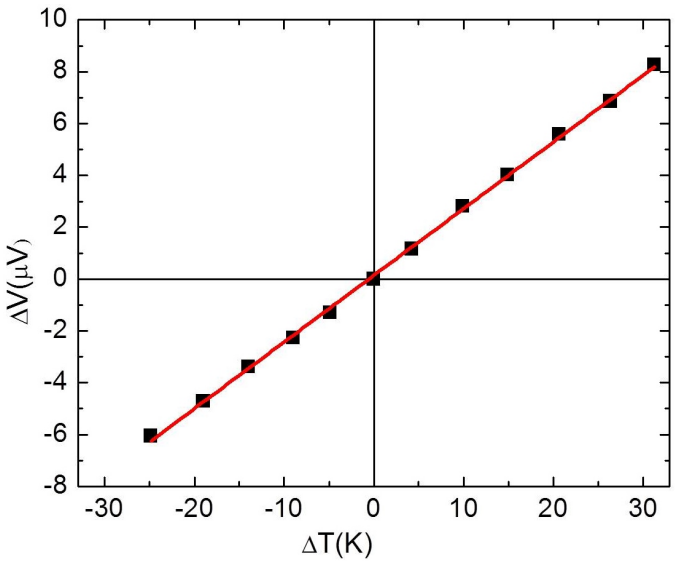

Figure 5.54: Temperature gradient dependence of the SDSE signal of Si/ SiO_x/ Ta/ Py/ Cu/ Py/ FeMn Spin valve

The thickness of the Py layer was changed from 75Å to 350Å. Here all the samples were grown simultaneously using an *in situ* mask exchange system in the sputtering system. Therefore it's possible to conclude that any changed in the signal can be exclusively due to thickness of the Py. The fig.5.55 shows the variation of the signal magnitude with the top Py layer thickness. An increase in the signal was observed form 75 Å to 100 Å. After 100 Å the signal magnitude decreases with the Py film thickness.

All the above data were very much similar to the giant magneto-resistance behavior. To compare both phenomena the GMR and the SDSE were measured in a single spin valve structure.

5.5.2 Comparison of giant magneto-resistance with the spin dependent Seebeck effect in Py/Cu/Py spin valves.

In this section the effect of the heat current and the electrical current on the spin valves was measured. First a 93 μA constant dc current was applied along the length

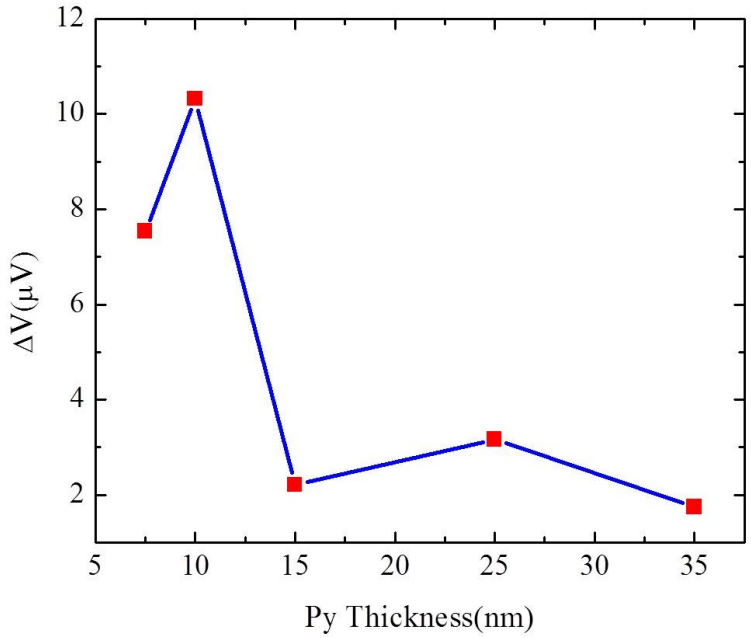

Figure 5.55: Py layer thickness dependence of the SDSE signal of Si/ SiO_x/ Ta/Py/ Cu/ Py/ FeMn Spin valve with 30 K temperature difference.

of the Ta (5 nm)/Py (5 nm)/Cu (5 nm)/Py (10 nm)/FeMn (15) spin valve. For the thermal measurements a 30 K temperature difference was applied along the 10 mm sample crating a 3 K/mm temperature gradient. The field dependence of the voltage was measured by sweeping the external magnetic field between ±900 Oe.

Both MR and SDSE showed similar field dependence at room temperature with $\nabla T = 30K$(fig.5.56). A clear GMR signal with two different resistance states was observed in both measurements. Most notably a higher percentage change in the signal was observed in the SDSE (4.5%) relative to the GMR (1.7%).

These values persist even when the current and ΔT are reduced by an order of magnitude. A 13 μA current and a 3 K temperature gradient was applied in each case. The absolute magnitude of both signals of course decreases significantly, but the percentage changes of the signals remained the same (fig.5.57). This suggests that both the GMR percentage and the SDSE percentage does not depend on the amount of current and the temperature gradient respectively.

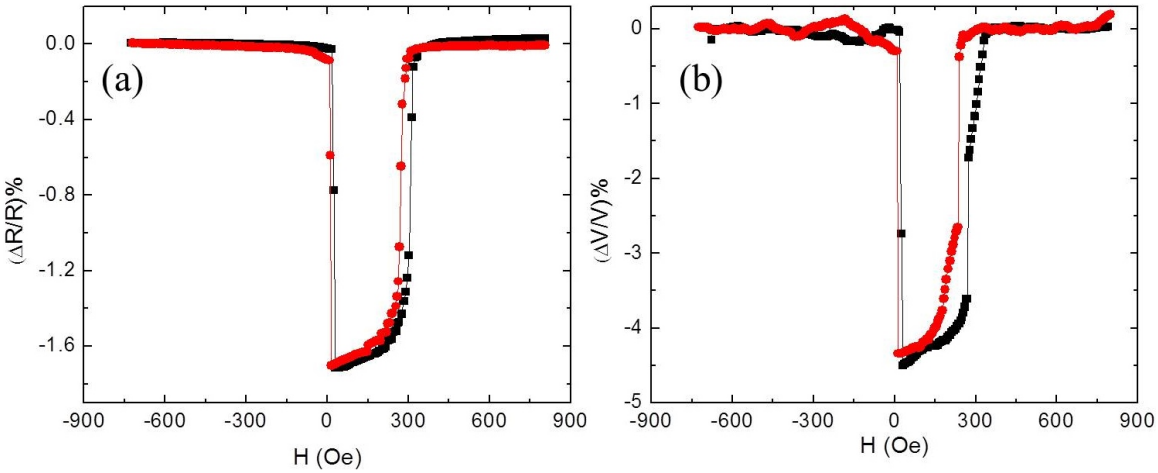

Figure 5.56: MR and SDSE of Py/Cu/Py/FeMn spin valve. (a) MR of the spin valve measured with 93μA current applied along the sample. (b) SDSE of the spin valve with 30 K temperature difference along the length of the sample.

In the spin valve structure we also see some slight different field dependence between charge and heat currents, again localized primarily around the magnetic reversal fields.

These data suggest that the heat current also behaves similar to the charge current inside the spin valve structure. The origin of GMR is interface scattering of conduction electrons traveling through the spin valve. To get a similar signal with the temperature gradient, the heat current also should undergo some type of scattering process inside the spin valve. Higher signal percentage indicates that the scattering process of the thermal current is more efficient than that of charge current.

5.6 Chapter Summary

Anomalous Nernst effect on Py thin film was measured. A proper sample preparation and mounting techniques were introduced to minimize the ANE. Planar Nernst effect and spin dependent Seebeck effect were measured on Py thin films. They were compared to their charge counterpart the anisotropic magneto-resistance. All the effects showed similar behavior suggesting the similar origin, presumably the spin

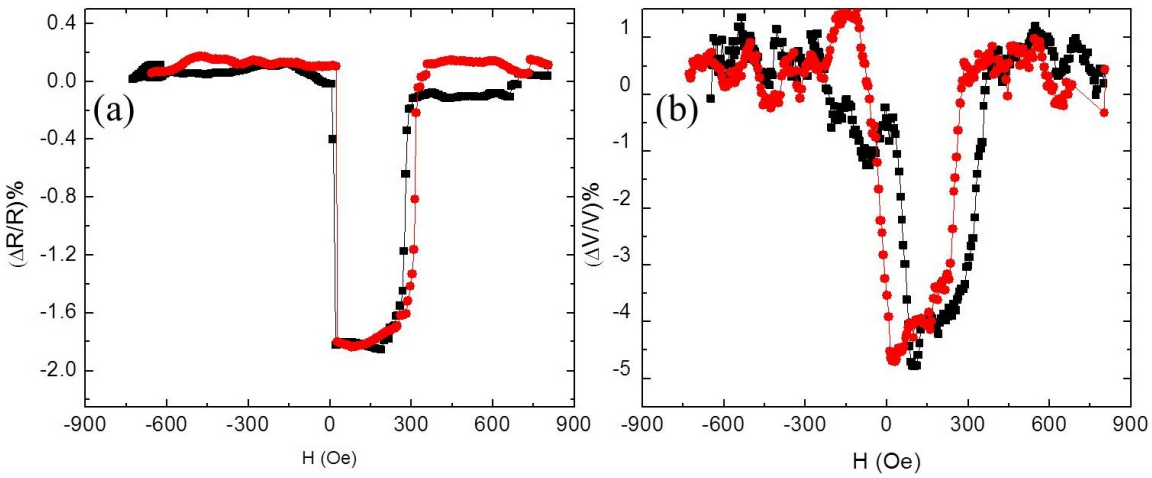

Figure 5.57: MR and SDSE of Py/Cu/Py/FeMn spin valve with reduced current and the ∇T. (a) MR of the spin valve measured with 13μA current applied along the sample. (b) SDSE of the spin valve with 3 K temperature difference along the length of the sample.

dependent scattering of conduction electrons. Magnetothermopower of Py/Cu/Py spin valve was successfully measured and compared with the GMR of the same structure. Both phenomenon showed GMR shaped field dependence with higher signal magnitude in magnetothermopower.

6 Concluding Remarks

High quality Fe_3O_4 thin films were grown on MgO (100) substrates with ultra thin buffer layers. Structural, transport, and magnetic properties of Fe_3O_4 showed strong dependence on the strain due to the lattice mismatch. Magnetization measurements indicated the rotation of easy axis of Fe_3O_4 during the Verwey transition. This was confirmed by the MFM study on Fe_3O_4 thin films and it also showed that the magnetic easy axis of Fe_3O_4 slightly rotate out of plane during the Verwey transition.

Spin valve structures were fabricated using Fe_3O_4 thin films, based on spin polarization through reflection. The GMR values observed were low relative to the all metal spin valves. Possible reasons includes low efficiency of the polarization of the reflection process and low spin polarization of Fe_3O_4. Field growth induced uniaxial anisotropy in Py and Fe_3O_4 thin films. In spin valve structure it induced a clearly defined parallel and anti-parallel states.

Anomalous Nernst effect was measured in Py thin films. Proper sample preparing and mounting techniques were introduced to minimize the ANE in metal thin films. Planar Nernst effect and Spin dependent Seebeck effect were measured on Py thin films. Comparison of those two effects with their charge counterpart, anisotropic magneto resistance, suggested the similar origin for all the effects, namely spin dependent scattering. Spin dependent Seebeck effect and giant magneto-resistance were measured in Py/Cr/Py spin valve structures. Both exhibited GMR type of signal with higher percentage change was observed in SDSE.

References

[1] StuartA. Wolf. Spintronics, electronics for the next millenium? *Journal of Superconductivity*, 13:195–199, 2000.

[2] S Das Sarma, Jaroslav Fabian, Xuedong Hu, and Igor uti. Spintronics: electron spin coherence, entanglement, and transport. *Superlattices and Microstructures*, 27:289 – 295, 2000.

[3] S. A. Wolf, D. D. Awschalom, R. A. Buhrman, J. M. Daughton, S. von Molnr, M. L. Roukes, A. Y. Chtchelkanova, and D. M. Treger. Spintronics: A spin-based electronics vision for the future. *Science*, 294(5546):pp. 1488–1495, 2001.

[4] M. Baibich, J.M. Broto, A. Fert, F. Nguyen Van Dau, F Petroff, P. Etienne, G. creuzet, A. Friederich, and J. Chazelas. Giant magnetoresistance of (001) fe/(001)cr magnetic superlattices. *Phys. Rev. Lett.*, 61:2472–2475, 1988.

[5] G. Binasch, P. Grünberg, F. Saurenbach, and W. Zinn. Enhanced magnetoresistance in layerd magnetic structres with antiferromagnetic interlayer exchange. *Phys. Rev. B.*, 39:4828–4830, 1989.

[6] Magnetic recording: advancing into the future. *Journal of Physics D: Applied Physics*, 35:R157, 2002.

[7] J. Hübner, W. W. Rühle, M. Klude, D. Hommel, R. D. R. Bhat, J. E. Sipe, and H. M. van Driel. Direct observation of optically injected spin-polarized currents in semiconductors. *Phys. Rev. Lett.*, 90:216601, May 2003.

[8] B. Beschoten F. Matsukura H. Ohno Y. Ohno, D. K. Young and D. D. Awschalom. Electrical spin injection in a ferromagnetic semiconductor heterostructure. *Nature*, 402:790–792, 1999.

[9] Jack Bass and William P Pratt Jr. Spin-diffusion lengths in metals and alloys, and spin-flipping at metal/metal interfaces: an experimentalist's critical review. *Journal of Physics: Condensed Matter*, 19:183201, 2007.

[10] Igor Žutić, Jaroslav Fabian, and S. Das Sarma. Spintronics: Fundamentals and applications. *Rev. Mod. Phys.*, 76:323–410, Apr 2004.

[11] P.C van Son, H. van Kempen, and P. Wyder. Boundary resistance of the ferromagnetic-nonferromagnetic metal interface. *Phys. Rev. Lett.*, 58:2271–2273, May 1987.

[12] W.Y. Lee, S. Gardelis, B.C. Choi, Y.B. Xu, C.G. Smith, C.W.H. Barnes, D.A. Ritchie, E.H. linfield, and J.A.C. Bland. Magnetization reversal and magnetoresistance in lateral spin injection device. *Journal of Applied Physics*, 85:6682–6685, 1999.

[13] P.R. Hammar, B.R. Bennett, M.J. Yang, and Mark Johnson. Observation of spin injection at a ferromagnet-semiconductor interface. *Phys. Rev. Lett.*, 85:203–206, 1999.

[14] C. Ciuti, J.P. McGuire, and sham. L.J. Spin polarization of semiconductor carriers by reflection off a ferromagnet. *Phys. Rev. Lett.*, 89:156601, 2002.

[15] C. Ciuti, J.P. McGuire, and sham. L.J. Spin dependent properties of a two dimensional electron gas with ferromagnetic gates. *Appl. Phy. Lett.*, 81(25):4781–4783, 2002.

[16] S.A Crooker, M. Furis, X. Lou, C. Adelman, D.L Smith, C.J. Plamstrom, and P.A. Crowell. Imaging spin transport in lateral ferromagnet/semiconductor structures. *Science*, 309(5744):2191, 2005.

[17] S. S. P. Parkin, N. More, and K.P Roche. Oscillations in exchange coupling and magnetoresistance in metallic superlattice structures: Co/ru, co:cr and fe/cr. *Phys. Rev. Lett.*, 64:2304–2307, 1990.

[18] M.A. Ruderman and C KIttle. Indirect exchange coupling of nuclear magnetic moments by conduction electrons. *Phys. Rev.*, 96:99–102, 1954.

[19] Tadao Kasuya. A theory of metallic ferro and antiferromagnetism on zener's model. *Progress of Theoretical Physics*, 16:45–57, 1956.

[20] Kei Yosida. Magnetic properties of cu-mn alloys. *Phys. Rev.*, 106:893–898, 1957.

[21] S. S. P. Parkin. Origin of enhaveced magnetoresistance of magneitic multilayers: Spin-dependent scattering form magnetic interface states. *Phys. Rev. Lett.*, 71:1641–1644, 1993.

[22] A.Fert, A. Barthelemy, P. Glater adn P. Holody, R. Loloee, R. Morel, F. Petroff, P. Scheoeder, L.B. Stern, and T.Valet. Giant magnetoresistance in magnetic nanosturctures. recent developments. *Materials Sceince and Engineering: B*, 31:1–9, 1995.

[23] Yu. S. Dedkov, U. Rüdiger, and G. Güntherodt. Evidence for the half-metallic ferromagnetic state of fe_3o_4 by spin-resolved photoelectron spectroscopy. *Phys. Rev. B*, 65:064417, Jan 2002.

[24] R Pentcheva U Rdiger M Fonin, Yu S Dedkov and G Gntherodt. Magnetite: a search for the half-metallic state. *JPCM*, 19(31):315217–315229, Mar 2007.

[25] Yves Gossuin, Pierre Gillis, Aline Hocq, Quoc L Vuong, and Alain Roch. Magnetic resonance relaxation properties of superparamagnetic particles. *Wiley Interdisciplinary Reviews: Nanomedicine and Nanobiotechnology*, 1(3):299–310, 2009.

[26] Martin Frik1, Arno Schindlmayr, and Matthias Scheffler1. Ab initio study of the half-metal to metal transition in strained magnetite. *New J. Phys*, 9, 2007.

[27] E.J.W. Verwey and P.W. Haayman. Electronic conductivity and transition point of magnetite. *Physica*, 8(9):979 – 987, 1941.

[28] Ze Zhang and Sashi Satpathy. Electron states, magnetism, and the verwey transition in magnetite. *PRB*, 44(24):13319–13331, Dec 1991.

[29] J Walz. The verwey transition a topical review. *Journal of Physics Condensed Matter*, 14:203, 2002.

[30] S.A Morton, G.D Waddill, S Kim, Ivan K Schuller, S.A Chambers, and J.G Tobin. Spin-resolved photoelectron spectroscopy of fe3o4. *Surface Science*, 513(3):L451 – L457, 2002.

[31] Mario Birkholz, Paul F. Fewster, and Christoph Genzel. *Thin Film Analysis by X-ray Scattering.* Wiley-VCH, 2006.

[32] Yoshikazu Fujii. Influence of surface roughness on near-surface depth analysis from x-ray reflectivity measurements. *Surface and Interface Analysis*, 42(10-11):1642–1645, 2010.

[33] Jin-Hyo Boo, Scott A. Ustin, and Wilson Ho. Low-temperature epitaxial growth of cubic sic thin films on si(111) using supersonic molecular jet of single source precursors. *Thin Solid Films*, 343344(0):650 – 655, 1999.

[34] Tao Yu, Yan-Feng Chen, Zhi-Guo Liu, Xiao-Yuan Chen, Li Sun, Nai-Ben Ming, and Lian-Jie Shi. Epitaxial growth of conductive lanio3 thin films by pulsed laser ablation. *Materials Letters*, 26:73 – 76, 1996.

[35] J. P. Shepherd, J. W. Koenitzer, R. Aragón, J. Spal/ek, and J. M. Honig. Heat capacity and entropy of nonstoichiometric magnetite fe3(1-)o4: The thermodynamic nature of the verwey transition. *Phys. Rev. B*, 43:8461–8471, Apr 1991.

[36] Jr. W. F. Egelhoff, R. D. McMichael, C. L. Dennis, M. D. Stiles, A. J. Shapiro, B. B. Maranville, and C. J. Powell. Suppression of orange-peel coupling in magnetic tunnel junctions by preoxidation. *Applied Physics Letters*, 88(16):162508, 2006.

[37] C. Magen, E. Snoeck, U. Luders, and J. F. Bobo. Effect of metallic buffer layers on the antiphase boundary density of epitaxial fe[sub 3]o[sub 4]. *Journal of Applied Physics*, 104(1):013913, 2008.

[38] P. B. Jayathilaka, C. A. Bauer, D. V. Williams, M. C. Monti, J. T. Markert, and Casey W. Miller. Impact of ultrathin transition metal buffer layers on fe[sub 3]o[sub 4] thin films. *Journal of Applied Physics*, 107(9):09B101, 2010.

[39] A. K. H. Lee, P. B. Jayathilaka, C. A. Bauer, M. C. Monti, J. T. Markert, A. de Lozanne, and Casey W. Miller. Magnetic force microscopy of epitaxial magnetite films through the verwey transition. *Applied Physics Letters*, 97(16):162502, 2010.

[40] P. B. Jayathilaka, M. C. Monti, J. T. Markert, and Casey W. Miller. Heterostructures for realizing magnon-induced spin transfer torque. *Advances in Condensed Matter Physics*, 2012:2012, 2012.

[41] Bruce M. Moskowitz Katerina Moloni and E. Dan Dahlberg. Domain structures in single crystal magnetite below the verwey transition as observed with

a low temperature magnetic force microscope. *Geophysical Research Letters*, 23(20):2851–2854, 1996.

[42] M. Ziese, R. Höhne, P. Esquinzi, and P. Busch. Micromagnetic studies of magnetite films using μ-hall sensor arrays. *Phys. Rev. B.*, 66(8).

[43] D. Tripathy, A. O. Adeyeye, and S. Shannigrahi. Effect of spacer layer thickness on the magnetic and magnetotransport properties of $fe_3o_4Cuni_{80}fe_{20}$ spin valve structures. *Phys. Rev. B*, 75:012403, Jan 2007.

[44] Sebastiaan van Dijken, Xavier Fain, Steven M Watts, Kentaro Nakajima, and J.M.D Coey. Magnetoresistance of fe3o4/au/fe3o4 and fe3o4/au/fe spin-valve structures. *Journal of Magnetism and Magnetic Materials*, 280:322 – 326, 2004.

[45] P. Li, L. T. Zhang, W. B. Mi, E. Y. Jiang, and H. L. Bai. Origin of the butterfly-shaped magnetoresistance in reactive sputtered epitaxial fe[sub 3]o[sub 4] films. *Journal of Applied Physics*, 106(3):033908, 2009.

[46] W. Eerenstein, T.T.M. Palstra, S.S. Saxena, and T. Hibma. Spin-polarized transport across sharp antiferromagnetic boundaries. *Phys. Rev. Lett.*, 88(24).

[47] M. Julliere. Tunneling between ferromagnetic films. *Physics Letters A*, 54(3):225 – 226, 1975.

[48] Mark Johnson and R. H. Silsbee. Thermodynamic analysis of interfacial transport and of the thermomagnetoelectric system. *Phys. Rev. B*, 35:4959–4972, Apr 1987.

[49] Jing Shi, Kevin Pettit, E. Kita, S. S. P. Parkin, R. Nakatani, and M. B. Salamon. Field-dependent thermoelectric power and thermal conductivity in multilayered and granular giant magnetoresistive systems. *Phys. Rev. B*, 54:15273–15283, Dec 1996.

[50] Laurent Gravier, Santiago Serrano-Guisan, Fran çois Reuse, and J.-Ph. Ansermet. Spin-dependent peltier effect of perpendicular currents in multilayered nanowires. *Phys. Rev. B*, 73:052410, Feb 2006.

[51] Gerrit E.W. Bauer, Allan H. MacDonald, and Sadamichi Maekawa. spin caloritronics. *Solid State Communications*, 150(1112):459 – 460, 2010. ¡ce:title¿Spin Caloritronics¡/ce:title¿.

[52] Mikhail Erekhinsky, Felix Casanova, Ivan K. Schuller, and Amos Sharoni. Spin-dependent seebeck effect in non-local spin valve devices. *Applied Physics Letters*, 100(21):212401, 2012.

[53] T. C. Harman, J. H. Cahn, and M. J. Logan. Measurement of thermal conductivity by utilization of the peltier effect. *Journal of Applied Physics*, 30(9):1351–1359, 1959.

[54] Jiang Xiao, Gerrit E. W. Bauer, Ken-chi Uchida, Eiji Saitoh, and Sadamichi Maekawa. Theory of magnon-driven spin seebeck effect. *Phys. Rev. B*, 81:214418, Jun 2010.

[55] J.-E. Wegrowe. Spin transfer from the point of view of the ferromagnetic degrees of freedom. *Solid State Communications*, 150(1112):519 – 523, 2010. ¡ce:title¿Spin Caloritronics¡/ce:title¿.

[56] K. Uchida, S. Takahashi, K. Harii, J. Ieda, W. Koshibae, K. Ando, S. Maekawa, and E. Saitoh. Observation of the spin seebeck effect. *Nature*, 455:778–781, 2008.

[57] Saburo Takahashi and Sadamichi Maekawa. Spin current in metals and superconductors. *Journal of the Physical Society of Japan*, 77(3):031009, 2008.

[58] T. Valet and A. Fert. Theory of the perpendicular magnetoresistance in magnetic multilayers. *Phys. Rev. B*, 48:7099–7113, Sep 1993.

[59] M.C. Cadeville and J Roussel. Thermoelectric power and electronic structure of dilute alloys of nickel and conalt with d transition elements. *journal of Physics F: Metal Physics*, 1:686, 1971.

[60] Moosa Hatami, Gerrit E. W. Bauer, Qinfang Zhang, and Paul J. Kelly. Thermal spin-transfer torque in magnetoelectronic devices. *Phys. Rev. Lett.*, 99:066603, Aug 2007.

[61] E. Saitoh, M. Ueda, H. Miyajima, and G. Tatara. Conversion of spin current into charge current at room temperature: Inverse spin-hall effect. *Applied Physics Letters*, 88(18):182509, 2006.

[62] K. Ando, Y. Kajiwara, S. Takahashi, S. Maekawa, K. Takemoto, M. Takatsu, and E. Saitoh. Angular dependence of inverse spin˘hall effect induced by spin pumping investigated in a $ni_{81}fe_{19}$/Pt thin film. *Phys. Rev. B*, 78:014413, Jul 2008.

[63] O. Mosendz, V. Vlaminck, J. E. Pearson, F. Y. Fradin, G. E. W. Bauer, S. D. Bader, and A. Hoffmann. Detection and quantification of inverse spin hall effect from spin pumping in permalloy/normal metal bilayers. *Phys. Rev. B*, 82:214403, Dec 2010.

[64] J. Jaworski, C. M.and Yang, S. Mack, D. D. Awschalom, J. P. Heremans, and R. C. Myers. Observation of the spin-seebeck effect in a ferromagnetic semiconductor. *Nature Materials*, 9:898, 2010.

[65] C. M. Jaworski, J. Yang, S. Mack, D. D. Awschalom, R. C. Myers, and J. P. Heremans. Spin-seebeck effect: A phonon driven spin distribution. *Phys. Rev. Lett.*, 106:186601, May 2011.

[66] K. Uchida, , H. Adachi, T. An, T. Ota, M. Toda, B. Hillebrands, and E. Maekawa, S. andSaitoh. Long-range spin seebeck effect and acoustic spin pumping. *Nature Materials*, 10:737, 2011.

[67] S. Y. Huang, W. G. Wang, S. F. Lee, J. Kwo, and C. L. Chien. Intrinsic spin-dependent thermal transport. *Phys. Rev. Lett.*, 107:216604, Nov 2011.

[68] Yong Pu, E. Johnston-Halperin, D. D. Awschalom, and Jing Shi. Anisotropic thermopower and planar nernst effect in $ga_{1-x}mn_xAs$ ferromagnetic semiconductors. *Phys. Rev. Lett.*, 97:036601, Jul 2006.

[69] A. D. Avery, M. R. Pufall, and B. L. Zink. Determining the planar nernst effect from magnetic-field-dependent thermopower and resistance in nickel and permalloy thin films. *Phys. Rev. B*, 86:184408, Nov 2012.

[70] Vu Dinh Ky. The planar nernst effect in permalloy films. *physica status solidi (b)*, 17(2):K207–K209, 1966.

[71] A.A. Tulapurkar and Y. Suzuki. Contribution of electronmagnon scattering to the spin-dependent seebeck effect in a ferromagnet. *Solid State Communications*, 150(1112):466 – 470, 2010. ¡ce:title¿Spin Caloritronics¡/ce:title¿.

[72] R. C. O'Handley. *Modern Magnetic Materials: Principles and Applications*. nov 1999.

[73] T. McGuire and R. Potter. Anisotropic magnetoresistance in ferromagnetic 3d alloys. *Magnetics, IEEE Transactions on*, 11(4):1018 – 1038, jul 1975.

[74] P.B. Jayathilaka, C.A. Bauer, D.V. Williams, and C.W. Miller. Influence of growth field on nife, fe o , and nife/cr/fe o spin-valves. *Magnetics, IEEE Transactions on*, 46(6):1777 –1779, june 2010.

[75] H.F. Kirby, T.M. Eggers, P.B. Jayathilaka, S.M. Campbell, and Casey W. Miller. Exchange bias of mu-metal thin films. *Journal of Magnetism and Magnetic Materials*, 324(24):4151 – 4154, 2012.

A Proof of copyright permissions

AMERICAN INSTITUTE OF PHYSICS LICENSE TERMS AND CONDITIONS

Jul 19, 2012

All payments must be made in full to CCC. For payment instructions, please see information listed at the bottom of this form.

License Number	2952620967850
Order Date	Jul 19, 2012
Publisher	American Institute of Physics
Publication	Journal of Applied Physics
Article Title	Impact of ultrathin transition metal buffer layers on Fe3O4 thin films
Author	P. B. Jayathilaka, C. A. Bauer, D. V. Williams, M. C. Monti, et al.
Online Publication Date	Apr 19, 2010
Volume number	107
Issue number	9
Type of Use	Thesis/Dissertation
Requestor type	Author (original article)
Format	Print and electronic
Portion	Figure/Table
Number of figures/tables	4
Title of your thesis / dissertation	Spin dependence transport devices using metals and reactively sputtered magnetic oxides
Expected completion date	Dec 2012
Estimated size (number of pages)	175
Total	0.00 USD

Terms and Conditions

American Institute of Physics -- Terms and Conditions: Permissions Uses

American Institute of Physics ("AIP") hereby grants to you the non-exclusive right and license to use and/or distribute the Material according to the use specified in your order, on a one-time basis, for the specified term, with a maximum distribution equal to the number that you have ordered. Any links or other content accompanying the Material are not the subject of this license.

1. You agree to include the following copyright and permission notice with the reproduction of the Material: "Reprinted with permission from [FULL CITATION]. Copyright [PUBLICATION YEAR], American Institute of Physics." For an article, the copyright and permission notice must be printed on the first page of the article or book chapter. For photographs, covers, or tables, the copyright and permission notice may appear with the Material, in a footnote, or in the reference list.
2. If you have licensed reuse of a figure, photograph, cover, or table, it is your responsibility to ensure that the material is original to AIP and does not contain the copyright of another entity, and that the copyright notice of the figure, photograph, cover, or table does not indicate that it was reprinted by AIP, with permission, from another source. Under no circumstances does AIP, purport or intend to grant permission to reuse material to which it

does not hold copyright.

3. You may not alter or modify the Material in any manner. You may translate the Material into another language only if you have licensed translation rights. You may not use the Material for promotional purposes. AIP reserves all rights not specifically granted herein.
4. The foregoing license shall not take effect unless and until AIP or its agent, Copyright Clearance Center, receives the Payment in accordance with Copyright Clearance Center Billing and Payment Terms and Conditions, which are incorporated herein by reference.
5. AIP or the Copyright Clearance Center may, within two business days of granting this license, revoke the license for any reason whatsoever, with a full refund payable to you. Should you violate the terms of this license at any time, AIP, American Institute of Physics, or Copyright Clearance Center may revoke the license with no refund to you. Notice of such revocation will be made using the contact information provided by you. Failure to receive such notice will not nullify the revocation.
6. AIP makes no representations or warranties with respect to the Material. You agree to indemnify and hold harmless AIP, American Institute of Physics, and their officers, directors, employees or agents from and against any and all claims arising out of your use of the Material other than as specifically authorized herein.
7. The permission granted herein is personal to you and is not transferable or assignable without the prior written permission of AIP. This license may not be amended except in a writing signed by the party to be charged.
8. If purchase orders, acknowledgments or check endorsements are issued on any forms containing terms and conditions which are inconsistent with these provisions, such inconsistent terms and conditions shall be of no force and effect. This document, including the CCC Billing and Payment Terms and Conditions, shall be the entire agreement between the parties relating to the subject matter hereof.

This Agreement shall be governed by and construed in accordance with the laws of the State of New York. Both parties hereby submit to the jurisdiction of the courts of New York County for purposes of resolving any disputes that may arise hereunder.

If you would like to pay for this license now, please remit this license along with your payment made payable to "COPYRIGHT CLEARANCE CENTER" otherwise you will be invoiced within 48 hours of the license date. Payment should be in the form of a check or money order referencing your account number and this invoice number RLNK500821856. Once you receive your invoice for this order, you may pay your invoice by credit card. Please follow instructions provided at that time.

Make Payment To:
Copyright Clearance Center
Dept 001
P.O. Box 843006
Boston, MA 02284-3006

For suggestions or comments regarding this order, contact RightsLink Customer Support: customercare@copyright.com or +1-877-622-5543 (toll free in the US) or +1-978-646-2777.

Gratis licenses (referencing $0 in the Total field) are free. Please retain this printable license for your reference. No payment is required.

AMERICAN INSTITUTE OF PHYSICS LICENSE TERMS AND CONDITIONS

Jul 19, 2012

All payments must be made in full to CCC. For payment instructions, please see information listed at the bottom of this form.

License Number	2952621380564
Order Date	Jul 19, 2012
Publisher	American Institute of Physics
Publication	Applied Physics Letters
Article Title	Magnetic force microscopy of epitaxial magnetite films through the Verwey transition
Author	A. K. H. Lee, P. B. Jayathilaka, C. A. Bauer, M. C. Monti, et al.
Online Publication Date	Oct 18, 2010
Volume number	97
Issue number	16
Type of Use	Thesis/Dissertation
Requestor type	Author (original article)
Format	Print and electronic
Portion	Figure/Table
Number of figures/tables	4
Title of your thesis / dissertation	Spin dependence transport devices using metals and reactively sputtered magnetic oxides
Expected completion date	Dec 2012
Estimated size (number of pages)	175
Total	0.00 USD

Terms and Conditions

American Institute of Physics -- Terms and Conditions: Permissions Uses

American Institute of Physics ("AIP") hereby grants to you the non-exclusive right and license to use and/or distribute the Material according to the use specified in your order, on a one-time basis, for the specified term, with a maximum distribution equal to the number that you have ordered. Any links or other content accompanying the Material are not the subject of this license.

1. You agree to include the following copyright and permission notice with the reproduction of the Material: "Reprinted with permission from [FULL CITATION]. Copyright [PUBLICATION YEAR], American Institute of Physics." For an article, the copyright and permission notice must be printed on the first page of the article or book chapter. For photographs, covers, or tables, the copyright and permission notice may appear with the Material, in a footnote, or in the reference list.
2. If you have licensed reuse of a figure, photograph, cover, or table, it is your responsibility to ensure that the material is original to AIP and does not contain the copyright of another entity, and that the copyright notice of the figure, photograph, cover, or table does not indicate that it was reprinted by AIP, with permission, from another source. Under no circumstances does AIP, purport or intend to grant permission to reuse material to which it

B Publications

1. **P. B. Jayathilaka**, T. M. Eggers, D. D. Belyea, and Casey W. Miller, "Observation of Planar Nernst Effect in Ferromagnetic Thin Films Grown on Macroscopic Substrates (2013), In preparation.

2. Dogan Kaya, Pavel N. Lapa, **Priyanga Jayathilaka**, Hillary Kirby, Casey W. Miller and Igor V. Roshchin,"Controlling exchange bias in FeMn with Cu," J. Appl. Phys. 113, 17D717 (2013)".

3. **P. B. Jayathilaka**, M. C. Monti, J. T. Markert and Casey W. Miller, "Heterostructures for realizing Magnon-Induced Spin Transfer Torque (MISTT),"Advances in Condensed Matter Physics, 2012,168313,(2012).

4. H. F. Kirby, T. M. Eggers, **P. B. Jayathilaka**, S. M. Campbell, and Casey W. Miller, "Exchange bias of mu-metal thin films,"Journal of Magnetism and Magnetic Materials 324, 4151-4154 (2012), .

5. N. Laurita, A. Chaturvedi, C. Bauer, **P. Jayathilaka**, A. Leary, C. Miller, M.-H. Phan, M. E. McHenry, and H. Srikanth,"Enhanced giant magnetoimpedance effect and field sensitivity in Co-coated soft ferromagnetic amorphous ribbons," J. Appl. Phys. 109, 07C706 (2011).

6. A. K. H. Lee, **P. B. Jayathilaka**, C. A. Bauer, M. C. Monti, J. T. Markert, A. de Lozanne, and Casey W. Miller, "Magnetic force microscopy of epitaxial magnetite films through the Verwey transition", Appl. Phys. Lett. 97, 162502 (2010).

7. **P. B. Jayathilaka**, C. A. Bauer, D. V. Williams, and Casey W. Miller, "Influence of growth field on NiFe, Fe_3O_4, and NiFe/Cr/Fe_3O_4 spin-valves", IEEE Trans. Magn. 46, 1777 (2010).

8. **P. B. Jayathilaka**, C. A. Bauer, D. V. Williams, M. C. Monti, J. T. Markert, and Casey W. Miller, "Impact of ultrathin transition metal buffer layers on Fe_3O_4 thin films", J. Appl. Phys. 107, 09B101 (2010).

C Conference Presentations

1. "Effect of ultra thin transition metal buffer layers on Magnetite thin films", **Priyanga Jayathilaka**, Daryl Williams, Chris Bauer, Dustin Belyea and Casey Miller : APS March Meeting 2009, Pittsburgh, PA (March 16-20, 2009).

2. "Impact of transition metal buffer layers on magnetite thin film growth." , C. Bauer, **P.B. Jayathilaka**, D.V.Williams, M. Monti, J.T. Markert and C.W. Miller: MMM/Intermag joint conference, Washington D.C (January 18-21, 2010).

3. "Py/Cr/Fe_3O_4spin valves: MMM/Intermag joint conference", **Priyanga B. Jayathilaka** and Casey W. Miller: MMM/Intermag joint conference, Washington D.C (January 18-21, 2010).

4. "In-plane anisotropy properties in Fe_3O_4thin films on MgO substrates", J. Dou, M.J. Pechan, P. Jayathilaka, D.Williams,C. Bauer and C. Miller: MMM/Intermag joint conference, Washington D.C (January 18-21, 2010).

5. "Influence of growth field on Py, $Fe_3O_4$and Py/Cr/Fe_3O_4spin-valves", **Priyanga Jayathilaka**, Chris Bauer, Daryl Williams and Casey W. Miller: APS March Meeting 2010, Portland, OR (March 15-19, 2010).

6. "Effect of the deposition field on the magnetic properties of epitaxial Fe_3O_4thin films", Jian Dou, Michael Pechan, Priyanga Jayathilaka, Daryl Williams, Chris Bauer and Casey Miller: APS March Meeting 2010, Portland, OR (March 15-19, 2010).

7. "Exchange bias of conetic thin films",**P. Jayathilaka** and C.W. Miller: MMM Conference, Atlanta, GA (November 14-18, 2010).

8. "Enhanced low-field magnetoimpedance effect in softferromagnetic amorphous ribbons coated with magnetic Metals", N. Laurita, A. Chaturvedi, A. Leary, C. Bauer, P. Jayathilaka, C.W. Miller, M.E. McHenry, M.H. Phan and H. Srikanth: MMM Conference, Atlanta, GA (November 14-18, 2010).

9. "Magnetic Force Microscopy of magnetite thin films through the Verwey Transition", A. Lee, P. Jayathilaka, C. Bauer, M. Monti, J.T. Markert, A. de Lozanne and C.W. Miller: MMM Conference, Atlanta, GA (November 14-18, 2010).

10. "Mu metal Exchange bias for GMI applications",**Priyanga Jayathilaka**, Scott Campbell and Casey Miller: APS March Meeting, Dallas, TX (March 21-25, 2011).

11. "Magnetic Force Microscopy of Magnetite Thin Films with Transition Metal Buffer Layers", Alfred KH. Lee, Mark C. Monti, John T. Markert, Alex de Lozanne, Priyanga B. Jayathilaka, Chris A. Bauer, and Casey W. Miller: APS March Meeting, Dallas, TX (March 21-25, 2011).

12. "Magnetic resonance at the Verwey transition in epitaxial Fe_3O_4",M. Pechan, B. Kaster, J. Dou, P. Jayathilaka, C. Bauer, and C. Miller: APS March Meeting, Dallas, TX (March 21-25, 2011).

13. "Magnetocaloric effect in heterostructures of $Ni_xCu_{(1-x)}$ alloys", C.A. Bauer, P.B. Jayathilaka, R.V. Rupani, D.D. Belyea, and Casey W. Miller: APS March Meeting, Dallas, TX (March 21-25, 2011).

14. "Spin Seebeck Effect in Permalloy grown on Gold", **P.B. Jayathilaka**, H.F. Kirby, D.D. Belyea and C.W. Miller: MMM Conference, Scottsdale, AZ (October 31 - November 3, 2011)

15. "Magnetocaloric Effect in Gd/Fe Heterostructures", C. Bauer, D.D. Belyea, P.B. Jayathilaka and C.W. Miller: MMM Conference, Scottsdale, AZ (October 31 - November 3, 2011).

16. "Impact of field-induced exchange anisotropy on the magnetoimpedance effect in FeMn/Metglas ribbons bilayer", N.J. Laurita, A. Chatervedi, P. Jayathilaka, M.H. Phan, H.S. Srikanth and C.W. Miller: MMM Conference, Scottsdale, AZ (October 31 - November 3, 2011).

17. "Search for spin seebeck effect in *in situ* grown thin films" **Priyanga Jayathilaka**, Dustin Belyea, HIllary Kirby and Casey Miller: APS March meeting, Boston, MA (February 27- March 2, 2012).

18. "Effect of Cu Layer on Exchange Bias in FeMn", Dogan Kaya, Priyanga Jayathilaka, Casey Miller and Igor roshchin : APS March meeting, Boston, MA (February 27- March 2, 2012).

19. "Anisotropic Magnetothermopower of Py thin films", **Priyanga Jayathilaka**, D.D. Belyea, T.E.Eggers and Casey Miller : MMM conference, Chicago, IL (January 14- 18, 2013).

20. "Damping in Fe3O4/Ag through the Verwey Transition", D. Stanley, M.J. Pechan, P.B. Jayathilaka and C.W. Miller : MMM conference, Chicago, IL (January 14- 18, 2013).

21. "Controlling Exchange Bias in FeMn with Cu", D. Kaya, P.N. Lapa, P. Jayathilaka, H. Kirby, C.W. Miller and I.V. Roshchin : MMM conference, Chicago, IL (January 14- 18, 2013).

About the Author

Priyanga Buddhika Jayathilaka was born on November 25,1981 in Gampola, Sri Lanka. In 2002 he entered in to University of Peradeniya, Sri Lanka to pursue a bachelors degree in Physical sciences. After first two years in the University he got selected to proceed a special degree in Physics. He worked with Professor A. Kareem in final year project on using conducting polymers to fabricate artificial muscle actuators. He graduated in 2006 with a Bachelor of Science degree in Physics with department honours. After that he moved to United States of America in 2007 and joined with the department of Physics in University of South Florida to pursue a doctoral degree. After spending one semester at USF he joined with professor Casey W. Miller to start his research. As Casey Millers first student he helped to built up the research lab from the scratch. His research was mainly focused on growing magnetic oxides and using them to fabricate spin transport devices.

He was awarded the Fred L. and Helen M. Tharp Endowed Scholarship Fund Graduate Award twice in 2010 and 2012 and Frank E. Duckwall Practicum Internship in Applied Physics in 2012. In 2012 he was headed to NIST centre for Neutron research at Gaithersburg,MD to complete his industrial practicum under the guidance of Dr. Brian Kirby. There he studied the polarized Neutron reflectivity on NiCu graded films.